JGR Solid Earth

RESEARCH ARTICLE
10.1029/2024JB030284

The 2022 M_W 7.3 Southern Sumatra Tsunami Earthquake: Rupture Up-Dip of the 2007 M_W 8.4 Bengkulu Event

Tao Xia[1], Lingling Ye[1], Yefei Bai[2], Thorne Lay[3], Shiqing Xu[1], Hiroo Kanamori[4], Luis Rivera[5], and Sesar Prabu Dwi Sriyanto[6]

[1]Department of Earth and Space Sciences, Southern University of Science and Technology, Shenzhen, China, [2]Ocean College, Zhejiang University, Zhoushan, China, [3]Department of Earth and Planetary Sciences, University of California Santa Cruz, Santa Cruz, CA, USA, [4]Seismological Laboratory, California Institute of Technology, Pasadena, CA, USA, [5]Institut Terre et Environnement Strasbourg, Université de Strasbourg/CNRS, Strasbourg, France, [6]Badan Meteorologi, Klimatologi, dan Geofisika (BMKG), Jakarta, Indonesia

Abstract On 18 November 2022, a large earthquake struck offshore southern Sumatra, generating a tsunami with 25 cm peak amplitude recorded at tide gauge station SBLT. Our *W*-phase solution indicates a shallow dip of 6.2°, compatible with long-period surface wave radiation patterns. Inversion of teleseismic body waves indicates a shallow slip distribution extending from about 10 km deep to near the trench with maximum slip of ~4.1 m and seismic moment of 1.05 × 10^{20} Nm (M_W 7.3). Joint modeling of seismic and tsunami data indicates a shallow rigidity of ~23 GPa. We find a low moment-scaled radiated energy of 4.15 × 10^{-6}, similar to that of the 2010 M_W 7.8 Mentawai event (3.1 × 10^{-6}) and other tsunami earthquakes. These characteristics indicate that the 2022 event should be designated as a smaller moment magnitude tsunami earthquake compared to the other 12 well-documented global occurrences since 1896. The 2022 event ruptured up-dip of the 2007 M_W 8.4 Bengkulu earthquake, demonstrating shallow seismogenic capability of a megathrust that had experienced both a deeper seismic event and adjacent shallow aseismic afterslip. We consider seismogenic behavior of shallow megathrusts and concern for future tsunami earthquakes in subduction zones globally, noting a correlation between tsunami earthquake occurrence and subducting seafloor covered with siliceous pelagic sediments. We suggest that the combination of pelagic clay and siliceous sediments and rough seafloor topography near the trench play important roles in controlling the genesis of tsunami earthquakes along Sumatra and other regions, rather than the subduction tectonic framework of accretionary or erosive margin.

Plain Language Summary Tsunami earthquakes are shallow subduction zone events that occur near the trench, usually on the plate boundary, producing larger than typical tsunamis relative to their surface and body wave earthquake magnitudes. These events produce weak ground shaking, leaving coastal populations unaware of the event until a large tsunami arrives. They are also important indicators of the frictional state of the shallow megathrust fault. We use seismic and tsunami observations to determine the rupture process of the 18 November 2022 Sumatra event, which occurred up-dip of the 2007 magnitude 8.4 Bengkulu rupture. We find that the 2022 moment-magnitude 7.3 event shares common rupture characteristics with other recognized tsunami earthquakes and we designate it as a tsunami earthquake. We compare the tsunami earthquakes that have struck in different subduction zones globally, noting examples involving spontaneous failures of stress accumulations at shallow depths or events triggered by stress and strain perturbation from deeper great earthquakes. Additional endeavors to estimate the seismic coupling of shallow megathrusts are needed to evaluate the potential for tsunami earthquakes.

Key Points:

- The 2022 Sumatra event ruptured up-dip of the 2007 Bengkulu event on a near-trench shallowly dipping fault, producing a moderate tsunami
- Joint modeling of seismic and tsunami data resolves shallow slip of up to 4.1 m in low rigidity material, typical of tsunami earthquakes
- Global observations show that up-dip regions not ruptured in great mega-thrust events can host shallow damaging tsunami earthquakes

Supporting Information:

Supporting Information may be found in the online version of this article.

Correspondence to:

L. Ye,
yell@sustech.edu.cn

Citation:

Xia, T., Ye, L., Bai, Y., Lay, T., Xu, S., Kanamori, H., et al. (2024). The 2022 M_W 7.3 southern Sumatra tsunami Earthquake: Rupture up-dip of the 2007 M_W 8.4 Bengkulu event. *Journal of Geophysical Research: Solid Earth*, *129*, e2024JB030284. https://doi.org/10.1029/2024JB030284

Received 3 SEP 2024
Accepted 30 NOV 2024

Author Contributions:

Conceptualization: Lingling Ye, Thorne Lay, Hiroo Kanamori
Data curation: Tao Xia, Sesar Prabu Dwi Sriyanto
Formal analysis: Tao Xia, Lingling Ye, Yefei Bai, Hiroo Kanamori, Luis Rivera
Funding acquisition: Lingling Ye, Yefei Bai, Thorne Lay, Shiqing Xu
Investigation: Tao Xia, Lingling Ye, Yefei Bai, Thorne Lay, Shiqing Xu, Hiroo Kanamori, Luis Rivera
Methodology: Lingling Ye
Project administration: Lingling Ye
Resources: Lingling Ye
Supervision: Lingling Ye
Validation: Yefei Bai
Visualization: Tao Xia
Writing – original draft: Tao Xia, Lingling Ye
Writing – review & editing: Tao Xia, Lingling Ye, Yefei Bai, Thorne Lay,

1. Introduction

Earthquakes that rupture the near-trench portion of megathrusts are rare but can result in large tsunamis relative to their body and surface wave seismic magnitudes, leading to their designation as tsunami earthquakes based on characteristics of their source spectra (e.g., Kanamori, 1972, 2014; Lay & Bilek, 2007; Okal & Newman, 2001; Polet & Kanamori, 2000; Ye et al., 2016a). Tsunami earthquakes have occurred in the shallow megathrusts of several subduction zones, including the 1896 Sanriku, 1907 Sumatra, 1946 Aleutian Islands, 1960 and 1996 Peru, 1963 and 1975 Kuril, 1992 Nicaragua, 1994 and 2006 Java, 2010 Mentawai (Sumatra), and 2012 El Salvador events. The 2021 M_W 8.2 South Sandwich Island earthquake has a large slow rupture component located between deeper fast components (Jia et al., 2022), so it can be viewed as a tsunami earthquake with broader depth extent

than other tsunami earthquakes. These tsunami earthquakes exhibit distinctive rupture characteristics, including source spectra depleted in short period energy, low stress drop, slow rupture speed, enhanced slip at shallow depth with attendant strong excitation of tsunami waves, and aftershocks with normal faulting mechanisms (e.g., Kanamori, 2014; Lay & Bilek, 2007; Ye et al., 2016a). Various mechanisms have been proposed to explain one or more of these characteristics, such as subduction of a seamount (e.g., Abercrombie et al., 2001), variable frictional properties on the plate interface (e.g., Bilek & Lay, 2002), translation of sloping seafloor (e.g., Tanioka & Satake, 1996), anelastic deformation of the overlying sedimentary wedge (e.g., Du et al., 2021; Ma, 2012), low rigidity and low shear velocity of the shallow megathrust (e.g., Cheung et al., 2022; Polet & Kanamori, 2000; Sallarès & Ranero, 2019; Sallarés et al., 2021), release of gravitational potential energy (McKenzie & Jackson, 2012), free surface interactions (Gabuchian et al., 2017), plate bending (Oryan & Buck, 2020), and so on. However, the robustness of these candidate mechanisms still needs to be validated by further observations, as there are many regions where tsunami earthquakes could potentially strike.

The capacity of the shallow megathrust to store strain and rupture spontaneously depends on its physical characteristics and the stress state along the fault and within the outer accretionary wedge. These factors are intricately linked to the consolidation state and mineral content of accreted and underthrust pelagic sediments and to the deformation structures and width of the outer wedge of the frontal accretionary prism (Qiu & Barbot, 2022). Overlying sediments on top of the wedge can also influence shallow slip as a result of dynamic rupture interactions with energy radiated up from the megathrust (Li et al., 2023). The subducting sediments may govern the up-dip extent of seismic rupture during large megathrust events due to their unstable properties, thereby influencing the potential for devastating tsunami generation (e.g., Ruff & Kanamori, 1980). Specifically, thermally controlled chemical transformations including the smectite to illite transition (e.g., Pytte & Reynolds, 1989; Saffer et al., 2008), the opal to quartz transition (e.g., Spinelli & Underwood, 2004), and carbonate and zeolite cementation (e.g., Moore & Saffer, 2001), may occur within sediments, altering the frictional properties dependent on sediment mineral content, sediment consolidation, and fluid release (e.g., Ikari et al., 2018; Vrolijk, 1990). Some of these processes were inferred to influence shallow coseismic rupture during the 2004 M_W 9.2 Sumatra-Andaman (e.g., Dean et al., 2010; Geersen et al., 2013; Gulick et al., 2011; Hüpers et al., 2017; Stevens et al., 2021) and 2011 M_W 9.1 Tohoku (e.g., Fujie et al., 2020; Kameda et al., 2015; Ujiie et al., 2013) megathrust earthquakes, for which updip rupture that extended to the trench enhanced destructive tsunamis, essentially as coseismic tsunami earthquake component of the total ruptures. In addition, the low shear velocity (or rigidity) near the toe of the wedge likely enhances the shallow slip for tsunami generation (Prada et al., 2021; Sallarès & Ranero, 2019; Sallarès et al., 2021), and the nature of the upper plate sedimentary wedge may control the volume above the underthrust slab in which low rigidity affects rupture properties of the tsunami earthquake. Qiu and Barbot (2022) establish that there is a correlation between maximum tsunami run-up for tsunami earthquakes and width of the outer wedge.

Subduction morphological condition is another key factor that appears to influence the occurrence of tsunami earthquakes. Kanamori and Kikuchi (1993) propose that a non-accreting (erosive) margin facilitates the rupture extending all the way to the trench, with examples being the 1960 M_W 7.6 Peru, 1963 M_W 7.8 and 1975 M_W 7.5 Kuril, and 1992 M_W 7.6 Nicaragua tsunami earthquakes. Minor incoming sediments are totally subducted along the plate-boundary interface in these regions, allowing slip to extend to the trench through a relatively weak and shallow plate-boundary interface covered by sediments. Polet and Kanamori (2000) argue that some sediment-starved trenches with small accretionary prisms and thin sediment can also support rupture nucleation and up-dip propagation in the shallow megathrust due to their rough horst-and-graben structure. Based on marine acoustic data, Geersen (2019) infers that tsunami earthquakes tend to occur in trenches characterized as sediment-starved with rough subducting plates.

Over the past decades, the Sunda megathrust has experienced several significant earthquakes, notably including the 2004 M_W 9.2 Sumatra-Andaman and 2005 M_W 8.6 Nias events, which ruptured the zone from 0°N to 14°N (e.g., Ammon et al., 2005; Hsu et al., 2006; Lay et al., 2005). The 1907 M_W 7.8 Sumatra earthquake located seaward of the 2005 Nias coseismic rupture, is regarded as a tsunami earthquake due to its shallow rupture, low rupture velocity, relatively long duration, and extensive tsunami impact (e.g., Kanamori et al., 2010; Martin et al., 2019). Kanamori et al. (2010) conclude, after reviewing historical seismograms of the 1907 earthquake, that it possibly originated as a thrust event on the subduction interface at a depth of ~30 km and then propagated up-dip to the trench, resulting in an extensive tsunami. Martin et al. (2019) derive the rupture area of the 1907 event located up-dip of the coseismic slip region of the 2005 M_W 8.6 Nias event and find that it had a maximum slip of

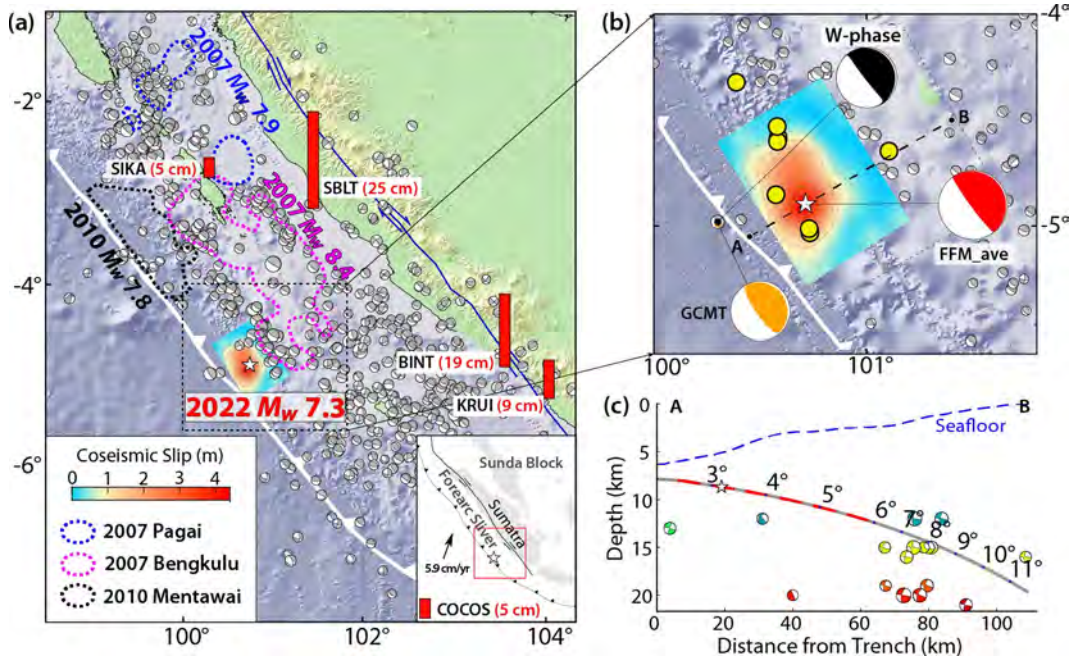

Figure 1. (a) Regional tectonic setting around the 2022 M_W 7.3 Sumatra earthquake near the Sunda trench. The white star indicates the epicenter of the earthquake from the U.S. Geological Survey National Earthquake Information Center (USGS-NEIC) catalog. Magenta, blue, and black outlined patches represent the rupture areas with slip >1 m for the 12 September 2007 M_W 8.4 and M_W 7.9 events (Konca et al., 2008) and the 25 October 2010 Mentawai M_W 7.8 event (Yue, Lay, Rivera, Bai, et al., 2014), respectively. Focal mechanisms show seismicity with magnitude ≥5.0 from the Global Centroid Moment Tensor (GCMT) catalog since 1976. The red bars show five tide gauges with observed tsunami heights. The inset map shows the active tectonic framework in which the Australian plate subducts beneath the Sunda Block of the Eurasian plate along the Sunda trench. Black arrows represent the relative plate motion referenced to the Sunda Block (Demets et al., 2010). The barbed solid line represents the Sunda trench. (b) Coseismic slip distribution of the 2022 Sumatra earthquake, along with the average moment tensor of our preferred slip model (red), our *W*-phase solution (black), and the GCMT solution (orange). Yellow circles show 1-month aftershocks from the USGS-NEIC catalog. (c) Depth profile of the megathrust interface geometry (gray curve) with depth-varying dip from the Slab 2.0 model (Hayes et al., 2018) and varying seafloor bathymetry from BATNAS data (blue dashed curve). The red dashed curve indicates the interface extent used for slip inversion for the 2022 Sumatra earthquake. Focal mechanisms are for M5+ events in the dashed box area in panel (b) from the GCMT catalog, color-coded with the source depth.

~21 m and extended ~220 km southeastward along the shallow Sunda trench, based on the near- and far-field tsunami observations. Qiu and Barbot (2022) estimate a 30 km width to the outer wedge, with a large influx of trench-filled sediment in this accretionary region.

The plate interface in the Sumatra subduction zone from 2°S to 5°S near the Pagai Islands experienced several major ruptures in 2007 and 2010 (Figure 1) and previous great events in 1797 M_W ~ 8.5–8.7 and 1833 M_W ~ 8.6–8.9. The estimated rupture zones of these events indicate strong interplate coupling beneath the Mentawai Islands from geodetic and paleogeodetic observations (e.g., Chlieh et al., 2008; Natawidjaja et al., 2006; Yue, Lay, Rivera, Bai, et al., 2014). The 2007 M_W 8.4 Bengkulu and 2007 M_W 7.9 Pagai events ruptured the central and deep portion of the megathrust, partially overlapping the slip zones of the 1797 and 1833 events, and the Pagai event may be correlated with accumulated slip deficit exceeding the slip that occurred during the 1797 earthquake (Chlieh et al., 2008). On 25 October 2010, the M_W 7.8 Mentawai tsunami earthquake ruptured the shallow portion of the Sunda megathrust, up-dip of the northwestern region of the 2007 M_W 8.4 Bengkulu event, producing a stronger tsunami than the 2007 events (e.g., Borrero et al., 2009; Hill et al., 2012; Lay et al., 2011; Satake et al., 2013; Yue, Lay, Rivera, Bai, et al., 2014). The outer trench wedge width in this region is estimated as 35 km wide, with multiple splay faults in the wedge (e.g., Qiu & Barbot, 2024). The 2010 Mentawai event defied the common assumption that the up-dip region of prior great earthquakes that do not rupture to the trench is aseismic. It demonstrated that local frictional properties in the shallow megathrust could be capable of accumulating sufficient stress or receiving sufficient strain perturbation following great earthquakes downdip to fail

synchronously as for the 2011 M_W 9.1 Tohoku earthquake or fail subsequently in a tsunami earthquake as for the 2010 Mentawai earthquake following the 2007 M_W 8.4 Bengkulu event. Distributed faulting in the outer trench region likely reduces the loading rate for the decollément fault (Qiu & Barbot, 2024), resulting in longer intervals between tsunami events, but strain accumulation is indicated by the larger earthquakes that do occur.

The Sumatra earthquake of 18 November 2022 occurred on the shallow Sunda megathrust off southern Sumatra Island, Indonesia, at 13:37:08 UTC (Figure 1). The U.S. Geological Survey National Earthquake Information Center (USGS-NEIC) hypocenter for the 2022 Sumatra event is 4.90°S, 100.79°E, 25.0 km deep, roughly 204 km southwest of Bengkulu city (https://earthquake.usgs.gov/earthquakes/eventpage/us7000iqpn/executive). The short-period body wave magnitude was 6.1 and the 20-s period surface wave magnitude was 7.2 in the USGS-NEIC catalog. The 2022 Sumatra event ruptured the up-dip megathrust region of the southeastern region of the 2007 M_W 8.4 Bengkulu event and generated a moderate tsunami, which was recorded at four near-field tide gauge stations (Sriyanto et al., 2023) and one far-field tide gauge station (see Data and Resources). It occurred near the trench, providing an opportunity to further explore the seismogenic capability of the shallow megathrust of a subduction zone that previously experienced a great earthquake deeper on the megathrust. Here, we determine the source process of the 2022 Sumatra event using inversion of seismic data and joint modeling of tsunami waveforms, estimate the diagnostic source parameters of tsunami earthquakes, and then discuss diverse slip modes in the shallow megathrust of different subduction zones globally that have experienced major tsunami earthquakes.

2. Methods and Results

2.1. Long-Period Point-Source Solutions for the 2022 Sumatra Earthquake

Routine long-period moment tensor solutions from the USGS-NEIC (*W*-Phase) and Global Centroid Moment Tensor (GCMT) indicate shallow thrust faulting (Table S1 in Supporting Information S1) for the 2022 Sumatra event. Our *W*-phase moment-tensor solution (Kanamori & Rivera, 2008) of 157 three-component 5–10 mHz observations from 95 global broadband network stations indicates a predominantly double-couple point-source solution with $M_0 = 4.39 \times 10^{19}$ Nm (M_W 7.03) at a shallow centroid depth of 9.5 km, $\varphi = 346.6°$, $\delta = 6.2°$, $\lambda = 114.4°$, and centroid time of 15.0 s. The observed long-period surface wave radiation patterns (Figure S1 in Supporting Information S1) have less-pronounced Love wave nodes near 150° and 330°, favoring the dip to be less than 10°, compatible with the *W*-phase solutions. The boostrap analysis of the *W*-phase inversion demonstrates a well-resolved solution with a very shallow dip for the 2022 Sumatra event (Figure S2 in Supporting Information S1).

All of the long-period point-source solutions, summarized in Table S1 in Supporting Information S1, consistently indicate underthrusting focal mechanisms with the strike along the trench, relatively small dip angles ranging from 6.0° to 11.0°, and shallow source depths from 9.5 to 19.5 km. The estimated seismic moment is inversely proportional to the dip angle given that $M_0 \sin 2\delta$ is roughly constant for shallow thrust events (Kanamori & Stewart, 1976). These long-period models all assume the Preliminary Reference Earth Model (PREM) velocity model for the source structure, thus the resolutions of dip angle and shallow source depth are limited. Also, pre-calculated Green's functions are usually fixed to depths of 9.5 km and deeper for the *W*-phase inversions.

2.2. Finite-Fault Inversion With Moment Constraint and Slab Geometry

We invert teleseismic *P* and *S* wave data for space-time slip models utilizing a least squares kinematic multi-time window finite-fault inversion method with variable rakes for specified fault model geometry and rupture speed (e.g., Hartzell & Heaton, 1983; Kikuchi & Kanamori, 1991; Ye et al., 2016b). We apply the inversion procedure with a seismic moment constraint, which minimizes the difference between the inverted total seismic moment and a reference value based on long-period waves (e.g., *W*-phase or GCMT). This stabilizes the inversion process and provides flexibility in the parameterization of the subfault source time functions with a number of overlapping triangles, and use of subfaults with relatively small grid size, as required for smaller events (Ye et al., 2016c). The inversion problem with spatial smoothing and moment constraint with corresponding normalized weights of β_1 and β_2 can be written as,

$$\begin{bmatrix} G \\ \lambda_1 G_1 \\ \lambda_2 G_2 \\ \lambda_3 G_3 \end{bmatrix} [m] = \begin{bmatrix} d \\ 0 \\ \lambda_2 M_0^1 \\ \lambda_3 M_0^2 \end{bmatrix} \quad (1)$$

where $[m]$ and d are model parameters and data, respectively; G is the Green's function matrix; G_1, G_2, and G_3 are the coefficient matrix for spatial smoothing and one-row matrices for moment constraints, respectively. M_0^1, M_0^2 are decomposed components of a given seismic moment M_0 in two directions (Ye et al., 2016c). The weight λ_1, λ_2, and λ_3 are given by

$$\lambda_1^2 = \beta_1 \frac{|G|^2}{|G_1|^2}, \lambda_2^2 = \beta_2 \frac{|G|^2}{|G_2|^2}, \lambda_3^2 = \beta_2 \frac{|G|^2}{|G_3|^2}, \quad (2)$$

where || is the quadratic norm of the matrix. We fix the normalized spatial smoothing weight β_1 as 0.3, and vary the normalized seismic moment constraint weight β_2 from 0.05 to 0.001 in the following iterative inversion section. We use the seismic moment M_0 of 3.84 $\times$ 10^{19} Nm, which is the average of the *W*-phase solutions, as a reference value for the total seismic moment, and set $M_0^1 = M_0 \cos(\lambda + 45°), M_0^2 = M_0 \cos(\lambda - 45°)$ with the rake angle $\lambda = 114.4°$ from our *W*-phase inversion.

We specify a 2.5-D dip-varying fault plane with 8 km by 8 km subfaults, megathrust dip ranging from 2.8° to 5.5° (Figure 1c) and an initial uniform strike of $\varphi = 346.6°$ indicated by the Slab 2.0 model (Hayes et al., 2018), long-period surface wave radiation patterns, and our *W*-phase solution. We adopt Model Crust 1.0 (Laske et al., 2013) as a local source velocity structure to calculate teleseismic Green's functions for a variable bathymetry interpolated from BATNAS (https://tanahair.indonesia.go.id/portal-web/unduh/batnas). Details of the local crustal structure are not known, and shallow velocities are varied in the analysis below. The subfault source time windows are parameterized by 8 overlapping 2.0 s rise-time symmetric triangles for a maximum possible duration of 18 s to account for higher-frequency details in the waveforms, and the peak rupture expansion speed is limited to 2.0 km/s (a range of speeds was considered, but it is not well resolved by the teleseismic ground displacement data). The hypocentral depth is set at 8.0 km constrained by the Slab 2.0 model and our *W*-phase solution, with the epicenter slightly adjusted from the USGS-NEIC location to (4.9°S, 100.7°N) based on a grid search solution using regional arrival times (Figure S3 in Supporting Information S1).

2.3. Iterative Inversion and Modeling With Seismic and Tsunami Data

We employ seismic and tsunami observations to resolve the space-time history of the 2022 rupture. The seismic data set includes 85 vertical component *P* and 30 horizontal component *SH* teleseismic ground displacement recordings with well-distributed azimuthal coverage from global broadband stations, acquired from the Incorporated Research Institutions for Seismology (IRIS). We filtered the displacement recordings in the 0.005–0.9 Hz passband. The tsunami data include four tide gauge recordings from nearby stations along Sumatra (Sriyanto et al., 2023), as well as one far-field tide gauge recording at Cocos Island station from the European Commission Joint Research Centre, ISPRA, Space, Security and Migration Directorate (see Data and Resources).

Tsunami simulation is sensitive to the vertical seafloor deformation amplitude and area, which are proportional to the potency [$\varphi \equiv \int D(x,y)\, dS$] of the slip distribution $D(x,y)$ (Heaton & Heaton, 1989). Accurately recovering reasonable slip amplitude and absolute fault location, which both affect tsunami excitation, is challenging in finite-fault inversions based only on teleseismic waves. Here, we apply an iterative inversion strategy, which has been applied previously to constrain self-consistent slip models using seismic, geodetic, and tsunami observations for large earthquakes (e.g., Yamazaki et al., 2011, 2013, 2018; Ye et al., 2016b, 2022; Yue et al., 2014, 2014a). We seek a preferred space-time slip model by inverting the seismic data and modeling the tsunami data, perturbing the structure and parameters in the inversion to iteratively seek a self-consistent model for both data sets. The iterative approach is used because of the non-linearity of changes in structural and inversion parameters needed to reconcile the data sets. We use NEOWAVE, a well-established forward computation code for the

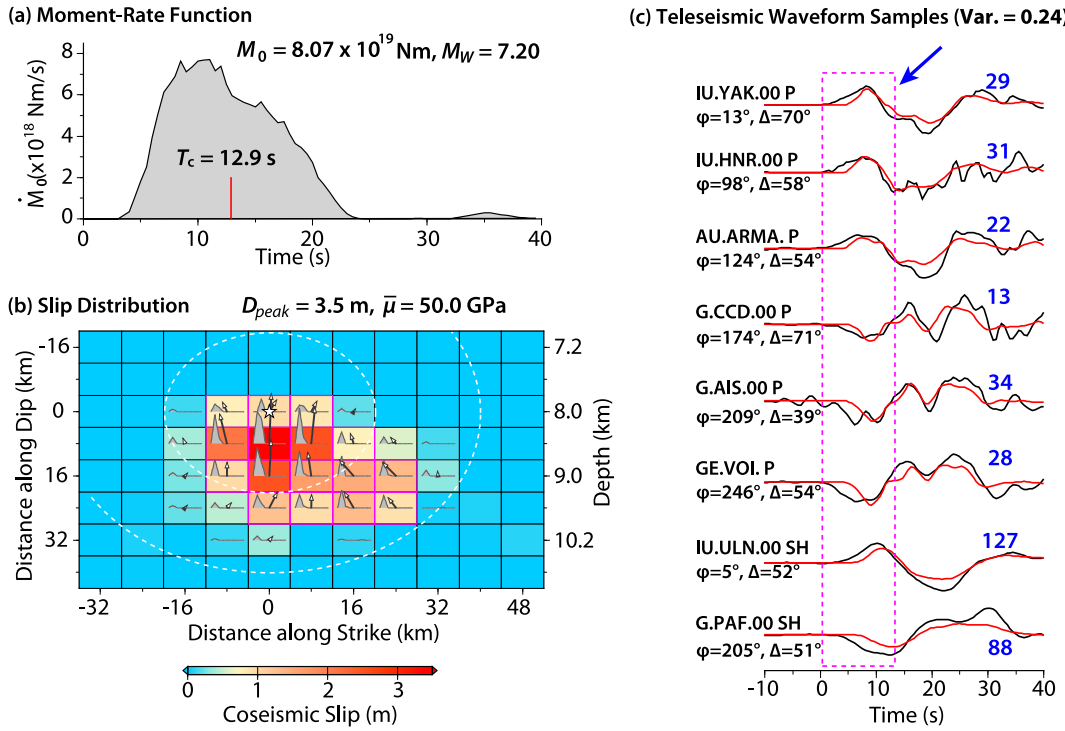

Figure 2. Slip model M01 using the Crust 1.0 source velocity structure with a modest seismic moment constraint ($\beta_2 = 0.05$). (a) The moment rate function with a red tick at the centroid time $T_c = 12.9$ s. (b) Slip distribution with arrows showing the magnitude and direction of slip (hanging-wall relative to footwall) and subfaults color-coded by peak slip. The subfault source time functions are shown within each subfault by gray polygons. White-dashed circles indicate the position of the rupture front in 10 s intervals. (c) Comparisons of the observed (black) and predicted (red) ground displacement waveforms for a subset of seismic waves. The purple dashed rectangular indicates the imprecise wave fits within the initial 15 s.

tsunami simulations (e.g., Bai et al., 2018; Liu et al., 2023; Ye et al., 2021, 2022). In this section, we discuss how we derive our preferred model through a sequence of representative steps.

The initial slip model M01 (Figure 2) is obtained by fixing the normalized moment constraint weight β_2 at a relatively small value of 0.05 because the data fit degrades as β_2 increases. Model M01 has an average rigidity $\bar{\mu}$ of 50.0 GPa, a peak slip D_{peak} of 3.5 m, a potency φ of ~2.1 km^3 over the total fault area. It has an average slip $\overline{D}_{0.15}$ of 1.4 m over a summed area of 1088 km^2 for patches where the slip is greater than 15% of the D_{peak}, that is slip $\geq \sim 0.5$ m, along with the corresponding potency $\varphi_{0.15}$ of 1.5 km^3 for that area (Table S2 in Supporting Information S1). The estimated seismic moment M_0 of M01 is 8.07 $\times$ 10^{19} Nm, substantially larger than that derived from the *W*-phase solutions due to the relatively small β_2. Model M01 fails to fit the seismic waveforms within the initial 15 s (Figure 2), and tsunami simulations for M01 are also unable to fit the first tsunami wave arrivals, showing relatively lower tsunami amplitudes (Figure S4a in Supporting Information S1).

A common, but imprecise practice for scaling slip models to match tsunami amplitudes is to simply enhance the slip in proportion to an assumed rigidity reduction while keeping the seismic moment fixed, but without using a corresponding seismic velocity model to reinvert the seismic data. We gradually increase the overall slip relative to that in model M01 to 180% (in 20% intervals) to determine how much stronger seafloor motion resulting from higher peak and average slip increases is needed to match the tsunami amplitudes. We find that a perturbed Test model with D_{peak} of 5.6 m and $\overline{D}_{0.15}$ of 2.2 m from increasing the overall slip in model M01 by 160% is able to match the tsunami signal amplitudes at SBLT and BINT well (Table S2 in Supporting Information S1), but this model is intrinsically not consistent with the seismic inversion.

To seek a self-consistent model, we invert for slip model M02 (Figure 3) which has enhanced peak slip and average slip close to those for the Test model as a result of reducing the Crust 1.0 crustal seismic velocities by a factor of 0.79. This lowers the average rigidity in the source region (Table S3 in Supporting Information S1) for

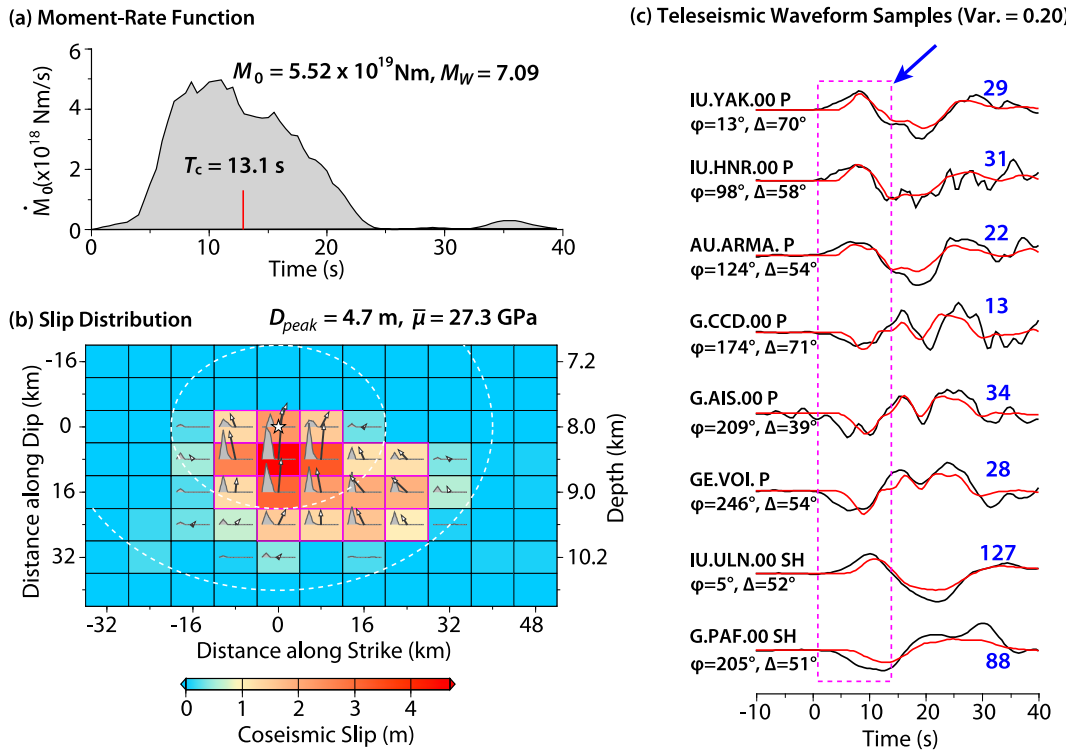

Figure 3. Slip model M02 with lower source velocity and rigidity obtained by multiplying Vp and Vs of Crust 1.0 model by a factor of 0.79 and using a modest seismic moment constraint ($\beta_2 = 0.05$). (a) The moment rate function with a red tick at the centroid time Tc = 13.1 s. (b) Slip distribution with arrows showing the magnitude and direction of slip (hanging-wall relative to footwall) and subfaults color-coded by peak slip. The subfault source time functions are shown within each subfault by gray polygons. White-dashed circles indicate the position of the rupture front in 10 s intervals. (c) Comparisons of the observed (black) and predicted (red) ground displacement waveforms for a subset of seismic waves. The purple dashed rectangular indicates the imprecise wave fits within the initial 15 s.

fixed density and unchanged layer thicknesses. Compared with M01, M02 has a lower $\bar{\mu}$ of 27.3 GPa, higher D_{peak} of 4.7 m and $\overline{D}_{0.15}$ of 1.7 m, slightly higher φ of 2.8 km^3 and $\varphi_{0.15}$ of 2.0 km^3, along with a lower M_0 of 5.52 × 10^{19} Nm (Table S2 in Supporting Information S1). However, as apparent in Figure 3c, model M02 still fails to adequately fit the early portion of the seismic waves. The modest 30% increase of the potency in the model M02, which is less than the 60% increase for the Test model, proves insufficient to address this issue well. This is attributed to the weak excitation of seismic waves in very low-velocity material for a very shallow fault dip, which requires a larger moment to match the far-field seismic waves. We note that the moment constraint employed in M01 and M02 inhibits the increase in seismic moment and potency.

We next relax the total moment constraint by fixing β_2 at a negligible value of 0.001 to invert for slip model M03 (Figure 4), using the same Crust 1.0 velocity model as M01. We adjust the strike from 346.6° to 328.0° to better match the tsunami signals. Model M03 has an $\bar{\mu}$ of 47.8 GPa, a D_{peak} of 4.4 m, φ of 4.8 km^3 for total area, a $\overline{D}_{0.15}$ of 1.8 m, and $\varphi_{0.15}$ of 3.5 km^3, along with M_0 of 1.94 × 10^{20} Nm, 2.5 times larger than for M01 (Table S2 in Supporting Information S1). While the peak slip of M03 is lower than for M01 and M02, it significantly improves the match to the early seismic waveforms (Figure 4c) and the initial tsunami wave arrivals at SBLT and BINT stations (Figure 4d). This notable improvement in fit is attributed to the significantly increased potency, which is ~2.3 times larger than the value for M01, arising from the effects by lowering the moment constraint (Table S2 and Figure S5 in Supporting Information S1). We additionally validate model M03 using simplified point-source forward modeling of the long-period Rayleigh and Love wave spectral amplitudes (Figures 4e and 4f). We follow the spectral method developed by Kanamori and Given (1981) to compare measured long-period surface wave radiation patterns at a period of T = 204.8 s with calculations using the PREM velocity model for the GCMT solution, our W-phase solution, model M03, and the following M04 model. We find that model M03 fails to match the long-period surface wave spectra, yielding significantly higher spectral amplitude compared to both GCMT

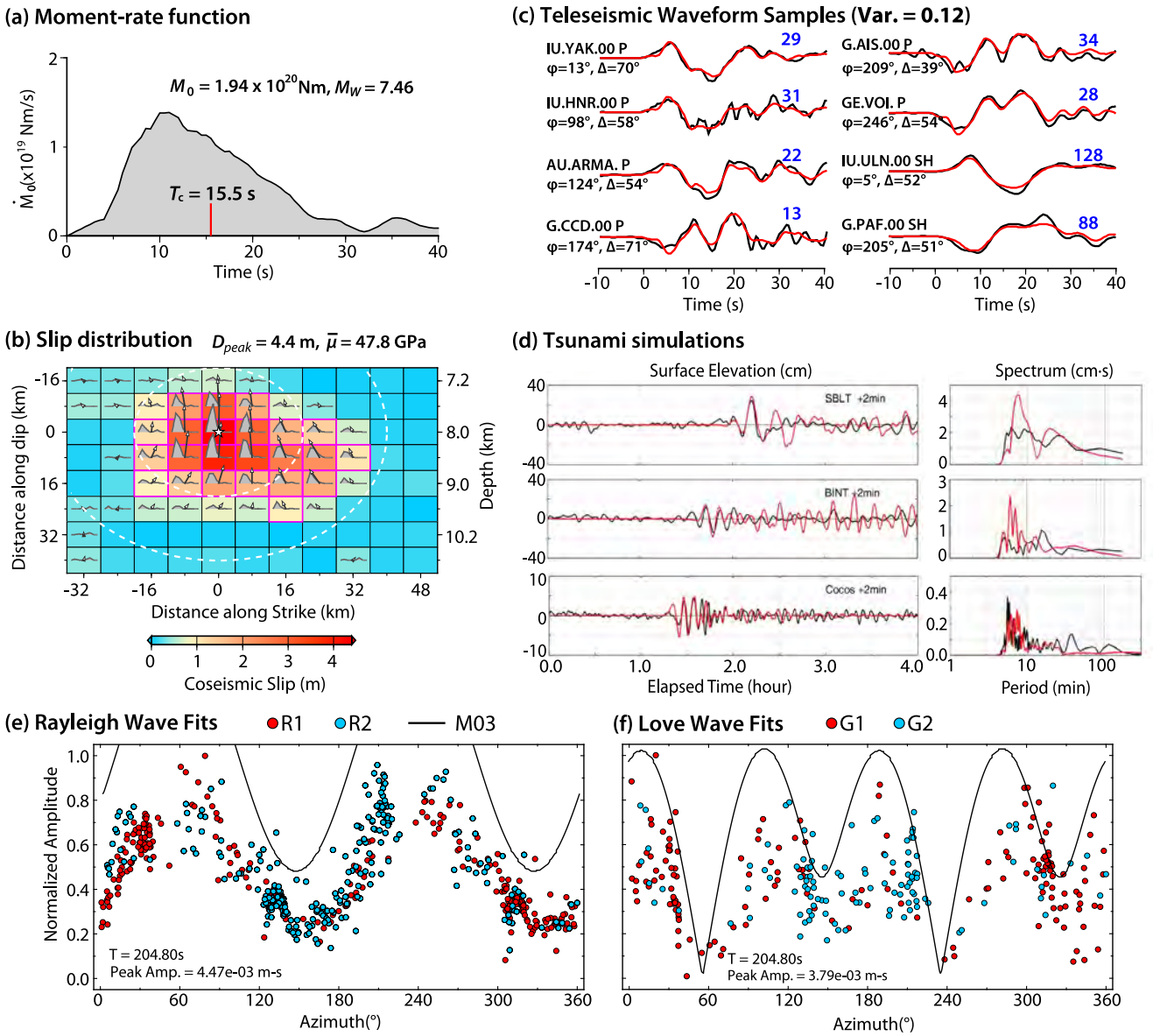

Figure 4. Slip model M03 using the Crust 1.0 source velocity model and a strongly reduced seismic moment constraint ($\beta_2 = 0.001$). (a) The moment rate function with a red tick at the centroid time $T_c = 15.5$ s. (b) Slip distribution with arrows showing the magnitude and direction of slip (hanging-wall relative to footwall) and subfaults color-coded by peak slip. The subfault source time functions are shown within each subfault by gray polygons. White-dashed circles indicate the position of the rupture front in 10 s intervals. (c) Comparisons of the observed (black) and predicted (red) ground displacement waveforms for a subset of seismic waves. (d) Comparison of recorded (black) and computed (red) sea level time series (left) and amplitude spectra (right) at SBLT, BINT, and Cocos tide gauges. The computed time series have been shifted by +2 min for each station, correcting for errors in average path bathymetry and approximations in the modeling. (e)–(f) Observed (dots) and predicted (black curves) Rayleigh wave and Love wave source spectral amplitudes from the model M03.

and our *W*-phase solutions (Figures 4e and 4f, and Figure S1 in Supporting Information S1). This discrepancy is attributed to the considerably larger seismic moment in a high-rigidity source velocity structure for Model M03.

Consequently, we reduce the average source region rigidity to 23.0 GPa by decreasing *Vp* and *Vs* in the source region by a factor of 0.7 (models for a suite of factors were considered) relative to model M01 and obtain slip model M04 (Figure 5). Model M04 has a seismic moment of 1.05×10^{20} Nm ($M_W = 7.3$), peak slip D_{peak} of 4.1 m, total potency φ of 5.5 km^3 and truncated potency $\varphi_{0.15}$ of 4.0 km^3 (Table S2 in Supporting Information S1). Because of the enhanced potency and the decreased seismic moment relative to M03, model M04 model now fits both the initial 15 s of the seismic waves (Figure 5c) and tsunami observations (Figure 5d) well, while satisfactorily matching the

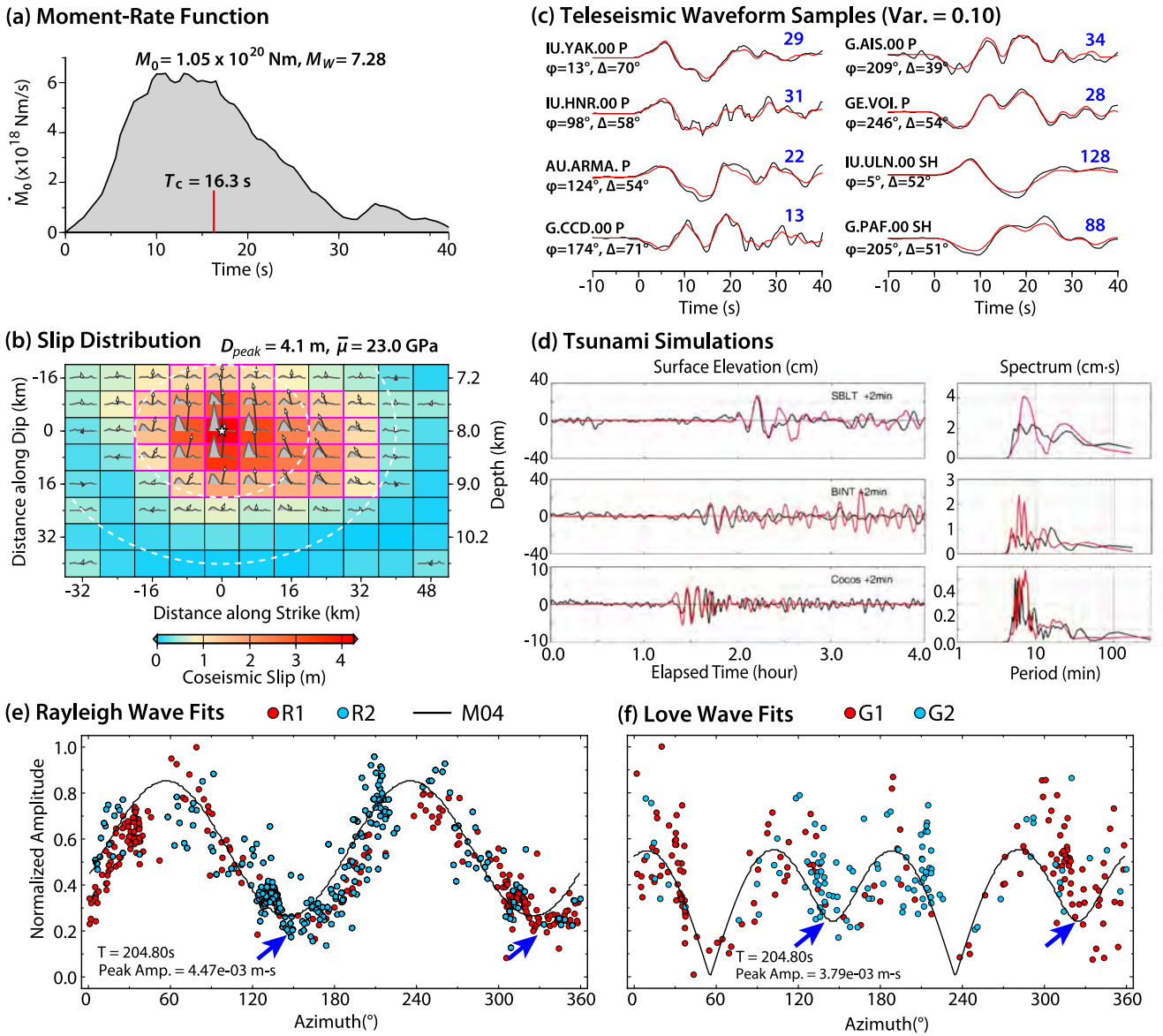

Figure 5. Preferred slip model M04 with Crust 1.0 source velocities being multiplied by a factor of 0.7 and strong reduction of the seismic moment constraint ($\beta_2 = 0.001$). The average rigidity above 10 km depth is 23 GPa. (a) The moment rate function with a red tick at the centroid time $T_c = 16.3$ s. (b) Slip distribution with arrows showing the magnitude and direction of slip (hanging-wall relative to footwall) and subfaults color-coded by peak slip. The subfault source time functions are shown within each subfault by gray polygons. White-dashed circles indicate the position of the rupture front in 10 s intervals. (c) Comparisons of the observed (black) and predicted (red) ground displacement waveforms of a subset of seismic waves. (d) Comparison of recorded (black) and computed (red) sea level time series (left) and amplitude spectra (right) at SBLT, BINT, and Cocos tide gauges. The computed time series have been shifted by 2 min for each station, approximately correcting for errors in average path bathymetry and approximations in the modeling. (e)–(f) Observed (dots) and predicted (black curves) Rayleigh wave and Love wave source spectral amplitudes from the model M04. The blue arrows indicate the symmetry in the Rayleigh wave radiation nodes (e) and the asymmetry in the Love wave radiation nodes (f).

long-period surface wave spectra with a point-source approximation (Figures 5e and 6f). We therefore prefer model M04 as a self-consistent representation of the source for the 2022 Sumatra earthquake.

2.4. Characteristics of the Preferred Slip Model

Our preferred slip model M04 for the 2022 Sumatra earthquake (Figure 5) has an average rake of 94.4 ° and a rough upper bound on the rupture speed of 2.0 km/s. The moment rate function (Figure 5a) has a centroid time of 16.3 s. The seismic moment of 1.05×10^{20} Nm (M_W 7.28) exceeds those estimated by the GCMT

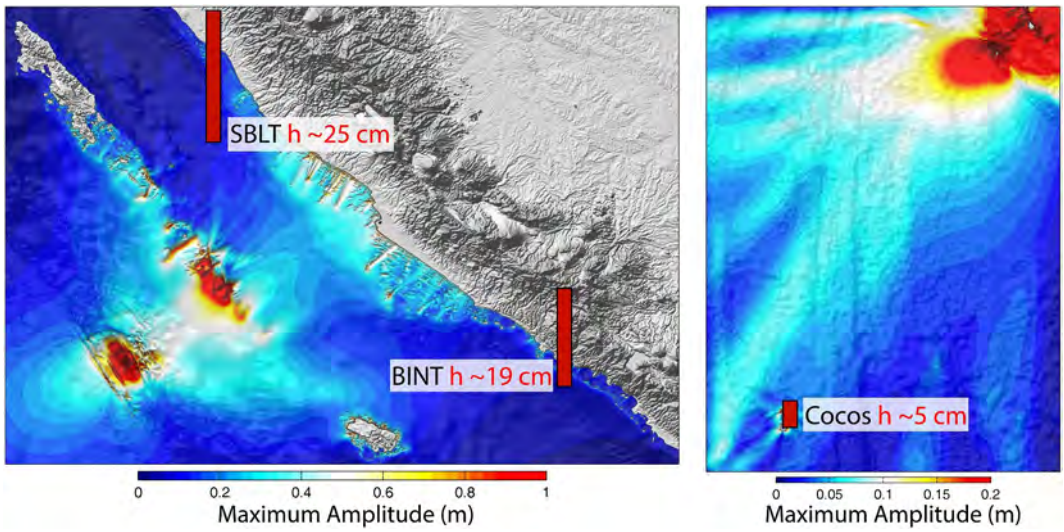

Figure 6. Tsunami simulation results. Maximum sea surface elevation maps near the source region predicted by our preferred finite-fault model M04. The dark red bars of different sizes represent the tsunami heights observed at SBLT, BINT, and Cocos tide gauge stations.

(2.81×10^{19} Nm, M_W 6.90), the USGS-NEIC *W*-phase (3.29×10^{19} Nm, M_W 6.94), and our *W*-phase (4.39×10^{19} Nm, M_W 7.03). This difference is caused by a combination of the very small dip (<4°) in the region where most slip is concentrated (Figure 5b) (even lower dip than the point-source model values), the shallow depth into rock (Figure 1c), and the low velocities and rigidity in the crustal model (the source model is listed in Table S1 in Supporting Information S1). The slip model has a centroid depth of 8.3 km below sea level, with an average water depth of about 4 km over the region of large slip. The average rigidity at the depths with large slip is 23 GPa, which reconciles the seismic and tsunami wave excitation. The large slip has a shallow bilateral concentration extending ~54 km along the strike, extending seaward to near the trench along the dip, with a maximum slip of ~4.1 m. All well-resolved slip is at depths shallower than 10 km.

The preferred slip model M04 fits the complete set of *P*-wave and *SH*-wave data well, accounting for approximately 91% of the power in the observations (Figure S6 in Supporting Information S1). The waveforms are relatively smooth and simple, but have long *P*-coda waves associated with deep water *pwP* reverberations. Our preferred slip model fits some of the *P*-coda and depth phases well due to the use of a 2.5D dip-varying fault model with a gradient in overlying water depth. A fully 3D modeling effort could possibly fit the later coda, but the signals confirm the concentration of slip below deep water. We find similar waveform fits and slip distributions for models with maximum rupture speeds of 1.0–4.0 km/s, indicating limited resolution of rupture expansion speed. This is typical of bilateral ruptures with moderate finiteness. The basic depth range of slip and absolute fault placement is partially constrained by the joint modeling of the tsunami signals. However, high-frequency *P*-wave motions are not all well predicted, probably due to limitations of the simplified source and receiver velocity models and Green's functions that we use for our ground displacement seismograms.

Maximum sea surface elevation maps near the source region and Cocos Island predicted for model M04 are shown in Figure 6, and comparisons between tsunami predictions and observations at SBLT, BINT, and Cocos Island tide gauge stations are shown in Figure 5d. Station SBLT is located closest to the source and recorded a peak tsunami wave first arrival amplitude of 25 cm, while station BINT located on the southeastern coast of Sumatra Island recorded a maximum amplitude of 19 cm. The Cocos Island station, located far from the source, reported a maximum amplitude of 5 cm. The arrival time of the first modeled peak at these three stations is delayed by 2 minutes to align with the observations reasonably, with this shift approximately correcting for errors in the overall bathymetric structure. The fits to these signals confirm the reliability of the seafloor deformation pattern (Figure S5 in Supporting Information S1) produced by our preferred slip model. We are unable to predict the tsunami signal at station SIKA because of the inaccurate available bathymetry information (Figure S7 in Supporting Information S1), and we cannot model the tsunami signal at KRUI well either, due to its low signal-noise ratio (Figure S8 in Supporting Information S1). Overall, the tsunami signals at SBLT, BINT, and Cocos

Island indicate compatibility with the relatively large seismic moment and shallow slip of our preferred model. We also validate our preferred slip model M04 using forward modeling of long-period surface wave spectral amplitude for Rayleigh and Love waves, as discussed in the last section. These comparisons (Figures 5e and 5f) indicate that our preferred model accounts for the asymmetry in the long-period Love wave nodes near 60°/240°, and 150°/330° sufficiently, somewhat better than the point-source moment tensor solutions. The spectral fits for the enhanced moment and reduced dip of the preferred model geometry confirm the viability of our estimated $M_W = 7.3$.

2.5. Tsunami Earthquake Designation

We estimate a radiated energy of $E_R = 4.36 \times 10^{14}$ J for the 2022 event by combining contribution from the moment rate function of our preferred slip model M04 for periods longer than 20 s and from stacked broadband P wave spectra for shorter periods corrected for radiation pattern and propagation effects (e.g., Ye et al., 2016a). The estimated source spectra with the seismic moment from our preferred slip model and W-phase seismic moment (Figure 7a) both indicate a depletion of high-frequency seismic wave radiation for frequencies greater than 0.1 Hz, which is a consistent characteristic of tsunami earthquakes. Figure 7b shows a comparison of the moment-scaled radiated energy for major interplate earthquakes deeper on the megathrust (Ye et al., 2016c) and shallow interplate tsunami earthquakes. The estimated moment-scaled radiated energy $E_R/M_0 = 4.15 \times 10^{-6}$ for the 2022 Sumatra earthquake is close to the values for recognized large well-recorded tsunami earthquakes which range from $\sim 1 \times 10^{-6}$ to 4×10^{-6} (Ye et al., 2016c). Additionally, we note that the low average rigidity of 23 GPa found for our preferred slip model is consistent with the source having a low rupture speed and depleted high-frequency seismic radiation. The static slip-weighted stress drop $\Delta\sigma_E = 1.41$ MPa, and the factor of 0.15 trimmed-slip circular stress drop $\Delta\sigma_{0.15} = 2.30$ MPa (following Ye et al., 2016c), are both smaller than the average for deeper megathrust events (~3.4–4.6 MPa, Ye et al., 2016c). Thus, we find that the 2022 Sumatra event, albeit a moderate-size rupture, involved large shallow slip in low-rigidity material, and its rupture shares several common features with tsunami earthquakes. This includes relatively strong excitation of tsunami waves by large shallow slip, depletion in high-frequency seismic wave radiation, low moment-scaled radiated energy, low rigidity, and low stress drop (e.g., Lay & Bilek, 2007; Ye et al., 2016c). While not a devastating tsunami event, the 2022 event is similar in size to the 2012 El Salvador earthquake which produced a moderate tsunami (Ye et al., 2013), and thus both events can be identified as tsunami earthquakes.

2.6. Coulomb Failure Stress Change From the Previous Earthquakes

The Mentawai segment of the Sunda trench has experienced several great megathrust earthquakes in its history (Figure 8a) and is prone to be relatively strongly locked as inferred from local GPS data (Chlieh et al., 2008). During the period from the 12 September 2007 M_W 8.4 Bengkulu earthquake to the 18 November 2022 Sumatra M_W 7.3 earthquake, most aftershocks of the 2007 M_W 8.4 Bengkulu and the 2007 M_W 7.9 earthquakes were distributed within and around the boundary of the large-slip areas for the 2007 mainshocks and did not extend to the shallow megathrust, consistent with the absence of shallow rupture. There was very sparse seismicity (M4.5+) within the coseismic slip area of the 2022 M_W 7.3 Sumatra event and the northern Mentawai segment near Siberut island (Figure 8). There has not been a great earthquake in the northern Mentawai segment since 1797, so Haridhi et al. (2018) designate it as the North Mentawai Seismic Gap. We explore the stress perturbation in the area of the 2022 M_W 7.3 Sumatra earthquake and the North Mentawai Seismic Gap from the 2007 M_W 8.4 Bengkulu, 2007 M_W 7.9 Pagai, and 2010 M_W 7.8 Mentawai earthquakes by evaluating the change of Coulomb failure stress (ΔCFS).

The ΔCFS involves projecting stress perturbation on a receiver fault resulting from earlier coseismic slip on a nearby fault, which can be written as,

$$\Delta\mathrm{CFS} = \Delta\tau + \mu'\Delta\sigma_n$$

where $\Delta\tau$ is the shear stress change (positive in the slip direction), $\Delta\sigma_n$ is the normal stress change (positive for unclamped fault), μ' is the effective frictional coefficient and set to be 0.4 in this study. We calculate ΔCFS from the 2007 M_W 8.4 Bengkulu earthquake (Konca et al., 2008) on a receiver fault along the slab interface using the Slab 2.0 model. Our results show an increase of the Coulomb stress in the 2022 M_W 7.3 rupture zone of ~0.5–

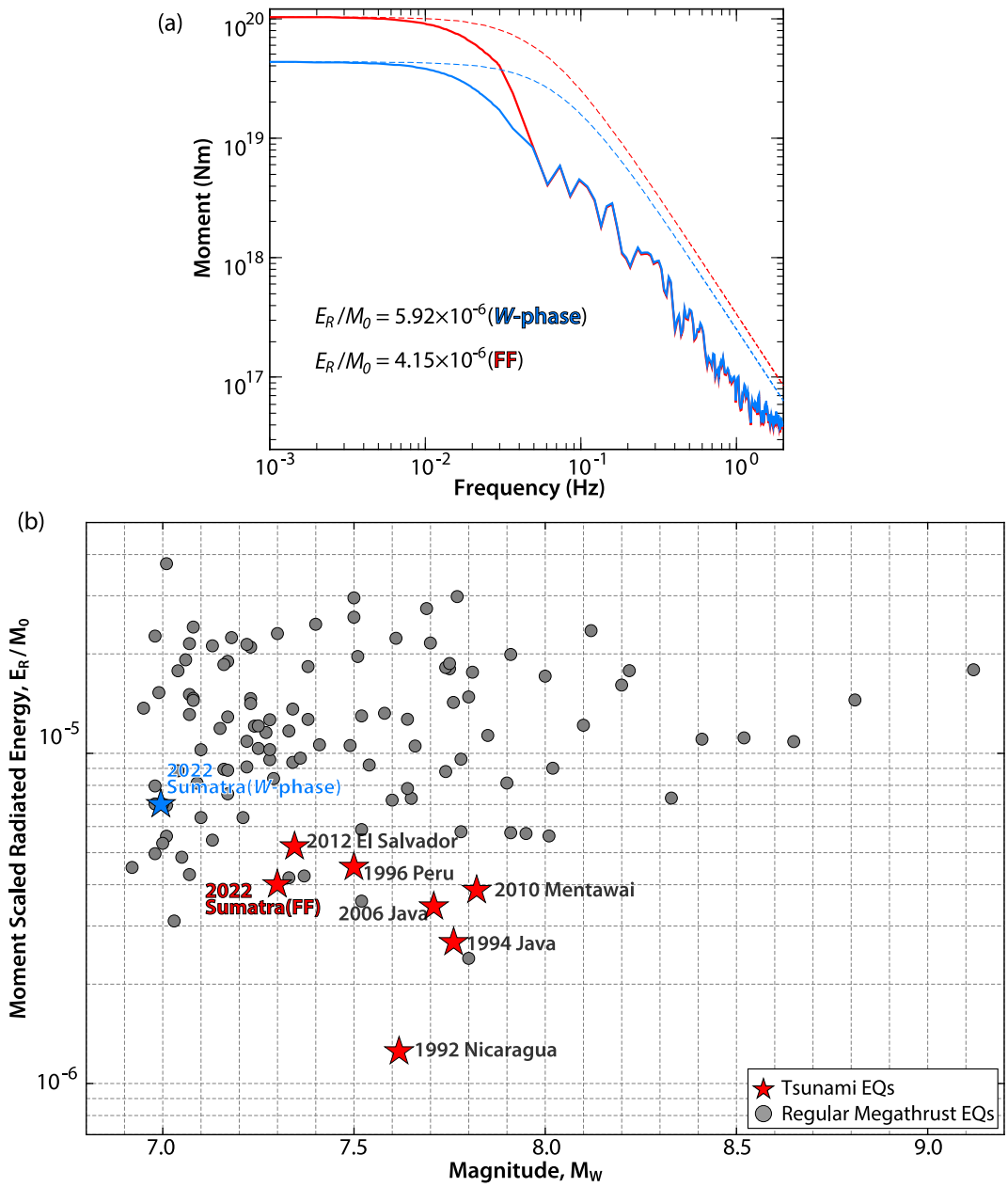

Figure 7. (a) Source spectra for the 2022 Sumatra event obtained from teleseismic *P* spectra and the moment-rate spectrum with different corrections of the seismic moment from the *W*-phase solution (bold dashed blue curve) and our model M04 (red curve), along with corresponding reference ω^{-2} source spectrum for 3 MPa stress drop (fine dashed curves). (b) Comparisons of moment-scaled radiated energy (E_R/M_0) for major tsunami earthquakes (stars) and other major megathrust earthquakes from 1990 to 2016 (gray dots; Ye et al., 2016a).

1.5 MPa, as was also the case for the 2010 M_W 7.8 Mentawai tsunami earthquake rupture zone (Figure 8b). We calculate the Coulomb failure stress change caused by the 2007 M_W 7.9 Pagai and 2010 M_W 7.8 Mentawai earthquakes along the slab interface, showing no significant increase the Coulomb failure stress change in the 2022 M_W 7.3 rupture zone (Figures 8c and 8d).

Thus, considering the cumulative contribution of stress changes due to the 2007 M_W 8.4 Bengkulu coseismic slip and the ensuing shallow afterslip in the shallow portion of the megathrust adjacent to the 2010 M_W 7.8 Mentawai and 2022 M_W 7.3 Sumatra earthquake rupture areas, it is evident that the 2022 M_W 7.3 Sumatra earthquake was

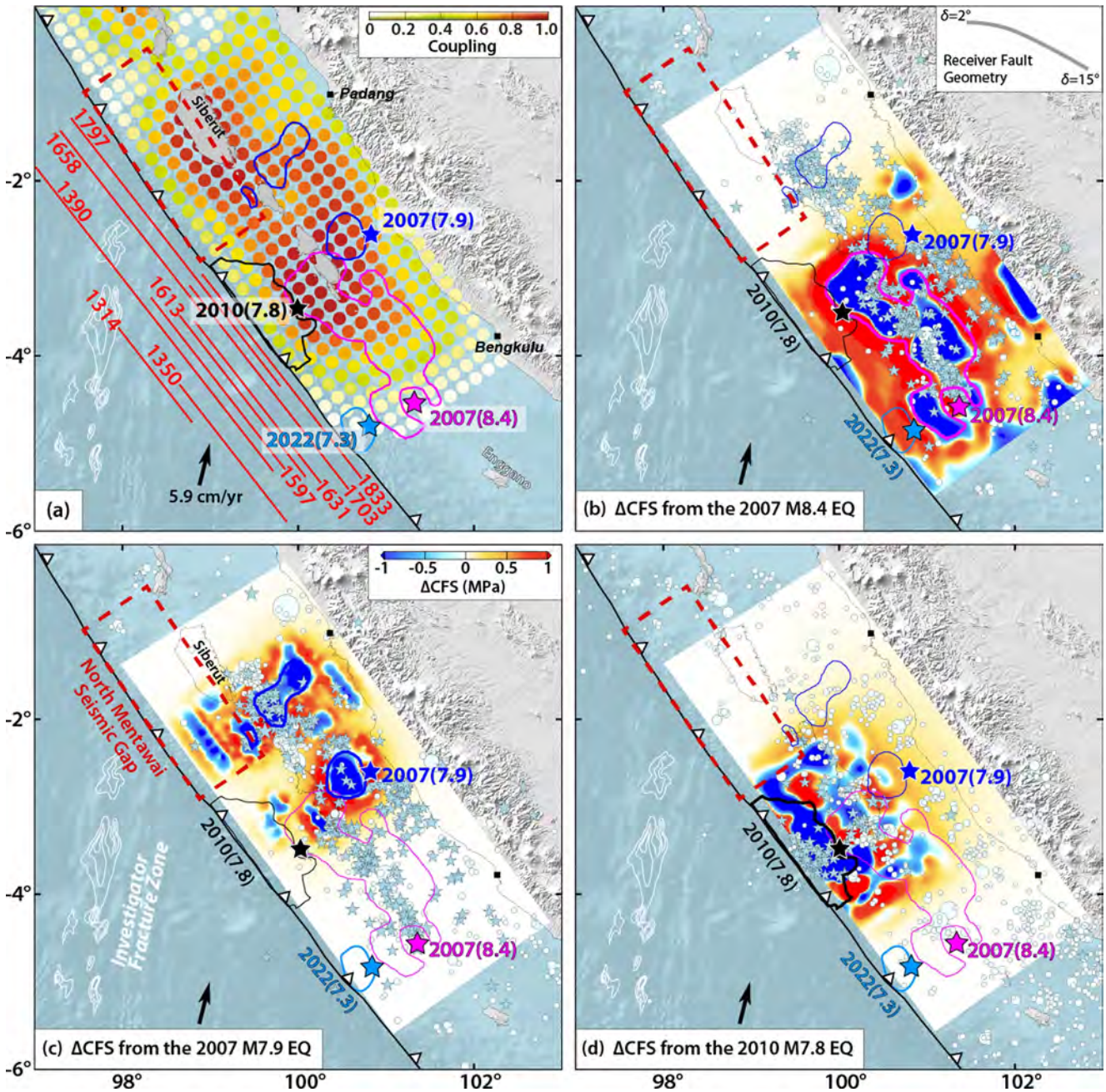

Figure 8. (a) Distribution of interseismic coupling (Chlieh et al., 2008) and historical great earthquakes in the Mentawai segment along the Sunda megathrust. Bold magenta, blue, black, and sky blue contours represent the rupture areas of the 2007 M_W 8.4 Bengkulu (Konca et al., 2008), 2007 M_W 7.9 Pagai (Konca et al., 2008), 2010 M_W 7.8 Mentawai (Yue, Lay, Rivera, Bai, et al., 2014), and 2022 M_W 7.3 Sumatra (this study) earthquakes with stars showing corresponding epicenters locations. Red bars show along strike extend for historical great earthquakes from Philibosian et al. (2017). (b)–(d) Coulomb stress changes along the megathrust from the coseismic slip of the 2007 M_W 8.4 Bengkulu (Konca et al., 2008), 2007 M_W 7.9 Pagai (Konca et al., 2008), and 2010 M_W 7.8 Mentawai (Yue, Lay, Rivera, Bai, et al., 2014) earthquakes, respectively. The receiver fault is along the slab interface using the Slab 2.0 model, having strike $\varphi = 324.0°$, rake $\lambda = 99.0°$ and a varying dip δ from 2.0° to 15.0°. Dark red dashed rectangular shows the North Mentawai Seismic Gap (Haridhi et al., 2018). White circles in (b) and (c) represent M4.5+ seismicity from the 2007 Bengkulu earthquake to the 2010 Mentawai earthquake. White circles in (d) represent M4.5+ seismicity from the 2010 Mentawai earthquake to the 2022 Sumatra earthquake. Light blue stars show M4.5+ aftershocks within 3 months after each mainshock.

promoted by the stress transfer from the deeper 2007 M_W 8.4 Bengkulu event. The downdip 2007 M_W 7.9 Pagai rupture exerts positive and negative Coulomb failure stress change in the North Mentawai Seismic Gap of ~0.5–1.0 MPa (Figure 8c), but the region was not as strongly or uniformly perturbed as the 2010 and 2022 rupture regions were by the 2007 M_W 8.4 Bengkulu event.

3. Discussion

Given that the near-trench megathrust was previously widely considered to be aseismic (e.g., Byrne et al., 1988; Scholz, 1998), the mechanism for shallow tsunami earthquakes remains unclear. A critical issue is whether there are local frictional heterogeneities in the shallow megathrust capable of accumulating sufficient stress to fail spontaneously in a tsunami earthquake. To that end, we consider the seismogenic behavior of the well-documented tsunami earthquakes since 1896 with good coverage and historical seismograms that have struck in different subduction zones globally.

We summarize the relatively sparse sampling provided by documented tsunami earthquakes, and their occurrence in both continental and island arc settings (Figure 9). There is a wide range of subducting lithosphere ages among the subduction zones that have hosted tsunami earthquakes. Figure 9 highlights one first-order correlation among almost all tsunami earthquakes which is that they have occurred in regions where siliceous pelagic sediments carpet the oceanic plates, but of course, only limited portions of such regions have produced recent tsunami earthquakes, so any causal relationship is unclear. Some destructive tsunamigenic earthquakes including shallow slip on the megathrust covered by siliceous pelagic sediments have been studied, such as the 2004 M_W 9.2 Sumatra-Andaman earthquake, for which a portion of the rupture extended close to the trench (e.g., Dean et al., 2010; Lay et al., 2005). Stevens et al. (2021) compile core samples from the International Ocean Discovery Program and the multichannel seismic reflection data, suggesting that the smectite-illite transformation and complete dehydration of silicates within thick basal sediments before subduction are essential factors contributing to the enhancement of the shallow slip. They found these processes produced substantial, dehydrated bulk sediment, along with fluid trapped by the low-permeability siliciclastic-fan and basal pelagic sediments, resulting in velocity-weakening behavior close to the trench in the southern part of the rupture area. Some regions like northern Honshu, where the 1896 Sanriku tsunami earthquake occurred, appear to have the red deep sea clay on the plate, and the same holds for the shallow rupture component of the 2011 Tohoku earthquake to the south of that event. Ujiie et al. (2013) suggest the abundant red deep sea clay retrieved from the plate-boundary décollement near the Japan trench, which consists primarily of ~78% smectite, exhibits very low shear strength under high-velocity friction experiments, leading to dynamically enhanced shallow slip under fluid-saturated and impermeable conditions. The large-slip region of the 2010 M_W 8.8 Maule (Chile) earthquake included two patches of slip that extended to the trench (e.g., Yue, Lay, Rivera, An, et al., 2014), where red deep sea clay is also found on the incoming Nazca Plate (Figure 9). The 2015 M_W 8.3 Illapel (Chile) earthquake to the north also involved coseismic slip extending up-dip to near the trench (e.g., Li et al., 2016). A 600-km long shallow very large-slip region for the 1957 Aleutian earthquake (Yamazaki et al., 2024) extended along the shallow megathrust in the eastern Aleutian Islands in a region where siliceous pelagic sediments are found on the incoming plate (Figure 9).

However, it is difficult to conclude whether the widespread occurrence of sediments can govern the genesis of tsunami earthquakes individually due to the very limited tsunami earthquake sampling. Here, we discuss the possibility that combined effects of the trench pelagic sediment and rough morphological condition of subduction zones may influence seismic behavior in the shallow megathrust. Figure 9b illustrates that eight tsunami earthquakes occurred in subduction zones with an erosive margin (Kuril, northeastern Japan, Alaska-Aleutian, Chile-Peru, Middle America), while the remainder occurred in zones with an accretionary margin (Sunda, Java). These tsunami earthquake occurrences in both erosive and accretionary subduction zones suggest a lack of clear systematic correlation between tsunami earthquake occurrence and subduction tectonic framework. Excluding the 1907 Sumatra event which has some location uncertainty, the area of the 2010 Mentawai and 2022 Sumatra earthquakes has a maximum sediment thickness of ~1100 m, while other tsunami earthquake regions host little or no sediment in the trench.

Figure 10 shows cross-sections with relocated hypocenters and slip regions for seven well-recorded tsunami earthquakes since 1990. These events occurred in regions with either thick sediment on the incoming plate (2022 Sumatra, 2010 Mentawai, 2006 Java, 1994 Java) or rough bathymetry with minor sediment (2012 El Salvador, 1992 Nicaragua, 1996 Peru). Rough seafloor topography, such as horst-and-graben structures and subducted

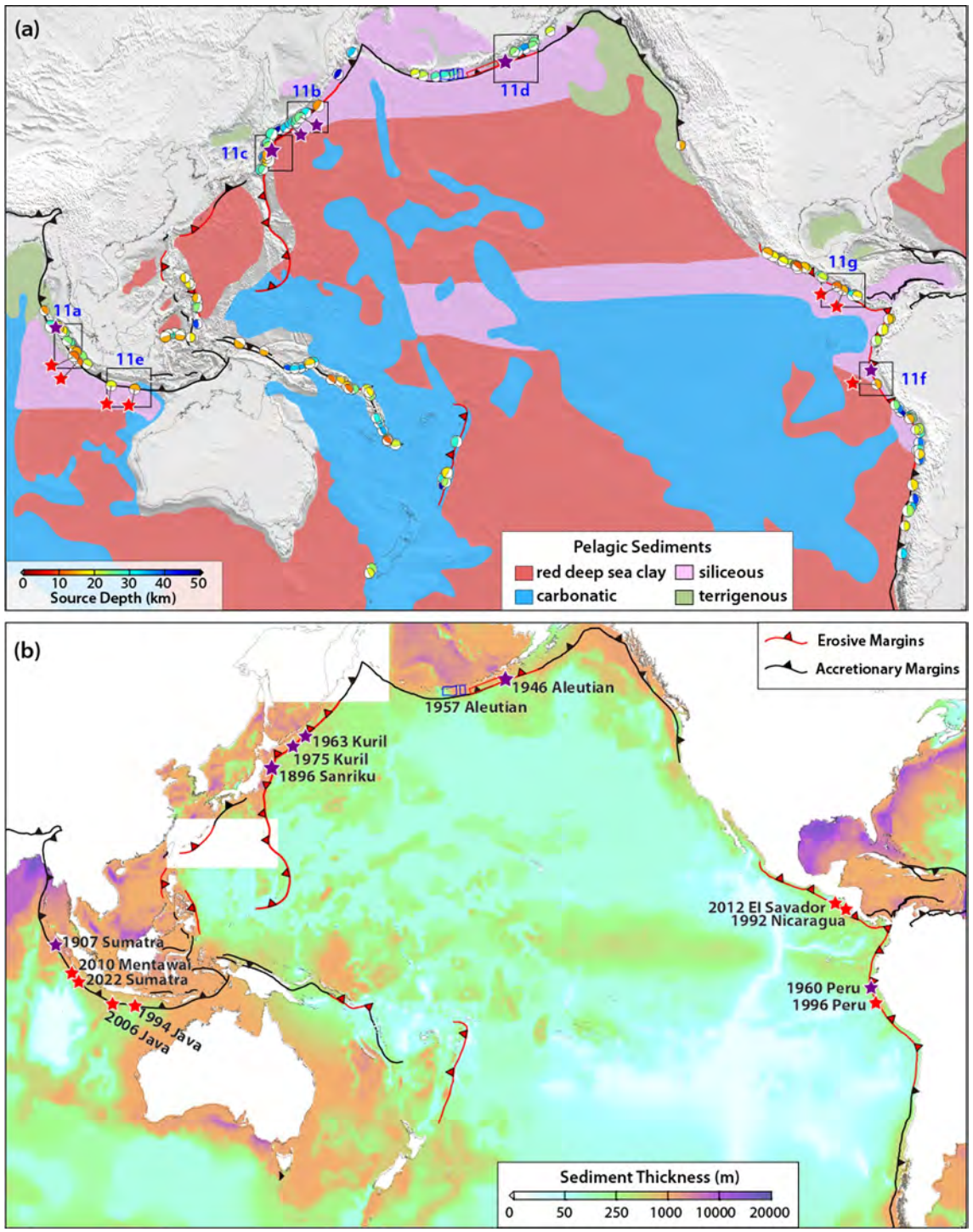

Figure 9. The distribution of well-known tsunami earthquakes globally along with pelagic sediment and sediment thickness. Focal mechanisms in (a) show 172 M6.9+ megathrust events since 1976 from the Global Centroid Moment Tensor catalog, coded by the centroid depth. Red stars indicate the well-documented tsunami earthquakes with broadband source spectrum for the 2022 Sumatra earthquake (this study) and six others since 1990 (Ye et al., 2016b). Six purple stars show the inferred tsunami earthquakes of the 1896 Sanriku (Kanamori, 1972), 1907 Sumatra (Kanamori et al., 2010), 1946 Aleuntian (Kanamori, 1972), 1960 Peru (Pelayo & Wiens, 1992), 1963 and 1975 Kuril (Fukao, 1979; Pelayo & Wiens, 1992), plotted at the USGS-NEIC location. Three boxes show main slip patches for the 1957 Aleutian earthquake with the red box indicating a 600-km long shallow very large-slip region (Yamazaki et al., 2024). The pelagic sediment distribution is modified from Jenkyns (1986), which was adapted from Davies and Gorsline (1976). The sediment thickness data is from Whittaker et al. (2013). Barbed lines represent subducting boundary types (black: accretionary; red: erosive), modified from Noda (2016). Subduction zones with tsunami earthquakes displayed in Figure 11 are outlined by black boxes (a–g).

seamounts, is common in regions with tsunami earthquake occurrences (Figures 9 and 10), as is strong deformation of the outer wedge (Qiu & Barbot, 2022). The rough seafloor topography may foster thick, fragmented, and faulted plate-boundary shear zones when subducted, enhancing contact area with the overriding plate and accumulating patchy stress in the shallow megathrust (e.g., Polet & Kanamori, 2000; Tanioka et al., 1997). The presence of incoming sediment deposits likely reduces the interface frictional strength, as in the case of abundant smectite observed in the 2011 Tohoku rupture area, favoring the possibility of shallow tsunami earthquakes (e.g., Geersen, 2019; Moore et al., 2015; Polet & Kanamori, 2000; Ujiie et al., 2013). Given that tsunami earthquakes have often involved large slip with correspondingly long recurrence intervals, the available sampling from recent seismic history has to be considered with caution, as we proceed to discuss some other aspects of these events.

As shown in this study, the 2022 Sumatra tsunami earthquake ruptured ~50 km along strike of the shallow portion of the Sunda trench, with all significant slip locating shallower than ~10 km (from 2 to 8 km into rock), which has been defined as Domain A in the depth-varying segmentation model (Lay et al., 2012). The rupture is located up-dip of the Domain B (15–35 km deep) 2007 M_W 8.4 Bengkulu event. This geometry is similar to that of the 2010 M_W 7.8 Mentawai tsunami earthquake to the northwest and that of the 1907 M_W 7.8 Sumatra tsunami earthquake (Figure 11a and Figure S15 in Supporting Information S1). In the shallow megathrust between the 2010 Mentawai and 2022 Sumatra events, Tsang et al. (2016) suggests that ~1.5 m of aseismic afterslip of the 2007 events occurred, consistent with our Coulomb failure stress change pattern. Thus, it appears that there is little likelihood of another tsunami earthquake occurring up-dip of the Bengkulu event in the near future. The patchy distribution of seismic and aseismic slip along the shallow Sumatra subduction zone suggests a role for small-scale structural heterogeneity influencing the conditions for localized tsunami earthquake occurrence amidst adjacent regions of slow slip.

Similarly, the 1963 M_W 7.8 and 1975 M_W 7.7 Kuril earthquakes ruptured near the Kuril trench (Fukao, 1979; Pelayo & Wiens, 1992; Pérez, 2000), where the deep megathrust has experienced two great megathrust Domain B events, including the 1963 M_W 8.5 and 1969 M_W 8.2 Kuril events (Figure 11b and Figure S16 in Supporting Information S1). Notably, the 1963 M_W 7.8 earthquake is an aftershock one week after the 1963 M_W 8.5 earthquake, probably resulting from stress transfer from the deeper rupture zone to the shallower megathrust, or possibly onto a splay fault. The outer wedge is only about 15 km wide in this region (Qiu & Barbot, 2022).

Two great tsunami earthquakes: the 1896 M_W 8.1 Sanriku and the shallow component of the 2011 M_W 9.1 Tohoku events, ruptured the Domain A segment of the Japan trench along Honshu, which has also experienced numerous ruptures confined to Domains B and C (35–50 km deep) (Figure 11c and Figure S17 in Supporting Information S1). The shallow plate interface in this region is very irregular and there are multiple deformation structures in the ~30 km wide outer wedge (Qiu & Barbot, 2022). The coseismic rupture extent spanning Domains A, B, and C for the 2011 event coincides with the region of estimated strong megathrust coupling area and afterslip in the deeper zone (Ozawa et al., 2011), indicating that balanced slip accommodation exists between the shallower and deeper portion of this region. The 1896 event represents spontaneous rupture of Domain A without deeper coseismic slip, and the down-dip region appears to have little slip deficit (e.g., Ye et al., 2011), so it is possible that stress shadowing by the deeper well-locked region to the south prevented a similar Domain A rupture prior to the 2011 event. This illustrates a major challenge of evaluating whether tsunami earthquakes can occur in those circum-Pacific regions without historical examples.

Another tsunami earthquake that spontaneously ruptured Domain A is the 1946 M_W 8.6 Aleutian Islands event, which occurred adjacent to the Shumagin Island region of the Aleutian-Alaska trench. Qiu and Barbot (2022) infer a very wide (~50 km) outer trench wedge in this region. There is an along-strike offset in the large-slip areas of earthquakes between the 1946 event and deeper (Domains B–C) 2020 M_W 7.8 Shumagin and the 2021 M_W 8.2 Chignik earthquakes (Figure 11d and Figure S18 in Supporting Information S1). Geodetic slip deficit appears to be very low along the deeper megathrust near the 1946 event (Freymueller & Beavan, 1999), so this may be a region where only Domain A ruptures occur, and the 1957 rupture zone to the west had 600 km long rupture of Domain A (Yamazaki et al., 2024). Aftershocks of the 2021 event distribute in the shallow portion and overlap its afterslip area at shallower depths (Brooks et al., 2023), also suggesting some strain balancing across different depths. The shallow region up-dip of the 2020 Shumagin earthquake did not have coseismic slip, but did show some slip deficit accumulation prior to the event (DeSanto et al., 2023). Some uncertainty remains regarding the seismic potential of the shallow part of the former Shumagin gap and the Chignik region, due to the lack of

shallow seismicity and limited resolution of interplate coupling along the dip in this region (e.g., Liu et al., 2023; Xiao et al., 2021; Ye et al., 2021, 2022).

Some other tsunami earthquakes have occurred in regions that experienced no historic downdip Domain B or Domain C events. The 1994 M_W 7.8 and 2006 M_W 7.7 Java events ruptured the Java trench, where the deeper megathrust region is generally regarded as weakly coupled (e.g., Scholz & Campos, 2012) with no history of great megathrust events (Figure 11e and Figure S17 in Supporting Information S1). Both events have low moment-scaled radiated energy, low apparent stress, and large slip in the depth range of 6–22 km (Ye et al., 2016a). They also produced predominantly normal-faulting aftershocks including several seaward of the large-slip zones (e.g., Abercrombie et al., 2001; Ammon et al., 2006; Bilek & Engdahl, 2007), which has been related to shallow ruptures (Sladen & Trevisan, 2018). The 1994 and 2006 Java events probably included rupture of localized unstable patches with strong coupling possibly associated with subducted seamounts or bathymetry (e.g., Abercrombie et al., 2001; Ammon et al., 2006; Bilek & Engdahl, 2007). The outer trench wedge along this accretionary boundary is estimated to be about 40 km wide in this region (Qiu & Barbot, 2022).

The 1960 M_W 7.6 and 1996 M_W 7.5 Peru events ruptured the northern Peru trench, which is an erosive boundary that has low seismic coupling in general (e.g., Scholz & Campos, 1995) without any recorded deep megathrust events in Domains B and C (Figure 11f and Figure S20 in Supporting Information S1). The rupture extent of the 1960 event is correlated with a locally strong shallow coupling region, but the 1996 event cannot be assessed due to the low-resolution coupling model (e.g., Villegas-Lanza et al., 2016). The outer wedge width is estimated as about 20 km near the 1996 event by Qiu and Barbot (2022). The 1992 M_W 7.6 Nicaragua and the 2012 M_W 7.3 El Salvador events ruptured patchy areas in the shallow portion of the Middle American megathrust along Nicaragua and El Salvador (Figure 11g and Figure S21 in Supporting Information S1). These are along an erosive margin as well, with ∼20 km wide outer wedge (Qiu & Barbot, 2022). The down-dip regions don't appear to be strongly coupled, but the presence of an upper plate sliver complicates this inference (Ye et al., 2013). There are other moderate ruptures showing regular seismic behavior along the strike in the Middle American megathrust, such as the 2012 M_W 7.6 Costa Rica event in Domain B and the 2012 M_W 7.4 Guatemala event in Domain C (e.g., Ye et al., 2013).

The documented tsunami earthquakes occurred in diverse megathrust environments, which can be roughly divided into two categories. One type includes regions where tsunami earthquake rupture up-dip of major or great megathrust events at deeper depths, with the deeper ruptures likely promoting triggering (i.e., clock-advance) of the ruptures at shallow depths, if not coseismic rupture as for the 2011 Tohoku event. The deeper portion of megathrust, when locked, likely casts a stress shadow for the shallow depth megathrust, regardless of the frictional properties at shallow depth (Lindsey et al., 2021). The heterogeneous coupling and seismogenic capability in the shallow Domain A region indicated by this type of tsunami earthquake may be attributed to the presence of fragmented and faulted shear zones resulting from the combined effects of sediments and rough topography, as discussed previously. It is unclear why immediate rupture of the shallow region does not always take place when deeper ruptures occur, as was the case for the 3 and 15 years delays for the 2010 Mentawai and 2022 Sumatra events following the 2007 Bengkulu earthquake; sluggish poroelastic and viscoelastic effects and additional stress increments from afterslip may be required to push the patchy shallow interface to subsequent failure. The presence of low-velocity sedimentary layers deposited on the wedge may cause dynamic interactions with the rupture that allow deeper ruptures to have more shallow slip (Li et al., 2023), but such superimposed layers are not evident in the steeply dipping outer wedges where isolated tsunami earthquake occur (Qiu & Barbot, 2022). Another type of tsunami earthquake includes regions where tsunami earthquakes occur in Domain A without having large events in Domains B and C. In these regions, localized asperities in the shallow megathrust are able to accumulate stress for a long time and fail spontaneously. The occurrence of such ruptures does not preclude some degree of stress shadowing from slip deficit accumulation and eventual rupture of deeper Domains B and C; the earthquake catalog may simply be too short to provide a full picture of the process. In these regions, long-term seafloor geodetic monitoring is required to assess the potential for tsunami earthquakes as well as to detect strain accumulation that may result in deeper ruptures.

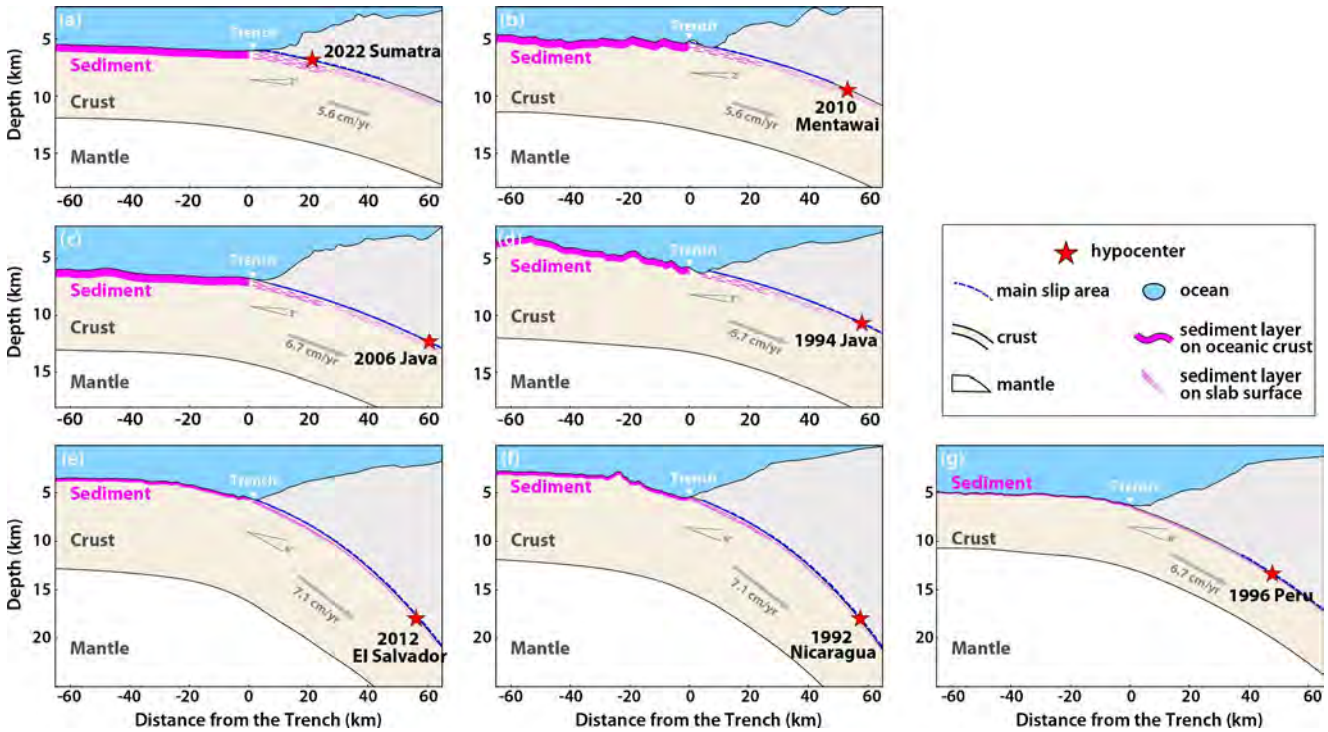

Figure 10. Profiles for seven regions that experienced well-documented tsunami earthquakes since 1990, including (a) 2022 M_W 7.3 Sumatra, (b) 2010 M_W 7.8 Mentawai, (c) 2006 M_W 7.7 Java, (d) 1994 M_W 7.8 Java, (e) 2012 M_W 7.3 El Salvador, (f) 1992 M_W 7.6 Nicaragua, and (e) 1996 M_W 7.6 Peru. Red stars show relocated hypocenters (Details in Table S4 and Figures S9–S14 in Supporting Information S1), with blue dashed curves indicating the main slip area. Each profile is constructed using GEBCO 2023 bathymetry data, sediment thickness data (Whittaker et al., 2013), and the Slab 2.0 model. The crustal thickness is derived from the Crust 1.0 model. The amplitude of the seafloor bathymetry is amplified by a factor of 3. Depths in the Slab 2.0 model are manually adjusted to match the trench depth from the bathymetry data.

4. Conclusion

The 2022 M_W 7.3 Sumatra underthrusting earthquake ruptured the megathrust region up-dip of the 2007 M_W 8.4 Bengkulu rupture on a shallow, sub-horizontal fault plane. The major slip patch had a peak slip of 4.1 m, located at depths shallower than 10 km, adjacent to the shallow afterslip zone of the 2007 major events. It exhibits common features of tsunami earthquakes, including a depletion in high-frequency seismic wave radiation, low moment-scaled radiated energy of 4.15×10^{-6}, and low source region rigidity of 23 GPa. Calculation of the Coulomb failure stress suggests that the 2022 M_W 7.3 Sumatra event was probably promoted by stress transfer resulting from the coseismic slip and afterslip of the 2007 Bengkulu event. We consider tsunami earthquakes that occurred in the Sumatra, offshore Honshu, Alaska-Aleutian, Peru, Java, and Middle American subduction zones using the depth-varying megathrust subdivision of Lay et al. (2012) with the combined effects of sediments and rough morphological. The diverse slip modes in different subduction zones reveal substantial complexity in the shallow megathrust, including ruptures in Domain A that may be induced by deeper ruptures in Domains B and C, or may occur independently due to the long-term stress accumulation. The presence of tsunami earthquakes in both erosive and accretionary subduction zones suggests a lack of distinct systematic correlation between their occurrence and subduction tectonic framework. The width of the strongly deformed outer wedge of the accretionary prism appears to correlate with tsunami excitation, with coseismic splay faulting within the wedge possibly contributing to tsunami excitation (Qiu & Barbot, 2022), but the shallow megathrust supports strain accumulation that releases in tsunami earthquakes. Furthermore, the combination of pelagic clay and siliceous sediments on the subducting ocean floor, which are subducted or accumulate in the outer sedimentary wedge, and rough seafloor topography may result in the heterogeneous coupling in the Domain A region, which appears to play important roles in controlling the genesis of tsunami earthquake along Sumatra and other regions. However, the variability of structures among limited recorded tsunami earthquakes obscures the factors that control tsunami earthquake occurrence.

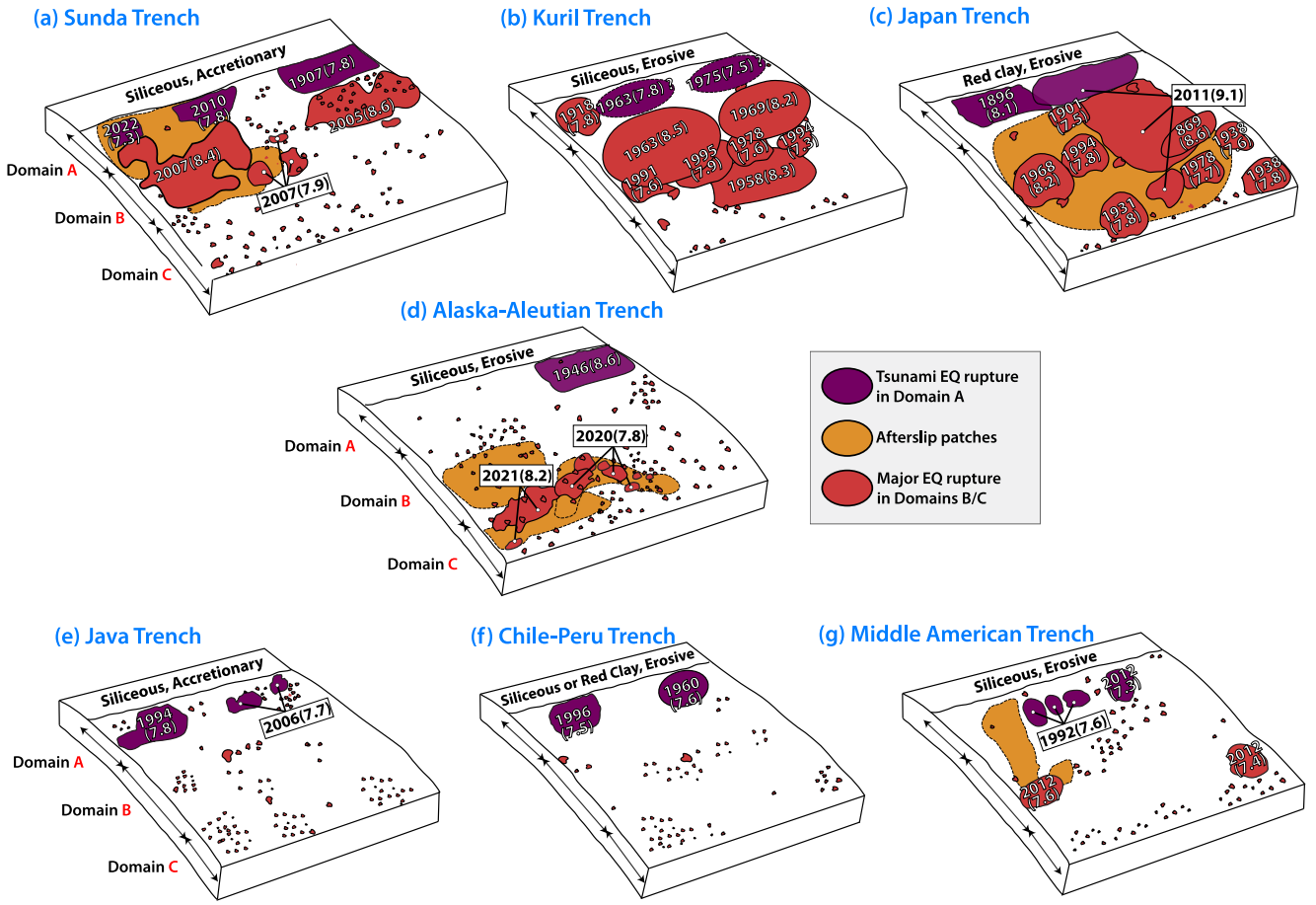

Figure 11. Schematics for subduction zones with major tsunami earthquakes. (a) Sumatra subduction zone with the 1907 M_W 7.8 Sumatra (Kanamori et al., 2010; Martin et al., 2019), 2005 M_W 8.6 Nias (Hsu et al., 2006), 2007 M_W 8.4 Bengkulu (Konca et al., 2008), the 2007 M_W 7.9 Pagai (Konca et al., 2008), the 2010 M_W 7.8 Mentawai (Yue, Lay, Rivera, Bai, et al., 2014) and the 2022 M_W 7.3 Sumatra events (this study). (b) Kuril subduction zone with the 1963 M_W 7.8, 1975 M_W 7.7, 1969 M_W 8.2, 1963 M_W 8.5, and 1995 M_W 7.9 Kuril events (Fukao, 1979; Pelayo & Wiens, 1992; Pérez, 2000). (c) Offshore Honshu subduction zone with the 1896 M_W 8.1 Sanriku, the 1978 M_W 7.7 Miyagi-oki, and the 2011 M_W 9.1 Tohoku events (Ye et al., 2021). (d) Alaska-Aleutian subduction zone with the 1946 M_W 8.6 Alaska, the 2020 M_W 7.8 Shumagin (Liu et al., 2023), and the 2021 M_W 8.2 Chignik events (Ye et al., 2022). (e) Java subduction zone with the 1994 M_W 7.8 Java and the 2006 M_W 7.7 Java events (Bilek & Engdahl, 2007). (f) Chile-Peru subduction zone with the 1960 M_W 7.6 Peru events (Bilek, 2010; Pelayo & Wiens, 1992) and the 1996 M_W 7.5 Peru (Ihmlé et al., 1998). (g) Middle American subduction zone with the 1992 M_W 7.6 Nicaragua, the 2012 M_W 7.3 EI Salvador, the 2012 M_W 7.4 Guatemala (Ye et al., 2013), and the 2012 M_W 7.6 Costa Rica events (Yue et al., 2013). Red polygons indicate major earthquake ruptures in Domains B and C; Purple polygons indicate tsunami earthquakes in the shallow depth; and orange polygons indicate afterslip patches, such as for the 2007 M_W 8.4 Bengkulu (Tsang et al., 2016), the 2011 M_W 9.1 Tohoku (Ozawa et al., 2011), the 2020 M_W 7.8 Shumagin, the 2021 M_W 8.2 Chignik (Brooks et al., 2023), and 2012 M_W 7.6 Costa Rica (Hobbs et al., 2017) events.

Conflict of Interest

The authors declare no conflicts of interest relevant to this study.

Data Availability Statement

Global seismic data were downloaded from the Incorporated Research Institutions for Seismology (IRIS) data management center (http://ds.iris.edu/wilber3/find_event), including stations from Global Seismographic Network code II (Scripps Institution of Oceanography [SIO], 1986, available at https://doi.org/10.7914/SN/II), IU (ASL/USGS, 1988, available at https://doi.org/10.7914/SN/IU), and International Federation of Digital Seismic Networks (FDSN) code AU (Geoscience Australia, 2021, available at https://doi.org/10.26186/144675), AW (Alfred Wegener Institute For Polar And Marine Research [AWI], 1993, available at https://doi.org/10.14470/NJ617293), FN (Sodankylä Geophysical Observatory/University Of Oulu (Finland), 1980, available at https://doi.org/10.14470/SA879454), G (Institut de physique du globe de Paris (IPGP) & École et Observatoire des Sciences de la Terre de Strasbourg (EOST), 1982, available at https://doi.org/10.18715/GEOSCOPE.G), GE

(GEOFON Data Centre, 1993, available at https://doi.org/10.14470/TR560404), GT (Albuquerque Seismological Laboratory (ASL)/USGS, 1993, available at https://doi.org/10.7914/SN/GT), HU [Kövesligethy Radó Seismological Observatory (Geodetic And Geophysical Institute, Research Centre For Astronomy And Earth Sciences, Hungarian Academy Of Sciences), 1992, available at https://doi.org/10.14470/UH028726], IC (Albuquerque Seismological Laboratory (ASL)/USGS, 1992, available at https://doi.org/10.7914/SN/IC), JP, KC (Central Asian Institute for Applied Geosciences, 2008, available at https://doi.org/10.7914/SN/KC), MN (MedNet Project Partner Institutions, 1990, available at https://doi.org/10.13127/sd/fbbbtdtd6q) and PS. The tsunami observation at Cocos Island tide gauge station is downloaded from the European Commission Joint Research Centre, ISPRA, Space, Security and Migration Directorate (JRC, https://webcritech.jrc.ec.europa.eu/tad_server/). The high-resolution bathymetry BATNAS data set is downloaded from Indonesian Geospatial Information Agency (https://tanahair.indonesia.go.id/portal-web/unduh/batnas). We thank the facilities of IRIS Data Services, and specifically the IRIS Data Management Center, which were used for access to waveforms, related metadata, and/or derived products used in this study. Data Services are funded through the Seismological Facilities for the Advancement of Geoscience (SAGE) Award of the National Science Foundation under Cooperative Support Agreement EAR-1851048. Global Centroid Moment Tensor solutions are from https://www.globalcmt.org/CMTsearch.html. The USGS-NEIC catalog is from https://earthquake.usgs.gov/earthquakes/search/. All links were last accessed on 29 October 2024.

Acknowledgments

We thank Prof. Bin Chen at SUSTech for the discussion about the pelagic sediment, Prof. Haipeng Luo at SUSTech for the discussion about the tsunami earthquakes. We thank editor Rachel Abercrombie, associate editor Yihe Huang, and two anonymous reviewers for their constructive comments. The work was supported in part by National Key Research and Development Program of China 2023YFF0803200 (L. Y.), National Natural Science Foundation of China 42376212 (Y. B.), National Natural Science Foundation of China 42074048 (S. X.), and National Science Foundation Grant EAR1802364 (T. L.).

References

Abercrombie, R. E., Antolik, M., Felzer, K., & Ekström, G. (2001). The 1994 Java tsunami earthquake: Slip over a subducting seamount. *Journal of Geophysical Research: Solid Earth*, *106*(B4), 6595–6607. https://doi.org/10.1029/2000jb900403

Albuquerque Seismological Laboratory (ASL)/U.S. Geological Survey (USGS). (1988). Global seismograph network—IRIS/USGS [Dataset]. International Federation of Digital Seismograph Networks. https://doi.org/10.7914/SN/IU

Albuquerque Seismological Laboratory (ASL)/USGS. (1992). New China Digital Seismograph Network [Dataset]. International Federation of Digital Seismograph Networks. https://doi.org/10.7914/SN/IC

Albuquerque Seismological Laboratory (ASL)/USGS. (1993). Global Telemetered Seismograph Network (USAF/USGS) [Dataset]. International Federation of Digital Seismograph Networks. https://doi.org/10.7914/SN/GT

Alfred Wegener Institute For Polar And Marine Research (AWI). (1993). (AW) AWI Network Antarctica [Dataset]. GFZ Data Services. https://doi.org/10.14470/NJ617293

Ammon, C. J., Ji, C., Thio, H. K., Robinson, D., Ni, S., Hjorleifsdottir, V., et al. (2005). Rupture process of the 2004 Sumatra-Andaman earthquake. *Science*, *308*(5725), 1133–1139. https://doi.org/10.1126/science.1112260

Ammon, C. J., Kanamori, H., Lay, T., & Velasco, A. A. (2006). The 17 July 2006 Java tsunami earthquake. *Geophysical Research Letters*, *33*(24). https://doi.org/10.1029/2006gl028005

Bai, Y., Cheung, K. F., Yamazaki, Y., Lay, T., & Ye, L. (2014). Tsunami surges around the Hawaiian Islands from the 1 April 2014 North Chile M_w 8.1 earthquake. *Geophysical Research Letters*, *41*(23), 8512–8521. https://doi.org/10.1002/2014gl061686

Bai, Y., Ye, L., Yamazaki, Y., Lay, T., & Cheung, K. F. (2018). The 4 May 2018 M_w 6.9 Hawaii Island earthquake and implications for tsunami hazards. *Geophysical Research Letters*, *45*(20), 11–040. https://doi.org/10.1029/2018gl079742

Bilek, S. L. (2010). Invited review paper: Seismicity along the South American subduction zone: Review of large earthquakes, tsunamis, and subduction zone complexity. *Tectonophysics*, *495*(1–2), 2–14. https://doi.org/10.1016/j.tecto.2009.02.037

Bilek, S. L., & Engdahl, E. R. (2007). Rupture characterization and aftershock relocations for the 1994 and 2006 tsunami earthquakes in the Java subduction zone. *Geophysical Research Letters*, *34*(20), L20311. https://doi.org/10.1029/2007gl031357

Bilek, S. L., & Lay, T. (2002). Tsunami earthquakes possibly widespread manifestations of frictional conditional stability. *Geophysical Research Letters*, *29*(14), 1673. https://doi.org/10.1029/2002gl015215

Borrero, J. C., Weiss, R., Okal, E. A., Hidayat, R., Suranto, Arcas, D., & Titov, V. V. (2009). The tsunami of 2007 September 12, Bengkulu province, Sumatra, Indonesia: Post-tsunami field survey and numerical modelling. *Geophysical Journal International*, *178*(1), 180–194. https://doi.org/10.1111/j.1365-246x.2008.04058.x

Brooks, B. A., Goldberg, D., DeSanto, J., Ericksen, T. L., Webb, S. C., Nooner, S. L., et al. (2023). Rapid shallow megathrust afterslip from the 2021 M8. 2 Chignik, Alaska earthquake revealed by seafloor geodesy. *Science Advances*, *9*(17), eadf9299. https://doi.org/10.1126/sciadv.adf9299

Byrne, D. E., Davis, D. M., & Sykes, L. R. (1988). Loci and maximum size of thrust earthquakes and the mechanics of the shallow region of subduction zones. *Tectonics*, *7*(4), 833–857. https://doi.org/10.1029/tc007i004p00833

Central Asian Institute for Applied Geosciences. (2008). Central Asian Seismic Network of CAIAG [Dataset]. International Federation of Digital Seismograph Networks. https://doi.org/10.7914/SN/KC

Cheung, K. F., Lay, T., Sun, L., & Yamazaki, Y. (2022). Tsunami size variability with rupture depth. *Nature Geoscience*, *15*(1), 33–36. https://doi.org/10.1038/s41561-021-00869-z

Chlieh, M., Avouac, J. P., Sieh, K., Natawidjaja, D. H., & Galetzka, J. (2008). Heterogeneous coupling of the Sumatran megathrust constrained by geodetic and paleogeodetic measurements. *Journal of Geophysical Research*, *113*(B5). https://doi.org/10.1029/2007jb004981

Davies, T., & Gorsline, D. (1976). Oceanic sediments and sedimentary processes. In J. Riley & K. Chester (Eds.), *Chemical Oceanography* (Vol. 5, pp. 1–80). Academic Press.

Dean, S. M., McNeill, L. C., Henstock, T. J., Bull, J. M., Gulick, S. P., Austin Jr, J. A., et al. (2010). Contrasting décollement and prism properties over the Sumatra 2004–2005 earthquake rupture boundary. *Science*, *329*(5988), 207–210. https://doi.org/10.1126/science.1189373

DeMets, C., Gordon, R. G., & Argus, D. F. (2010). Geologically current plate motions. *Geophysical Journal International*, *181*(1), 1–80. https://doi.org/10.1111/j.1365-246x.2009.04491.x

DeSanto, J. B., Webb, S. C., Nooner, S. L., Schmidt, D. A., Crowell, B. W., Brooks, B. A., et al. (2023). Limited shallow slip or the 2020 Simeonof earthquake, Alaska, constrained by GNSS-Acoustic. *Geophysical Research Letters*, *50*(16), e2023GL105045. https://doi.org/10.1029/2023gl105045

Du, Y., Ma, S., Kubota, T., & Saito, T. (2021). Impulsive tsunami and large runup along the Sanriku Coast of Japan produced by an inelastic wedge deformation model. *Journal of Geophysical Research: Solid Earth*, *126*(8), e2021JB022098. https://doi.org/10.1029/2021jb022098

Freymueller, J. T., & Beavan, J. (1999). Absence of strain accumulation in the western Shumagin segment of the Alaska subduction zone. *Geophysical Research Letters*, *26*(21), 3233–3336. https://doi.org/10.1029/1999gl008356

Fujie, G., Kodaira, S., Nakamura, Y., Morgan, J. P., Dannowski, A., Thorwart, M., et al. (2020). Spatial variations of incoming sediments at the northeastern Japan arc and their implications for megathrust earthquakes. *Geology*, *48*(6), 614–619. https://doi.org/10.1130/g46757.1

Fukao, Y. (1979). Tsunami earthquakes and subduction processes near deep-sea trenches. *Journal of Geophysical Research: Solid Earth*, *84*(B5), 2303–2314. https://doi.org/10.1029/jb084ib05p02303

Gabuchian, V., Rosakis, A. J., Bhat, H. S., Madariaga, R., & Kanamori, H. (2017). Experimental evidence that thrust earthquake ruptures might open faults. *Nature*, *545*(7654), 336–339. https://doi.org/10.1038/nature22045

Geersen, J. (2019). Sediment-starved trenches and rough subducting plates are conducive to tsunami earthquakes. *Tectonophysics*, *762*, 28–44. https://doi.org/10.1016/j.tecto.2019.04.024

Geersen, J., McNeill, L., Henstock, T. J., & Gaedicke, C. (2013). The 2004 Aceh-Andaman earthquake: Early clay dehydration controls shallow seismic rupture. *Geochemistry, Geophysics, Geosystems*, *14*(9), 3315–3323. https://doi.org/10.1002/ggge.20193

GEOFON Data Centre. (1993). GEOFON Seismic Network [Dataset]. GFZ Data Services. https://doi.org/10.14470/TR560404

Geoscience Australia. (2021). *Australian National Seismograph Network Data Collection (Version 2.0, September 2018)*. Commonwealth of Australia (Geoscience Australia). https://doi.org/10.26186/144675

Gulick, S. P., Austin Jr, J. A., McNeill, L. C., Bangs, N. L., Martin, K. M., Henstock, T. J., et al. (2011). Updip rupture of the 2004 Sumatra earthquake extended by thick indurated sediments. *Nature Geoscience*, *4*(7), 453–456. https://doi.org/10.1038/ngeo1176

Haridhi, H. A., Huang, B. S., Kuo-Liang, W., Denzema, D., Prasetyo, R. A., & Chao-Shing, L. (2018). A study of large earthquake sequences in the Sumatra subduction zone and its possible implications. *TAO: Terrestrial, Atmospheric and Oceanic Sciences*, *29*(6), 6.

Hartzell, S. H., & Heaton, T. H. (1983). Inversion of strong ground motion and teleseismic waveform data for the fault rupture history of the 1979 Imperial Valley, California, earthquake. *Bulletin of the Seismological Society of America*, *73*(6A), 1553–1583. https://doi.org/10.1785/bssa07306a1553

Hayes, G. P., Moore, G. L., Portner, D. E., Hearne, M., Flamme, H., Furtney, M., & Smoczyk, G. M. (2018). Slab2, a comprehensive subduction zone geometry model. *Science*, *362*(6410), 58–61. https://doi.org/10.1126/science.aat4723

Heaton, T. H., & Heaton, R. E. (1989). Static deformation from point sources and force couples located in welded Poissonian half-spaces: Implications for seismic moment tensors. *Bulletin of the Seismological Society of America*, *79*, 813–841.

Hill, E. M., Borrero, J. C., Huang, Z., Qiu, Q., Banerjee, P., Natawidjaja, D. H., et al. (2012). The 2010 M_W 7.8 Mentawai earthquake: Very shallow source of a rare tsunami earthquake determined from tsunami field survey and near-field GPS data. *Journal of Geophysical Research: Solid Earth*, *117*(B6). https://doi.org/10.1029/2012jb009159

Hobbs, T. E., Kyriakopoulos, C., Newman, A. V., Protti, M., & Yao, D. (2017). Large and primarily updip afterslip following the 2012 M_W 7.6 Nicoya, Costa Rica, earthquake. *Journal of Geophysical Research: Solid Earth*, *122*(7), 5712–5728. https://doi.org/10.1002/2017jb014035

Hsu, Y. J., Simons, M., Avouac, J. P., Galetzka, J., Sieh, K., Chlieh, M., et al. (2006). Frictional afterslip following the 2005 Nias-Simeulue earthquake, Sumatra. *Science*, *312*(5782), 1921–1926. https://doi.org/10.1126/science.1126960

Hüpers, A., Torres, M. E., Owari, S., McNeill, L. C., Dugan, B., Henstock, T. J., et al. (2017). Release of mineral-bound water prior to subduction tied to shallow seismogenic slip off Sumatra. *Science*, *356*(6340), 841–844. https://doi.org/10.1126/science.aal3429

Ihmlé, P. F., Gomez, J. M., Heinrich, P., & Guibourg, S. (1998). The 1996 Peru tsunamigenic earthquake: Broadband source process. *Geophysical Research Letters*, *25*(14), 2691–2694. https://doi.org/10.1029/98gl01987

Ikari, M. J., Kopf, A. J., Hüpers, A., & Vogt, C. (2018). Lithologic control of frictional strength variations in subduction zone sediment inputs. *Geosphere*, *14*(2), 604–625. https://doi.org/10.1130/ges01546.1

Institut de physique du globe de Paris (IPGP) and École et Observatoire des Sciences de la Terre de Strasbourg (EOST). (1982). *GEOSCOPE, French Global Network of broad band seismic stations*. Institut de physique du globe de Paris (IPGP), Université de Paris. https://doi.org/10.18715/GEOSCOPE.G

Jenkyns, H. C. (1986). Pelagic environments. In H. G. Reading (Ed.), *Sedimentary environments and facies* (2nd ed. pp. 343–397). Blackwell Scientific Publications.

Jia, Z., Zhan, Z., & Kanamori, H. (2022). The 2021 South Sandwich Island M_W 8.2 earthquake: A slow event sandwiched between regular ruptures. *Geophysical Research Letters*, *49*(3), e2021GL097140. https://doi.org/10.1029/2021gl097104

Kameda, J., Shimizu, M., Ujiie, K., Hirose, T., Ikari, M., Mori, J., et al. (2015). Pelagic smectite as an important factor in tsunamigenic slip along the Japan Trench. *Geology*, *43*(2), 155–158. https://doi.org/10.1130/g35948.1

Kanamori, H. (1972). Mechanism of tsunami earthquakes. *Physics of the Earth and Planetary Interiors*, *6*(5), 346–359. https://doi.org/10.1016/0031-9201(72)90058-1

Kanamori, H. (2014). The diversity of large earthquakes and its implications for hazard mitigation. *Annual Review of Earth and Planetary Sciences*, *42*(1), 7–26. https://doi.org/10.1146/annurev-earth-060313-055034

Kanamori, H., & Given, J. W. (1981). Use of long-period surface waves for rapid determination of earthquake-source parameters. *Physics of the Earth and Planetary Interiors*, *27*(1), 8–31. https://doi.org/10.1016/0031-9201(81)90083-2

Kanamori, H., & Kikuchi, M. (1993). The 1992 Nicaragua earthquake: A slow tsunami earthquake associated with subducted sediments. *Nature*, *361*(6414), 714–716. https://doi.org/10.1038/361714a0

Kanamori, H., & Rivera, L. (2008). Source inversion of W phase: Speeding up seismic tsunami warning. *Geophysical Journal International*, *175*(1), 222–238. https://doi.org/10.1111/j.1365-246x.2008.03887.x

Kanamori, H., Rivera, L., & Lee, W. H. (2010). Historical seismograms for unravelling a mysterious earthquake: The 1907 Sumatra Earthquake. *Geophysical Journal International*, *183*(1), 358–374. https://doi.org/10.1111/j.1365-246x.2010.04731.x

Kanamori, H., & Stewart, G. S. (1976). Mode of the strain release along the Gibbs fracture zone, Mid-Atlantic Ridge. *Physics of the Earth and Planetary Interiors*, *11*(4), 312–332. https://doi.org/10.1016/0031-9201(76)90018-2

Kikuchi, M., & Kanamori, H. (1991). Inversion of complex body waves—III. *Bulletin of the Seismological Society of America*, *81*(6), 2335–2350. https://doi.org/10.1785/bssa0810062335

Konca, A. O., Avouac, J. P., Sladen, A., Meltzner, A. J., Sieh, K., Fang, P., et al. (2008). Partial rupture of a locked patch of the Sumatra megathrust during the 2007 earthquake sequence. *Nature*, *456*(7222), 631–635. https://doi.org/10.1038/nature07572

Kövesligethy Radó Seismological Observatory (Geodetic And Geophysical Institute, Research Centre For Astronomy And Earth Sciences, Hungarian Academy Of Sciences (MTA CSFK GGI KRSZO)). (1992). Hungarian National Seismological Network [Dataset]. GFZ Data Services. https://doi.org/10.14470/UH028726

Laske, G., Masters, G., Ma, Z., & Pasyanos, M. (2013). Update on CRUST1. 0—A 1-degree global model of Earth's crust. In *Geophysical research abstracts* (Vol. 15(15), p. 2658). EGU General Assembly 2013.

Lay, T., Ammon, C. J., Kanamori, H., Yamazaki, Y., Cheung, K. F., & Hutko, A. R. (2011). The 25 October 2010 Mentawai tsunami earthquake (M_W 7.8) and the tsunami hazard presented by shallow megathrust ruptures. *Geophysical Research Letters*, *38*(6), L13301. https://doi.org/10.1029/2010gl046552

Lay, T., & Bilek, S. (2007). Anomalous earthquake ruptures at shallow depths on subduction zone megathrusts. In *The seismogenic zone of subduction thrust faults* (pp. 476–511). Columbia University Press.

Lay, T., Kanamori, H., Ammon, C. J., Koper, K. D., Hutko, A. R., Ye, L., et al. (2012). Depth-varying rupture properties of subduction zone megathrust faults. *Journal of Geophysical Research: Solid Earth*, *117*(B4), B04311. https://doi.org/10.1029/2011jb009133

Lay, T., Kanamori, H., Ammon, C. J., Nettles, M., Ward, S. N., Aster, R. C., et al. (2005). The great Sumatra-Andaman earthquake of 26 December 2004. *Science*, *308*(5725), 1127–1133. https://doi.org/10.1126/science.1112250

Li, L., Lay, T., Cheung, K. F., & Ye, L. (2016). Joint modeling of teleseismic and tsunami wave observations to constrain the 16 September 2015 Illapel, Chile, M_W 8.3 earthquake rupture process. *Geophysical Research Letters*, *43*(9), 4303–4312. https://doi.org/10.1002/2016gl068674

Li, X., Huang, Y., Chen, Z., & Huang, X. (2023). Effects of the accretionary wedge and sedimentary layers on subduction zone earthquake ruptures and ground motion: 2-D numerical simulations. *Geophysical Journal International*, *232*(3), 2049–2069. https://doi.org/10.1093/gji/ggac429

Lindsey, E. O., Mallick, R., Hubbard, J. A., Bradley, K. E., Almeida, R. V., Moore, J. D., et al. (2021). Slip rate deficit and earthquake potential on shallow megathrusts. *Nature Geoscience*, *14*(5), 321–326. https://doi.org/10.1038/s41561-021-00736-x

Liu, C., Bai, Y., Lay, T., Feng, Y., & Xiong, X. (2023). Megathrust complexity and the up-dip extent of slip during the 2021 Chignik, Alaska Peninsula earthquake. *Tectonophysics*, *854*, 229808. https://doi.org/10.1016/j.tecto.2023.229808

Ma, S. (2012). A self-consistent mechanisms for slow dynamic deformation and tsunami generation for earthquakes in the shallow subduction zone. *Geophysical Research Letters*, *39*(11), L11310. https://doi.org/10.1029/2012gl051854

Martin, S. S., Li, L., Okal, E. A., Morin, J., Tetteroo, A. E., Switzer, A. D., & Sieh, K. E. (2019). Reassessment of the 1907 Sumatra "tsunami earthquake" based on macroseismic, seismological, and tsunami observations, and modeling. *Pure and Applied Geophysics*, *176*(7), 2831–2868. https://doi.org/10.1007/s00024-019-02134-2

McKenzie, D., & Jackson, J. (2012). Tsunami earthquake generation by the release of gravitational potential energy. *Earth and Planetary Science Letters*, *345*, 1–8. https://doi.org/10.1016/j.epsl.2012.06.036

MedNet Project Partner Institutions. (1990). Mediterranean Very Broadband Seismographic Network (MedNet) [Dataset]. Istituto Nazionale di Geofisica e Vulcanologia (INGV). https://doi.org/10.13127/sd/fbbbtdtd6q

Moore, J. C., Plank, T. A., Chester, F. M., Polissar, P. J., & Savage, H. M. (2015). Sediment provenance and controls on slip propagation: Lessons learned from the 2011 Tohoku and other great earthquakes of the subducting northwest Pacific plate. *Geosphere*, *11*(3), 533–541. https://doi.org/10.1130/ges01099.1

Moore, J. C., & Saffer, D. (2001). Updip limit of the seismogenic zone beneath the accretionary prism of southwest Japan: An effect of diagenetic to low-grade metamorphic processes and increasing effective stress. *Geology*, *29*(2), 183–186. https://doi.org/10.1130/0091-7613(2001)029<0183:ulotsz>2.0.co;2

Natawidjaja, D. H., Sieh, K., Chlieh, M., Galetzka, J., Suwargadi, B. W., Cheng, H., et al. (2006). Source parameters of the great Sumatran megathrust earthquakes of 1797 and 1833 inferred from coral microatolls. *Journal of Geophysical Research: Solid Earth*, *111*(B6). https://doi.org/10.1029/2005jb004025

Noda, A. (2016). Forearc basins: Types, geometries, and relationships to subduction zone dynamics. *GSA Bulletin*, *128*(5–6), 879–895. https://doi.org/10.1130/b31345.1

Okal, E. A., & Newman, A. V. (2001). Tsunami earthquakes: The quest for a regional signal. *Physics of the Earth and Planetary Interiors*, *124*(1–2), 45–70. https://doi.org/10.1016/s0031-9201(01)00187-x

Oryan, B., & Buck, W. R. (2020). Larger tsunamis from megathrust earthquakes where slab dip is reduced. *Nature Geoscience*, *13*(4), 319–324. https://doi.org/10.1038/s41561-020-0553-x

Ozawa, S., Nishimura, T., Suito, H., Kobayashi, T., Tobita, M., & Imakiire, T. (2011). Coseismic and postseismic slip of the 2011 magnitude-9 Tohoku-Oki earthquake. *Nature*, *475*(7356), 373–376. https://doi.org/10.1038/nature10227

Pelayo, A. M., & Wiens, D. A. (1992). Tsunami earthquakes: Slow thrust-faulting events in the accretionary wedge. *Journal of Geophysical Research: Solid Earth*, *97*(B11), 15321–15337. https://doi.org/10.1029/92jb01305

Pérez, O. J. (2000). Kuril Islands Arc: Two seismic cycles of great earthquakes during which the complete history of seismicity ($M_S \geq 6$) is observed. *Bulletin of the Seismological Society of America*, *90*(4), 1096–1100. https://doi.org/10.1785/0119990063

Philibosian, B., Sieh, K., Avouac, J. P., Natawidjaja, D. H., Chiang, H. W., Wu, C. C., et al. (2017). Earthquake supercycles on the Mentawai segment of the Sunda megathrust in the seventeenth century and earlier. *Journal of Geophysical Research: Solid Earth*, *122*(1), 642–676. https://doi.org/10.1002/2016jb013560

Polet, J., & Kanamori, H. (2000). Shallow subduction zone earthquakes and their tsunamigenic potential. *Geophysical Journal International*, *142*(3), 684–702. https://doi.org/10.1046/j.1365-246x.2000.00205.x

Prada, M., Galvez, P., Ampuero, J. P., Sallarès, V., Sánchez-Linares, C., Macías, J., & Peter, D. (2021). The influence of depth-varying elastic properties of the upper plate on megathrust earthquake rupture dynamics and tsunamigenesis. *Journal of Geophysical Research: Solid Earth*, *126*(11), e2021JB022328. https://doi.org/10.1029/2021jb022328

Pytte, A. M., & Reynolds, R. C. (1989). The thermal transformation of smectite to illite. In *Thermal history of sedimentary basins: Methods and case histories* (pp. 133–140). Springer New York.

Qiu, A., & Barbot, S. (2022). Tsunami excitation in the outer wedge of global subduction zones. *Earth-Science Reviews*, *230*, 104054. https://doi.org/10.1016/j.earscirev.2022.104054

Ruff, L., & Kanamori, H. (1980). Seismicity and the subduction process. *Physics of the Earth and Planetary Interiors*, *23*(3), 240–252. https://doi.org/10.1016/0031-9201(80)90117-x

Saffer, D. M., Underwood, M. B., & McKiernan, A. W. (2008). Evaluation of factors controlling smectite transformation and fluid production in subduction zones: Application to the Nankai Trough. *Island Arc*, *17*(2), 208–230. https://doi.org/10.1111/j.1440-1738.2008.00614.x

Sallarès, V., Prada, M., Riquelme, S., Meléndez, A., Calahorrano, A., Grevemeyer, I., & Ranero, C. R. (2021). Large slip, long duration, and moderate shaking of the Nicaragua 1992 tsunami earthquake caused by low near-trench rock rigidity. *Science Advances*, *7*(32), eabg8659. https://doi.org/10.1126/sciadv.abg8659

Sallarès, V., & Ranero, C. R. (2019). Upper-plate rigidity determines depth-varying rupture behavior of megathrust earthquakes. *Nature*, *576*(7785), 96–101. https://doi.org/10.1038/s41586-019-1784-0

Satake, K., Nishimura, Y., Putra, P. S., Gusman, A. R., Sunendar, H., Fujii, Y., et al. (2013). Tsunami source of the 2010 Mentawai, Indonesia earthquake inferred from tsunami field survey and waveform modeling. *Pure and Applied Geophysics*, *170*(9–10), 1567–1582. https://doi.org/10.1007/s00024-012-0536-y

Scholz, C. H. (1998). Earthquakes and friction laws. *Nature*, *391*(6662), 37–42. https://doi.org/10.1038/34097

Scholz, C. H., & Campos, J. (1995). On the mechanism of seismic decoupling and back arc spreading at subduction zones. *Journal of Geophysical Research: Solid Earth*, *100*(B11), 22103–22115. https://doi.org/10.1029/95jb01869

Scholz, C. H., & Campos, J. (2012). The seismic coupling of subduction zones revisited. *Journal of Geophysical Research: Solid Earth*, *117*(B5). https://doi.org/10.1029/2011jb009003

Scripps Institution of Oceanography (SIO). (1986). Global Seismograph network - IRIS/IDA [Dataset], International Federation of Digital Seismograph Networks. https://doi.org/10.7914/SN/II

Sladen, A., & Trevisan, J. (2018). Shallow megathrust earthquake ruptures betrayed by their outer-trench aftershocks signature. *Earth and Planetary Science Letters*, *483*, 105–113. https://doi.org/10.1016/j.epsl.2017.12.006

Sodankylä Geophysical Observatory / University Of Oulu (Finland). (1980). Northern Finland Seismological Network [Dataset]. GFZ Data Services. https://doi.org/10.14470/SA879454

Spinelli, G. A., & Underwood, M. B. (2004). Character of sediments entering the Costa Rica subduction zone: Implications for partitioning of water along the plate interface. *Island Arc*, *13*(3), 432–451. https://doi.org/10.1111/j.1440-1738.2004.00436.x

Sriyanto, S. P. D., Arimuko, A., Nurokhim, A., Gunawan, I., Fatchurochman, I., Samapta, B. T., & Putra, A. A. (2023). Source Characteristics of the 18 November 2022 Earthquake (MW 6.7), Offshore Southwest Sumatra, Indonesia, Revealed by Tsunami Waveform Analysis: Implications for Tsunami Hazard Assessment. *Pure and Applied Geophysics*, *180*(11), 3655–3670. https://doi.org/10.1007/s00024-023-03371-2

Stevens, D. E., Henstock, T. J., & McNeill, L. C. (2021). Evolution of the thermal and dehydration state of sediments entering the North Sumatra subduction zone. *Geochemistry, Geophysics, Geosystems*, *22*(4), e2020GC009306. https://doi.org/10.1029/2020gc009306

Tanioka, Y., Ruff, L., & Satake, K. (1997). What controls the lateral variation of large earthquake occurrence along the Japan Trench? *Island Arc*, *6*(3), 261–266. https://doi.org/10.1111/j.1440-1738.1997.tb00176.x

Tanioka, Y., & Satake, K. (1996). Fault parameters of the 1896 Sanriku tsunami earthquake estimated from tsunami numerical modeling. *Geophysical Research Letters*, *23*(13), 1549–1552.

Tsang, L. L., Hill, E. M., Barbot, S., Qiu, Q., Feng, L., Hermawan, I., et al. (2016). Afterslip following the 2007 M_W 8.4 Bengkulu earthquake in Sumatra loaded the 2010 M_W 7.8 Mentawai tsunami earthquake rupture zone. *Journal of Geophysical Research: Solid Earth*, *121*(12), 9034–9049. https://doi.org/10.1002/2016jb013432

Ujiie, K., Tanaka, H., Saito, T., Tsutsumi, A., Mori, J. J., Kameda, J., & Expedition 343 and 343T Scientists. (2013). Low coseismic shear stress on the Tohoku-Oki megathrust determined from laboratory experiments. *Science*, *342*(6163), 1211–1214. https://doi.org/10.1126/science.1243485

Villegas-Lanza, J. C., Chlieh, M., Cavalié, O., Tavera, H., Baby, P., Chire-Chira, J., & Nocquet, J. M. (2016). Active tectonics of Peru: Heterogeneous interseismic coupling along the Nazca megathrust, rigid motion of the Peruvian Sliver, and Subandean shortening accommodation. *Journal of Geophysical Research: Solid Earth*, *121*(10), 7371–7394. https://doi.org/10.1002/2016jb013080

Vrolijk, P. (1990). On the mechanical role of smectite in subduction zones. *Geology*, *18*(8), 703–707. https://doi.org/10.1130/0091-7613(1990)018<0703:otmros>2.3.co;2

Whittaker, J. M., Goncharov, A., Williams, S. E., Müller, R. D., & Leitchenkov, G. (2013). Global sediment thickness data set updated for the Australian-Antarctic Southern Ocean. *Geochemistry, Geophysics, Geosystems*, *14*(8), 3297–3305. https://doi.org/10.1002/ggge.20181

Xiao, Z., Freymueller, J. T., Grapenthin, R., Elliott, J. L., Drooff, C., & Fusso, L. (2021). The deep Shumagin gap filled: Kinematic rupture model and slip budget analysis of the 2020 M_W 7.8 Simeonof earthquake constrained by GNSS, global seismic waveforms, and floating InSAR. *Earth and Planetary Science Letters*, *576*, 117241. https://doi.org/10.1016/j.epsl.2021.117241

Yamazaki, Y., Cheung, K. F., & Kowalik, Z. (2011). Depth-integrated, non-hydrostatic model with grid nesting for tsunami generation, propagation, and run-up. *International Journal for Numerical Methods in Fluids*, *67*(12), 2081–2107. https://doi.org/10.1002/fld.2485

Yamazaki, Y., Cheung, K. F., & Lay, T. (2013). Modeling of the 2011 Tohoku near-field tsunami from finite-fault inversion of seismic waves. *Bulletin of the Seismological Society of America*, *103*(2B), 1444–1455. https://doi.org/10.1785/0120120103

Yamazaki, Y., Cheung, K. F., & Lay, T. (2018). A self-consistent fault slip model for the 2011 Tohoku earthquake and tsunami. *Journal of Geophysical Research: Solid Earth*, *123*(2), 1435–1458. https://doi.org/10.1002/2017jb014749

Yamazaki, Y., Lay, T., Cheung, K. F., Witter, R. C., La Selle, S. P. M., & Jaffe, B. E. (2024). A great tsunami earthquake component of the 1957 Aleutian Islands earthquake. *Earth and Planetary Science Letters*, *637*, 118691. https://doi.org/10.1016/j.epsl.2024.118691

Ye, L., Bai, Y., Si, D., Lay, T., Cheung, K. F., & Kanamori, H. (2022). Rupture model for the 29 July 2021 M_W 8.2 Chignik, Alaska earthquake constrained by seismic, geodetic, and tsunami observations. *Journal of Geophysical Research: Solid Earth*, *127*(7), e2021JB023676. https://doi.org/10.1029/2021jb023676

Ye, L., Kanamori, H., Avouac, J. P., Li, L., Cheung, K. F., & Lay, T. (2016b). The 16 April 2016, M_W 7.8 (M_S 7.5) Ecuador earthquake: A quasi-repeat of the 1942 M_S 7.5 earthquake and partial re-rupture of the 1906 M_S 8.6 Colombia–Ecuador earthquake. *Earth and Planetary Science Letters*, *454*, 248–258. https://doi.org/10.1016/j.epsl.2016.09.006

Ye, L., Lay, T., & Kanamori, H. (2011). The Sanriku-Oki low seismicity region on the northern margin of the great 2011 Tohoku earthquake rupture. *Journal of Geophysical Research: Solid Earth*, *117*, B02305. https://doi.org/10.1029/2011JB008847

Ye, L., Lay, T., & Kanamori, H. (2013). Large earthquake rupture process variations on the Middle America megathrust. *Earth and Planetary Science Letters*, *381*, 147–155. https://doi.org/10.1016/j.epsl.2013.08.042

Ye, L., Lay, T., Kanamori, H., & Rivera, L. (2016a). Rupture characteristics of major and great ($M_W \geq 7.0$) megathrust earthquakes from 1990 to 2015: 2. Depth dependence. *Journal of Geophysical Research: Solid Earth*, *121*(2), 845–863. https://doi.org/10.1002/2015jb012427

Ye, L., Lay, T., Kanamori, H., & Rivera, L. (2016c). Rupture characteristics of major and great ($M_W \geq 7.0$) megathrust earthquakes from 1990 to 2015: 1. Source parameter scaling relationships. *Journal of Geophysical Research: Solid Earth*, *121*(2), 826–844. https://doi.org/10.1002/2015jb012426

Ye, L., Lay, T., Kanamori, H., Yamazaki, Y., & Cheung, K. F. (2021). The 22 July 2020 M_W 7.8 Shumagin seismic gap earthquake: Partial rupture of a weakly coupled megathrust. *Earth and Planetary Science Letters*, *562*, 116879. https://doi.org/10.1016/j.epsl.2021.116879

Yue, H., Lay, T., Rivera, L., An, C., Vigny, C., Tong, X., & Soto, J. C. B. (2014). Localized fault slip to the trench in the 2010 Maule, Chile M_W = 8.8 earthquake from joint inversion of high-rate GPS, teleseismic body waves, InSAR, campaign GPS, and tsunami observations. *Journal of Geophysical Research: Solid Earth*, *119*(10), 7786–7804. https://doi.org/10.1002/2014jb011340

Yue, H., Lay, T., Rivera, L., Bai, Y., Yamazaki, Y., Cheung, K. F., et al. (2014). Rupture process of the 2010 M_W 7.8 Mentawai tsunami earthquake from joint inversion of near-field hr-GPS and teleseismic body wave recordings constrained by tsunami observations. *Journal of Geophysical Research: Solid Earth*, *119*(7), 5574–5593. https://doi.org/10.1002/2014jb011082

Yue, H., Lay, T., Schwartz, S. Y., Rivera, L., Protti, M., Dixon, T. H., et al. (2013). The 5 September 2012 Nicoya, Costa Rica M_W 7.6 earthquake rupture process from joint inversion of high-rate GPS, strong-motion, and teleseismic P wave data and its relationship to adjacent plate boundary interface properties. *Journal of Geophysical Research: Solid Earth*, *118*(10), 5453–5466. https://doi.org/10.1002/jgrb.50379

Supporting Information for

The 2022 M_W 7.3 Southern Sumatra Tsunami Earthquake: Rupture Up-dip of the 2007 M_W 8.4 Bengkulu Event

Tao Xia[1], Lingling Ye[1,] *, Yefei Bai[2], Thorne Lay[3], Shiqing Xu[1], Hiroo Kanamori[4], Luis Rivera[5], Sesar Prabu Dwi Sriyanto[6]

[1]*Department of Earth and Space Sciences, Southern University of Science and Technology, Shenzhen, China*
[2]*Ocean College, Zhejiang University, Zhoushan, Zhejiang, China.*
[3]*Department of Earth and Planetary Sciences, University of California Santa Cruz, Santa Cruz, CA 95064, USA*
[4]*Seismological Laboratory, California Institute of Technology, Pasadena, CA 91125, USA*
[5]*Institut Terre et Environnement Strasbourg, Université de Strasbourg/CNRS, Strasbourg, France*
[6]*Badan Meteorologi, Klimatologi, dan Geofisika (BMKG), Jakarta, Indonesia*

* Corresponding to: Lingling Ye, yell@sustech.eud.cn.

Contents of this file

Table S1. Point-source solutions

	Lon.	Lat.	H (km)	Strike	Dip	Rake	M_0 (Nm)	M_W
USGS	100.74°	-4.96°	19.5	347.0°	6.0°	125.0°	3.29 x10^{19}	6.94
GCMT	100.31°	-4.98°	12.0	335.0°	11.0°	100.0°	2.81 x10^{19}	6.90
This study (W-Phase)	100.30°	-4.99°	9.5	346.6°	6.2°	114.4°	4.39 x10^{19}	7.03

Table S2. Parameters for slip models M01-M04

Models	$\overline{\mu}$ (GPa)	$\bar{\delta}$	D_{peak} (m)	$\overline{D}_{0.15}$ (m)	$A_{0.15}$ (km^2)	$\varphi_{0.15}$ (km^3)	φ (km^3)	M_0 (Nm)	β_2	Data fits	
										Teleseismic	Tsunami
M01	50.0	3.8°	3.5	1.4	1088	1.5	2.0	8.07 x10^{19}	0.05	Poor	Poor
M02	27.3	3.7°	4.7	1.7	1152	2.0	2.5	5.52 x10^{19}	0.05	Poor	Poor
M03	47.8	3.5°	4.4	1.8	1920	3.5	5.0	19.40 x10^{19}	0.001	Good	Good
M04	23.0	3.5°	4.1	1.8	2240	4.0	5.6	10.50 x10^{19}	0.001	Good	Good

Notes: $\overline{\mu}$ and $\bar{\delta}$ are average rigidity and dip angle weighted by the slip distribution $D(x,y)$ [$\bar{\mu} = \int \mu(x,y)D(x,y)dS / \int D(x,y)dS$; $\bar{\delta} = \int \delta(x,y)D(x,y)dS / \int D(x,y)dS$], respectively. D_{peak} is the peak slip. $\overline{D}_{0.15}$, $A_{0.15}$ and $\varphi_{0.15}$ are average slip, total area and seismic potency for grids which has a slip value larger or equal to $0.15D_{\text{peak}}$, respectively. $\varphi_{0.15} = A_{0.15} \times \overline{D}_{0.15}$. φ is the total seismic potency [$\varphi = \int D(x,y)dS$]. β_2 is the weighting factor of the moment constraint. Model M04 is our preferred model.

Table S3. Different velocity models tested in iterative finite-fault inversion.

Depth (km)	V_P (km/s)			V_S (km/s)			ρ (g/cm^3)	Rigidity μ (GPa)		
	M01/M03	**M02**	**M04**	**M01/M03**	**M02**	**M04**		**M01/M03**	**M02**	**M04**
0.00	1.50			0.00			1.02	0.00		
5.52	1.50			0.00			1.02	0.00		
5.52	1.75			0.34			1.82	0.21		
5.82	1.75			0.34			1.82	0.21		
5.82	5.00	3.95	3.50	2.70	2.13	1.89	2.55	18.59	11.57	9.11
6.49	5.00	3.95	3.50	2.70	2.13	1.89	2.55	18.59	11.57	9.11
6.49	6.50	5.10	4.55	3.70	2.92	2.59	2.85	39.02	24.30	19.12
7.97	6.50	5.10	4.55	3.70	2.92	2.59	2.85	39.02	24.30	19.12
7.97	7.10	5.60	4.97	4.05	3.20	2.84	3.05	50.03	31.23	24.60
12.55	7.10	5.60	4.97	4.05	3.20	2.84	3.05	50.03	31.23	24.60
12.55	7.80			4.40			3.50	67.76		
+∞	7.80			4.40			3.50	67.76		

Model M01/M03: velocity model from the Crust 1.0 model (Laske et al., 2013)

Model M02: velocity model after multiplying V_P, V_S in the Crust 1.0 model by 0.79

Model M04: velocity model after multiplying V_P, V_S in the Crust 1.0 model by 0.70

Table S4. Relocation info. for 7 well-documented tsunami earthquakes since 1990.

Events	USGS-NEIC			The optimal solutions in this study		
	Lat.	Lon.	Depth (km)	Lat.	Lon.	Depth (km)*
1992 M_W 7.7 Nicaragua 1992-09-02T00:16:01	11.742°	-87.340°	44.8	11.602°	-87.305°	19.9
1994 M_W 7.8 Java 1994-06-02T18:17:34	-10.477°	112.835°	18.4	-10.345°	112.928°	11.2
1996 M_W 7.4 Peru 1996-02-21T12:51:01	-9.593°	-79.587°	10.0	-9.678°	-79.897°	16.9
2006 M_W 7.7 Java 2006-07-17T08:19:26	-9.284°	107.419°	20.0	-9.184°	107.569°	14.2
2010 M_W 7.8 Mentawai 2010-10-25T14:42:22	-3.487°	100.082°	20.1	-3.485°	100.184°	12.1
2012 M_W 7.3 El Salvador 2012-08-27T04:37:19	12.139°	-88.590°	28.0	12.299°	-88.604°	19.9
2022 M_W 7.3 Sumatra 2022-11-18T13:37:08	-4.904°	100.786°	25.0	-4.904°	100.736°	8.9
Velocity model: Crust 1.0 and PREM models. *Source depth is obtained by projecting the epicenter to the Slab 2.0 model.						

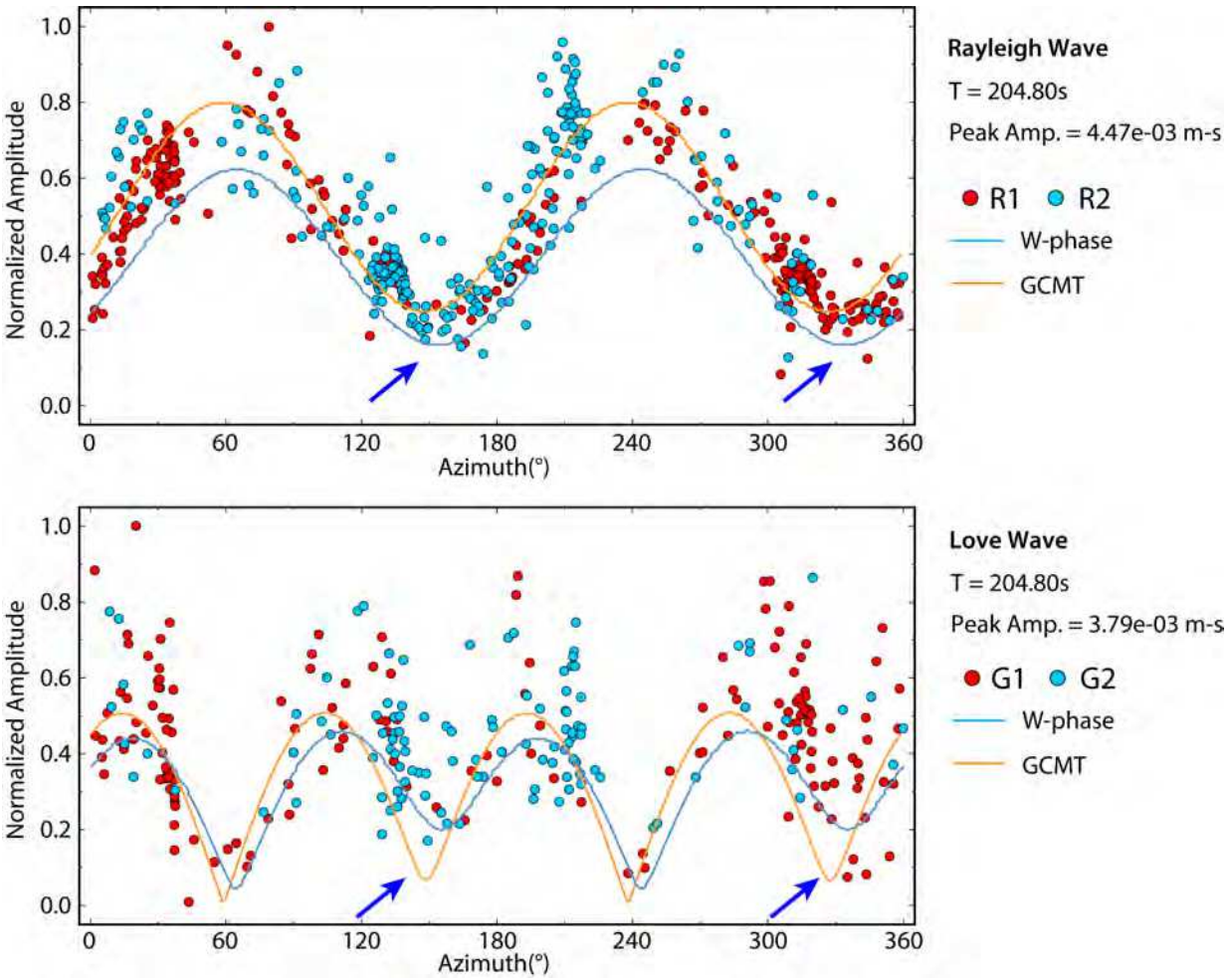

Figure S1. Observed and predicted Rayleigh wave (top) and Love wave (bottom) source spectral amplitudes for period T = 204.80 s for the 18 November 2022 Sumatra earthquake. Red and cyan dots indicate short-arc (R1, G1) and long-arc (R2, G2) observations, respectively. Cyan and orange lines indicate theoretical amplitudes for our *W*-phase solution with strike 346.6°, dip 6.2°, rake 114.4°, $M_0 = 4.39 \times 10^{19}$ Nm and the GCMT solution with strike 335°, dip 11°, rake 100°, $M_0 = 2.81 \times 10^{19}$ Nm, respectively. The blue arrows indicated the symmetry in the Rayleigh wave radiation nodes (e) and the asymmetry in the Love wave radiation nodes (f).

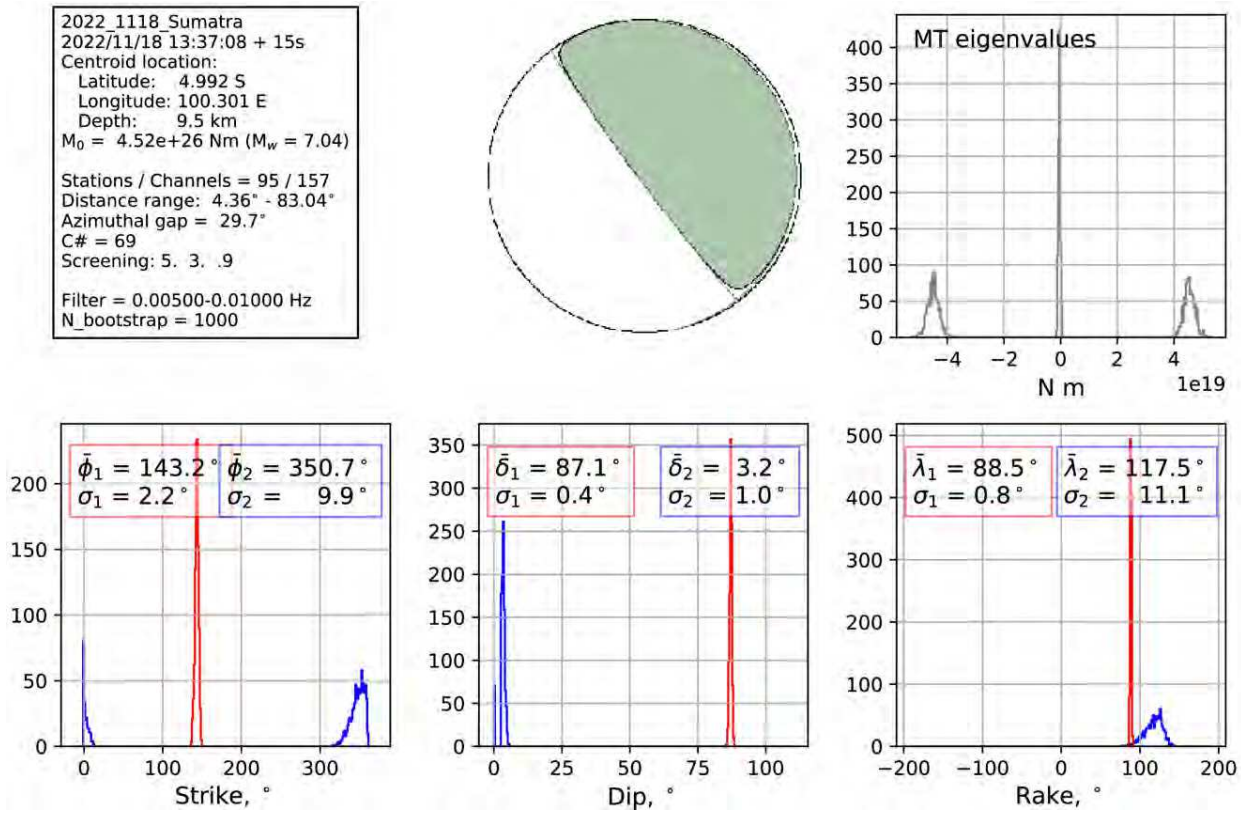

Figure S2. Bootstrap statistics of the *W*-phase solution. The box on the top left and focal mechanism gives the event details and a summary of the *W*-phase source inversion parameters, solution, and quality control parameters. The histograms show the output of 1,000 bootstrap inversion solutions. The initial dataset comprises 157 channels (Nch). Each bootstrap dataset is built by randomly drawing (with replacement) Nch channels from the initial dataset. Histograms for the eigenvalues of the moment tensors are depicted on the top right panel. Although not enforced during the inversion, for practical purposes, all the solutions are pure double couples. The bottom histograms correspond to the geometrical parameters: strike (φ), dip (δ), and rake (λ) of the double couples. Blue and red, respectively, indicate the shallow and the near-vertical planes. They are remarkably stable. For geometrical reasons, the strike and the rake of the sub-horizontal planes are more spread. The average and standard deviation (σ) for each parameter are given. The dip of the shallowly dipping plane averages 3.2° with a standard deviation of 1°.

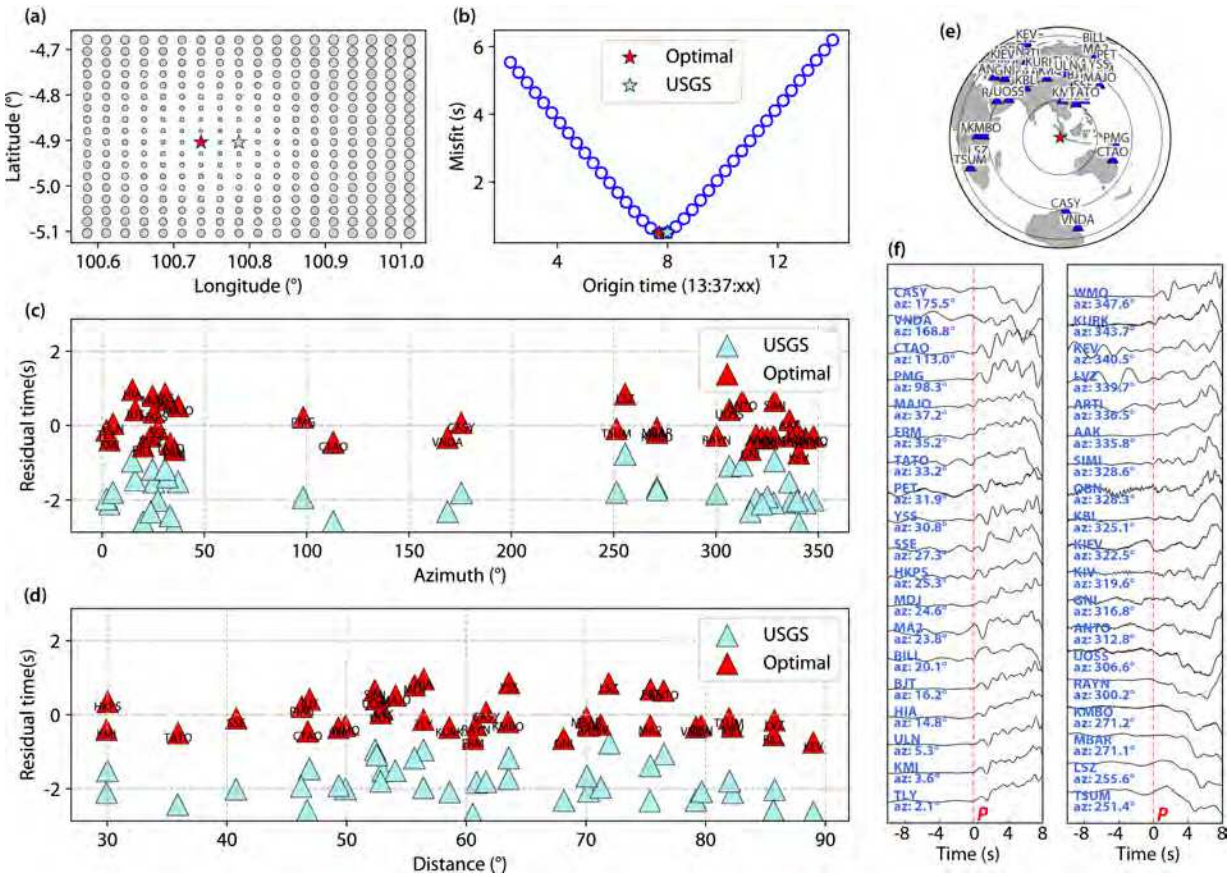

Figure S3. Relocation of the 2022 Sumatra earthquake. The source depth of our optimal solution is fixed at 8.9 km by projecting the corresponding epicenter onto the Slab 2.0 model. (a) and (b) represent misfit between observed and theoretical first arrival in both space and time, respectively. (c) and (d) Plots of arrival time residuals using the USGS-NEIC solution and our optimal location with station azimuth and distance. (e) and (f) Station distribution and initial waveforms of P-wave aligned with the predicted time from our optimal solution.

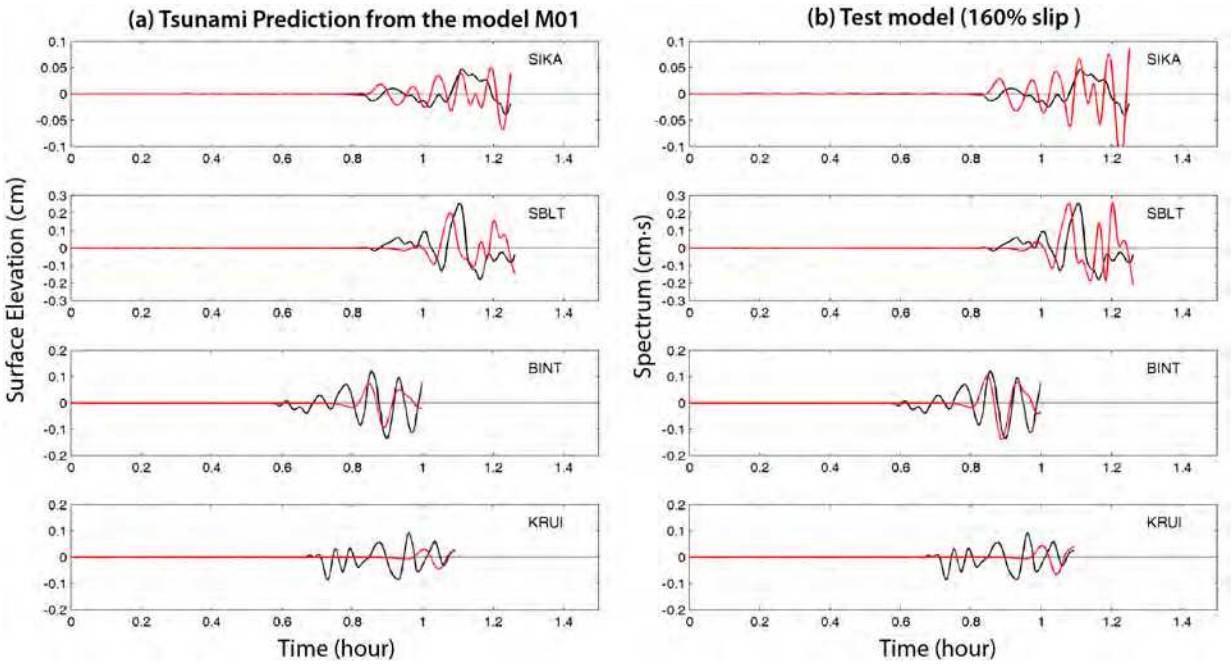

Figure S4. Comparison of recorded (black) and computed (red) sea level time series at SIKA, SBLT, BINT, and KRUI tide gauges for (a) slip model M01 and (b) the Test model that increases slip of all subfaults by a factor of 1.6 relative to M01.

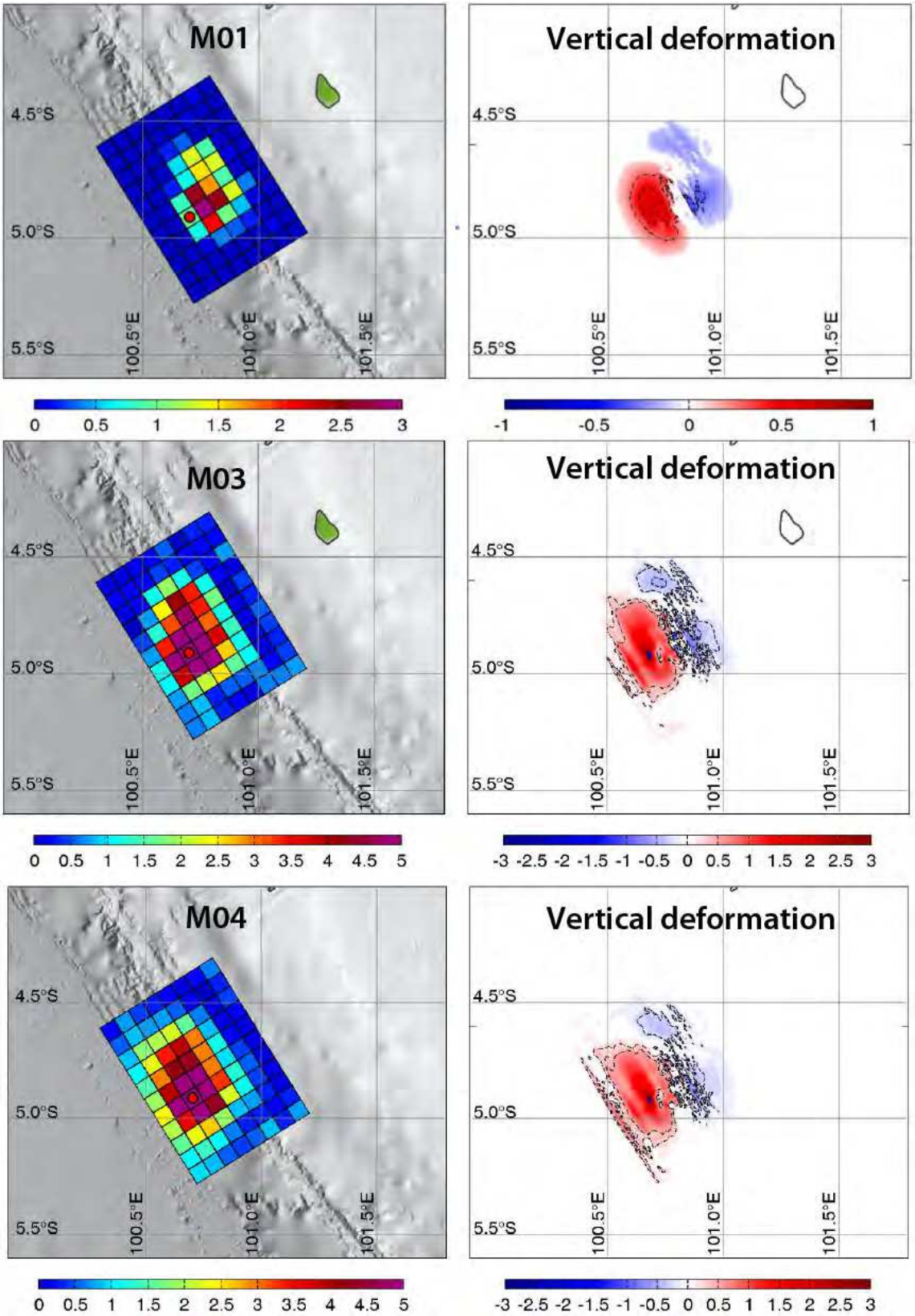

Figure S5. Map and seafloor vertical deformation for slip models M01, M03, and M04. The red dot indicates the epicenter. Model M04 is our preferred solution.

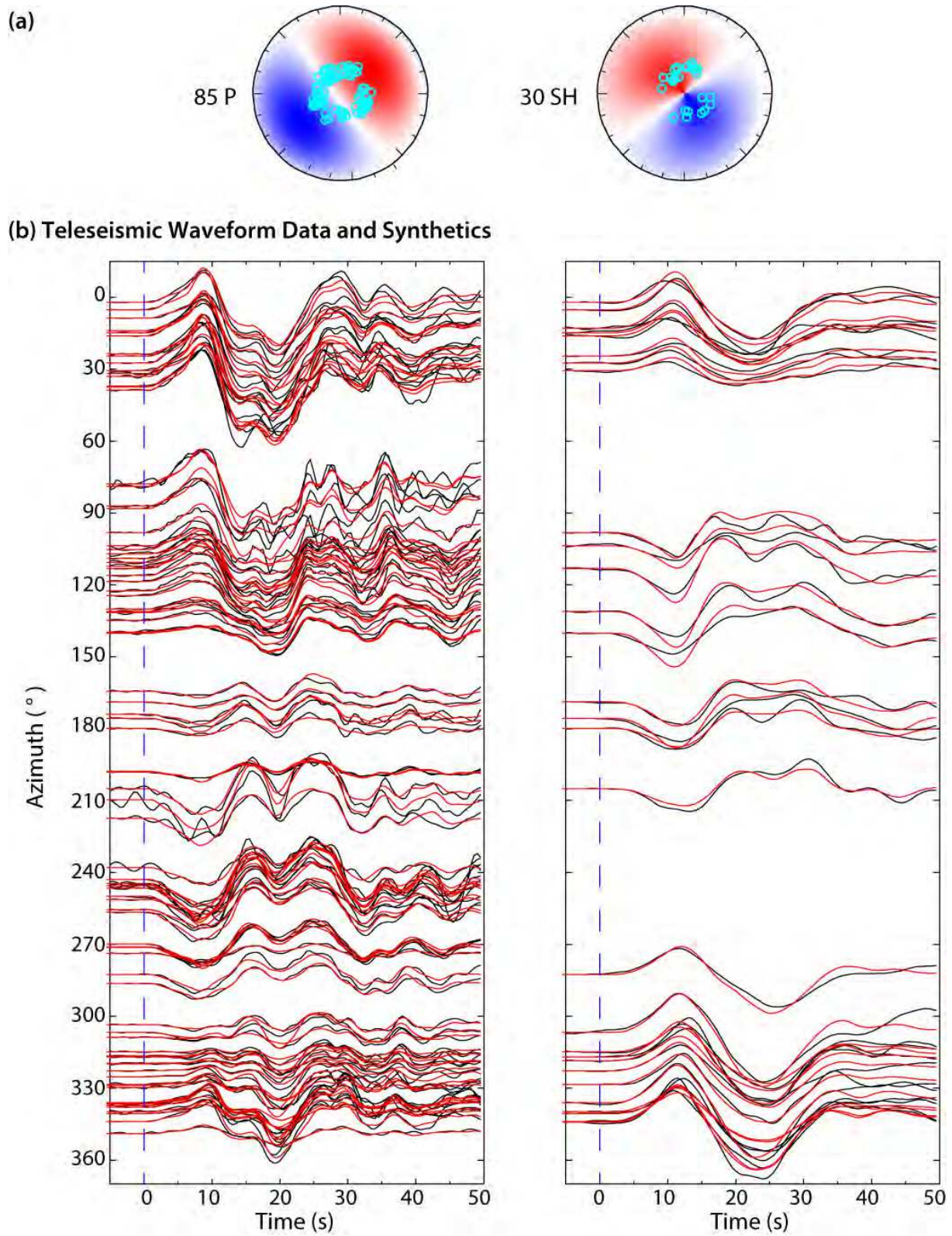

Figure S6. Teleseismic data fits from the preferred slip model M04. (a) Lower-hemisphere stereographic projections of radiation patterns for the 85 *P*-wave and 30 *SH*-wave (cyan) ground motions used in the inversion. (b) Comparisons of the observed (black) and predicted (red) ground displacement waveforms of teleseismic *P* (left) and *SH* (right) waves.

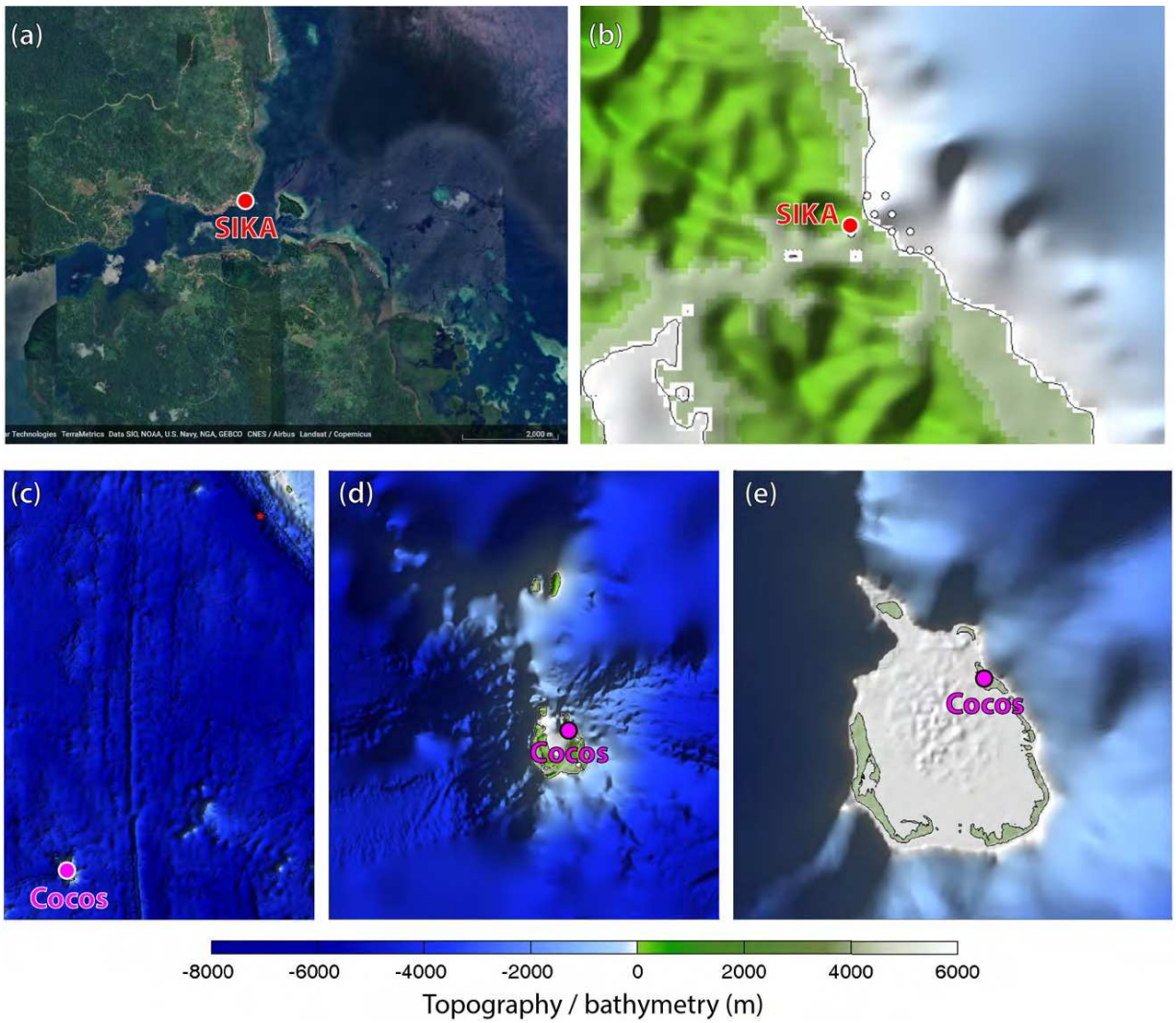

Figure S7. Comparison of computation domains for SIKA and Cocos stations. (a) Observed topography and bathymetry near SIKA Tide Gauge. (b) Computation domain for SIKA Gauge; the water inlet is not accurately represented in the bathymetry model, so virtual station locations (white dots) are used to estimate the response. (c-e) 12-arcsec, 6-arcsec and 1.5-arcsec resolution computation domains for Cocos Island, respectively.

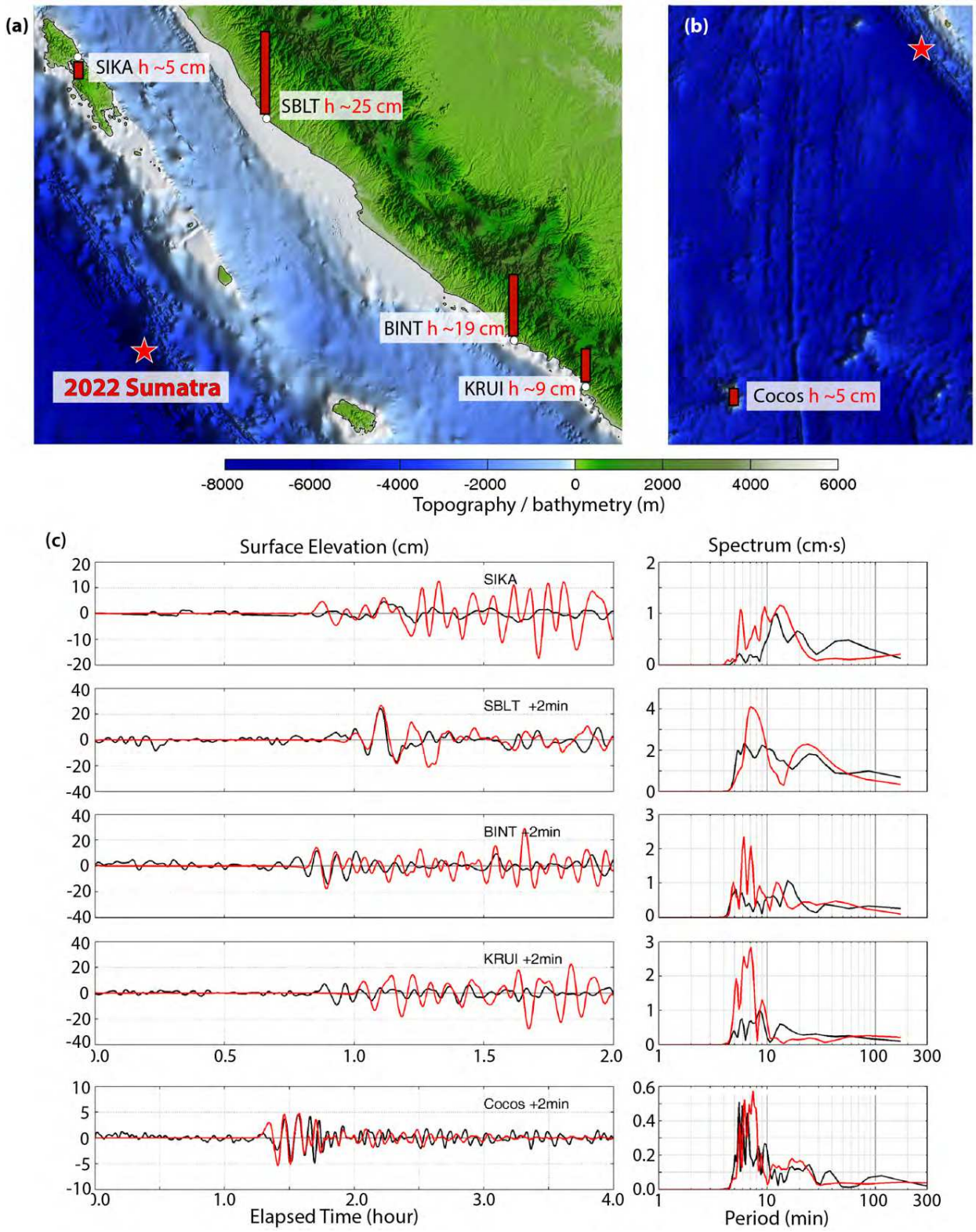

Figure S8. Tsunami simulation bathymetry and results for all five tide gauges from the preferred model (M04). (a-b) Location of the five tide gauges. The red bars represent the tsunami heights observed at each station. (c) Comparison of recorded (black) and computed (red) time series (left) for the preferred slip model and amplitude spectra (right) at each tide gauge.

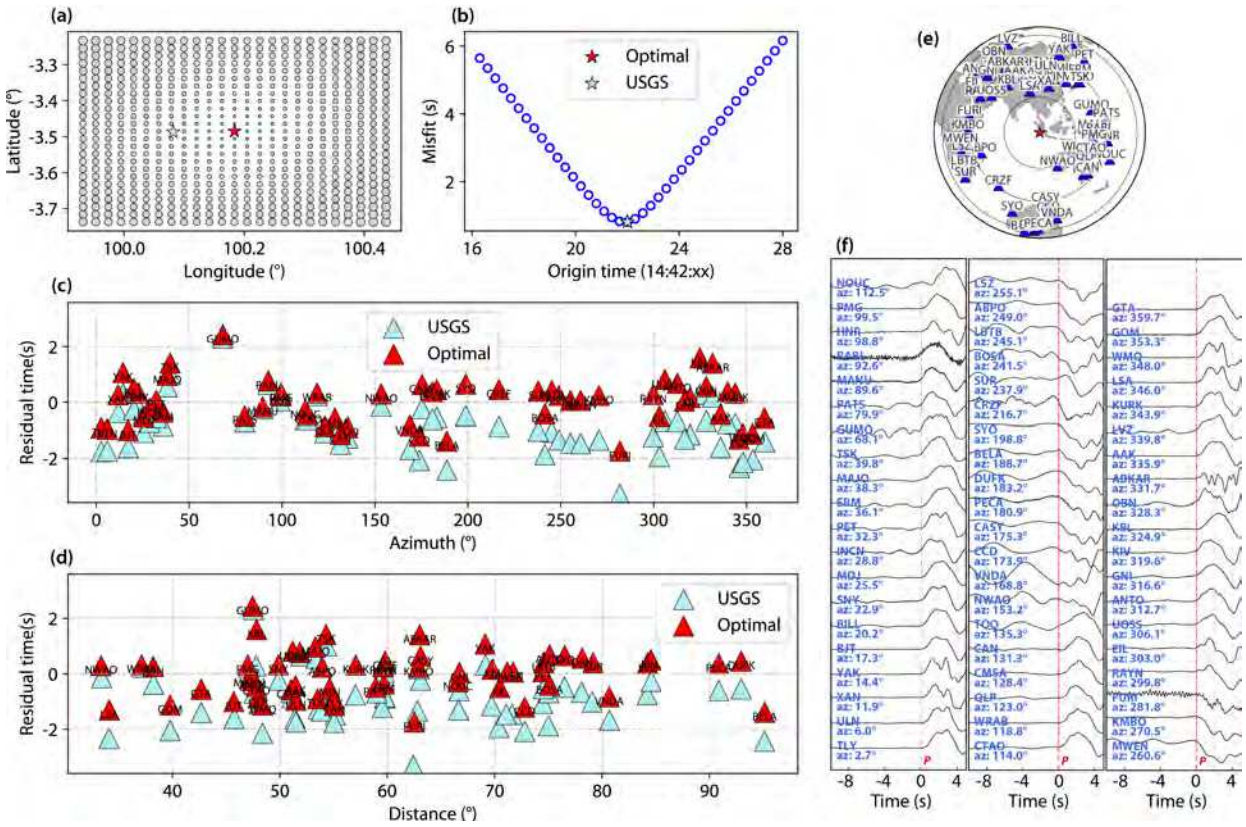

Figure S9. Relocation of the 2010 M_W 7.8 Mentawai earthquake. The depth of our optimal solution is fixed at 12.1 km by projecting the corresponding epicenter onto the Slab 2.0 model. Other symbols are same as Figure S3.

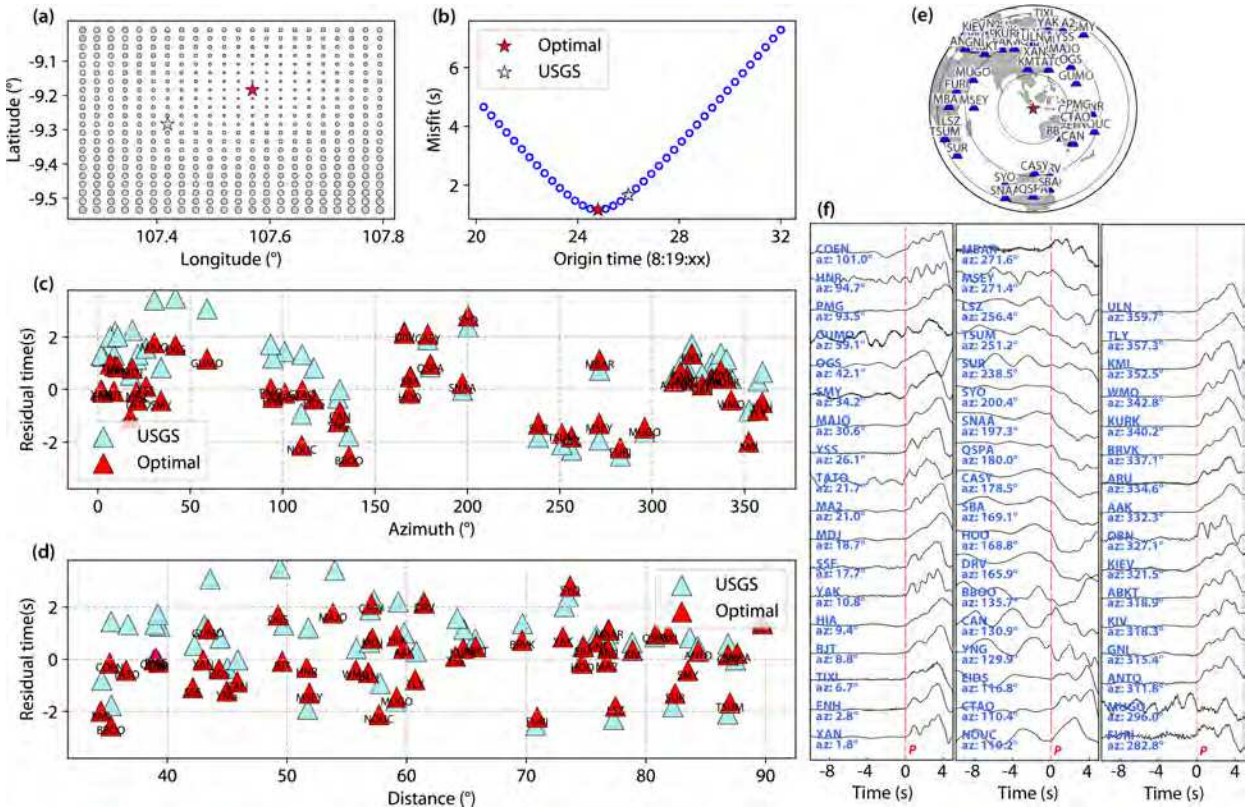

Figure S10. Relocation of the 2006 M_W 7.7 Java earthquake. The depth of our optimal solution is fixed at 12.7 km and 14.2 km by projecting the corresponding epicenter onto the Slab 2.0 model. Other symbols are same as Figure S3.

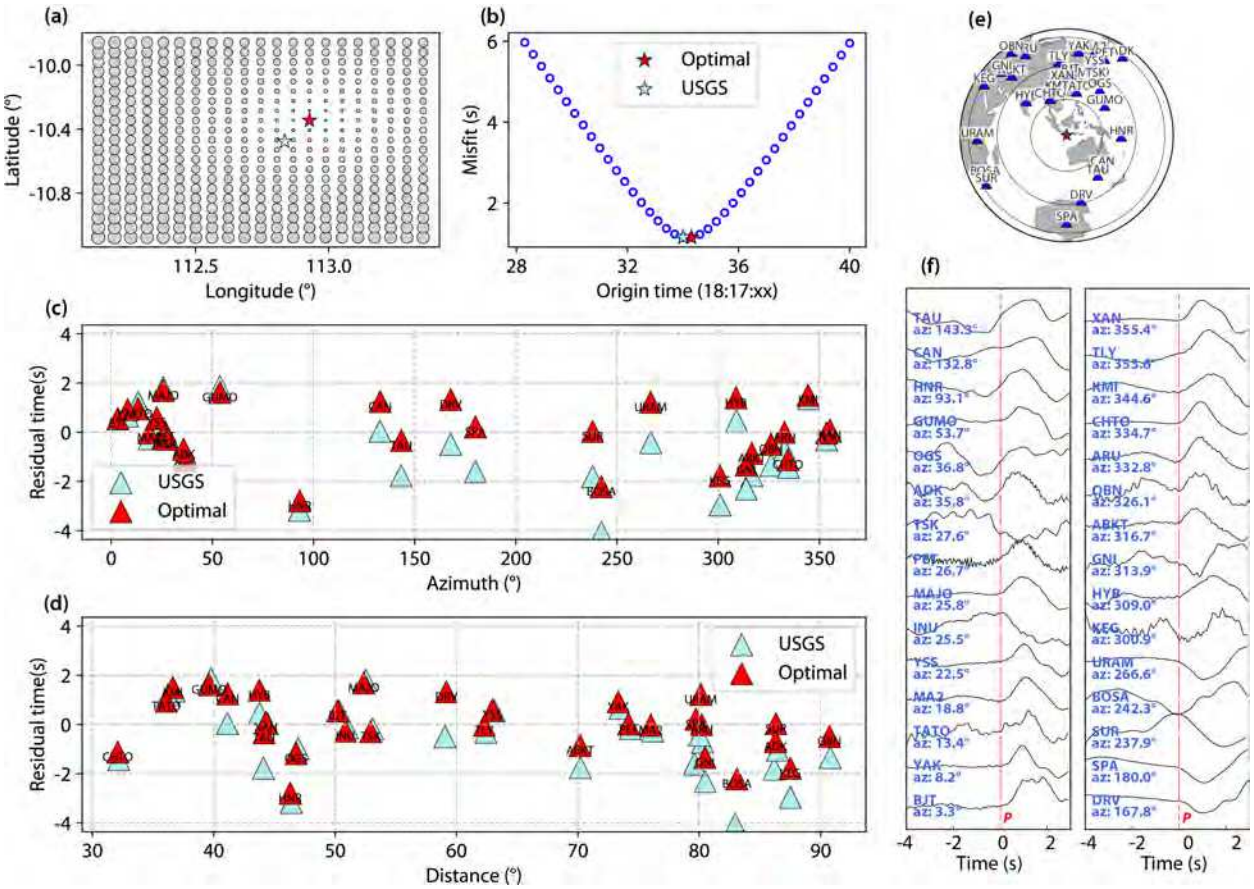

Figure S11. Relocation of the 1994 M_W 7.8 Java earthquake. The depth of our optimal solution is fixed at 11.2 km by projecting the corresponding epicenter onto the Slab 2.0 model. Other symbols are same as Figure S3.

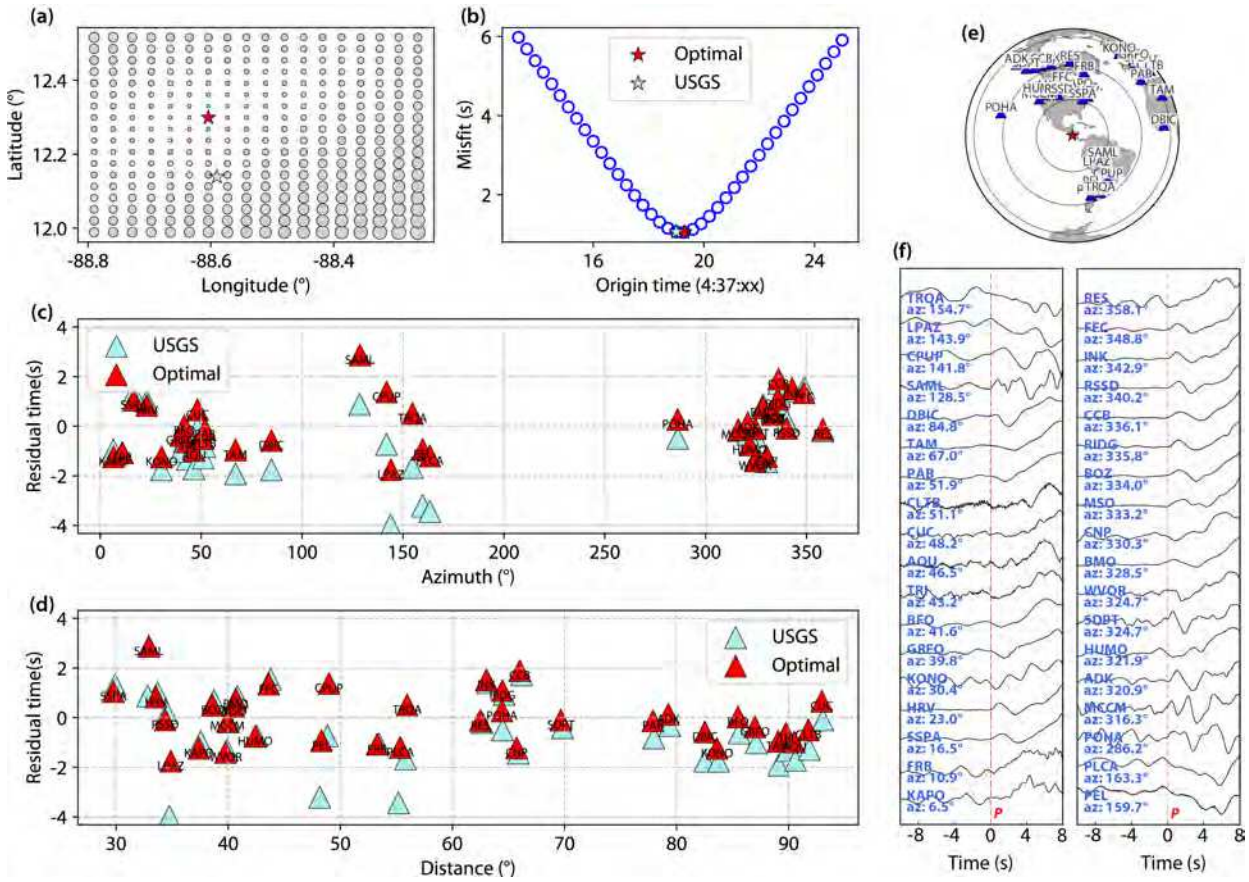

Figure S12. Relocation of the 2012 M_W 7.3 El Salvador earthquake. The depth of our optimal solution is fixed at 19.9 km by projecting the corresponding epicenter onto the Slab 2.0 model. Other symbols are same as Figure S3.

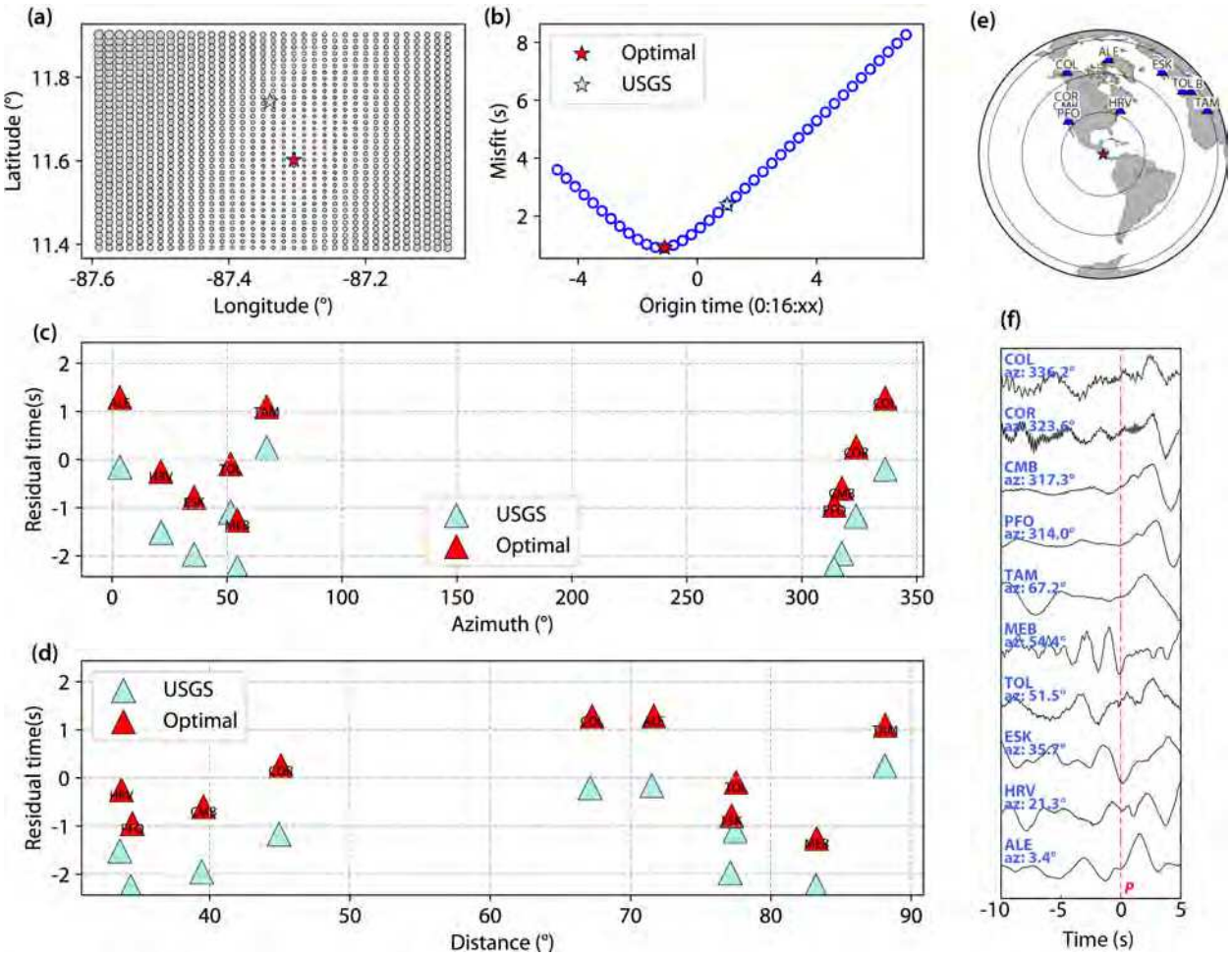

Figure S13. Relocation of the 1992 M_W 7.6 Nicaragua earthquake. The depth of our optimal solution is fixed at 19.9 km by projecting the corresponding epicenter onto the Slab 2.0 model. Other symbols are same as Figure S3.

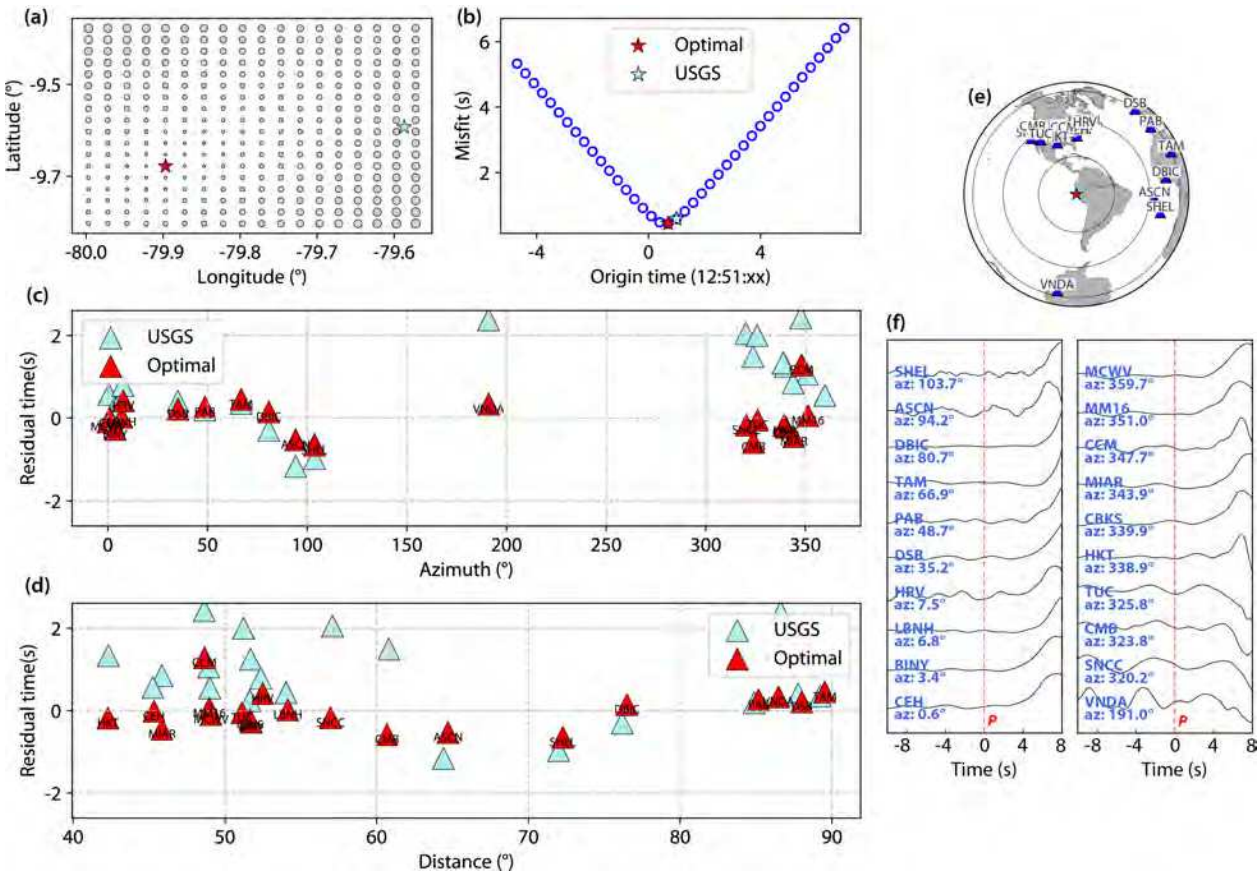

Figure S14. Relocation of the 1996 M_W 7.6 Peru earthquake. The depth of our optimal solution is fixed at 16.9 km by projecting the corresponding epicenter onto the Slab 2.0 model. Other symbols are same as Figure S3.

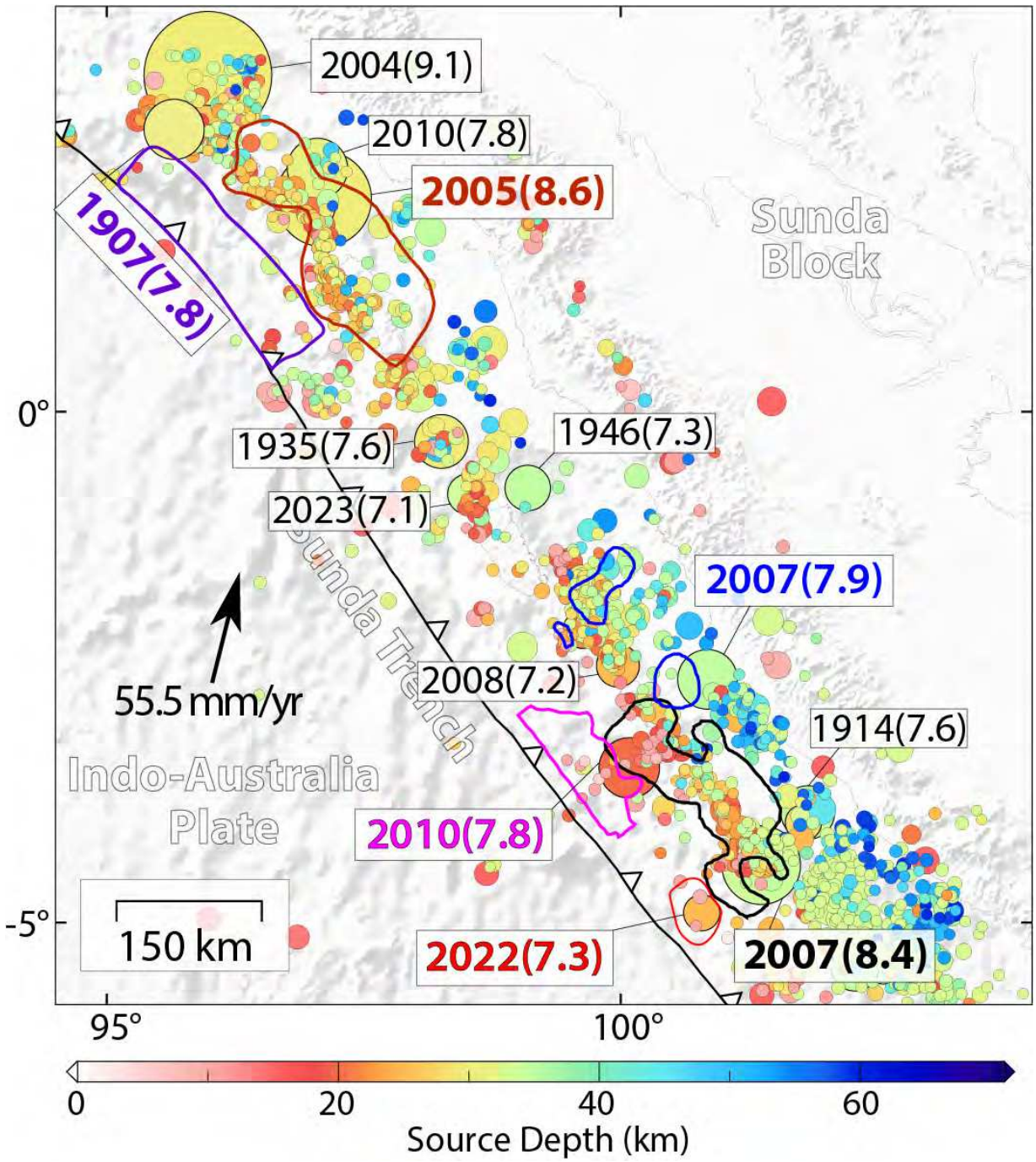

Figure S15. Seismicity in the southern Sumatra subduction zone. Circles show earthquake epicenters from the USGS- NEIC catalog since 1900, scaled with earthquake magnitude, and color-coded with source depth. Bold contours show the main slip distributions for the 1907 M_W 7.8 Sumatra (Kanamori et al., 2010; Martin et al., 2019; deep-purple curve), 2005 M_W 8.6 Nias (Hsu et al., 2006; brown curve), 2007 M_W 8.4 Bengkulu (Konca et al., 2008; black curve), M_W 7.9 Pagai (Konca et al., 2008; blue curves), 2010 M_W 7.8 Mentawai (Yue et al., 2014; magenta curve), 2022 M_W 7.3 Sumatra (this study; red curve) earthquakes. Black arrow represents plate motion direction and rate of the Indo-Australia plate relative to the fixed Sunda block computed using model MORVEL (DeMets et al., 2010).

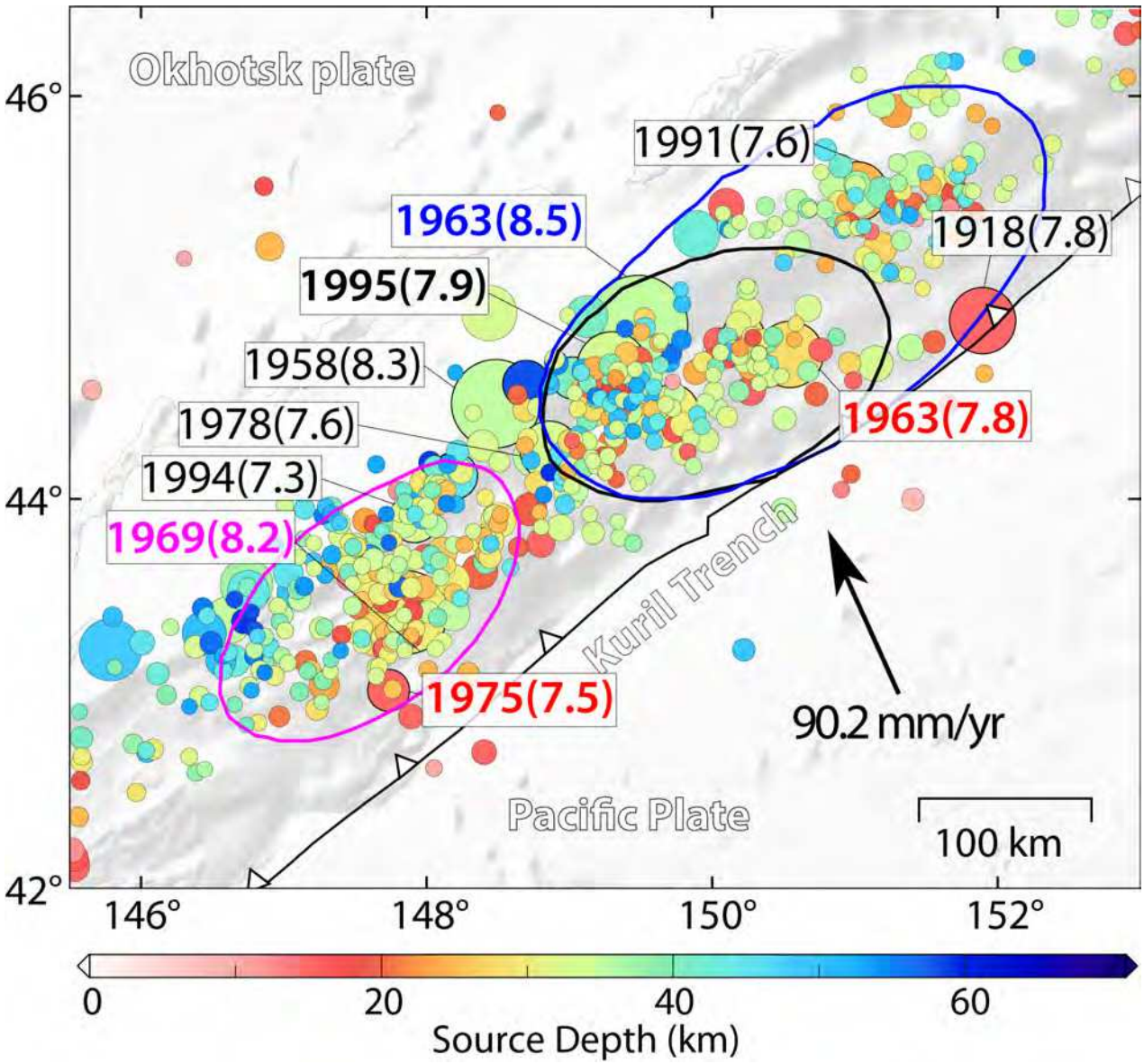

Figure S16. Seismicity in the Kuril subduction zone. Circles show earthquake epicenters from the USGS- NEIC catalog since 1900, scaled with earthquake magnitude, and color-coded with source depth. Bold contours show the main slip distributions for the 1963 M_W 8.5 (blue curve), 1969 M_W 8.2 (magenta curve), and the 1995 M_W 7.9 (black curve) Kuril events (Fukao. 1979; Pelayo & Wiens, 1992; Pérez, 2000). Black arrow represents plate motion direction and rate of the Pacific plate relative to the fixed Okhotsk plate computed using model MORVEL (DeMets et al., 2010).

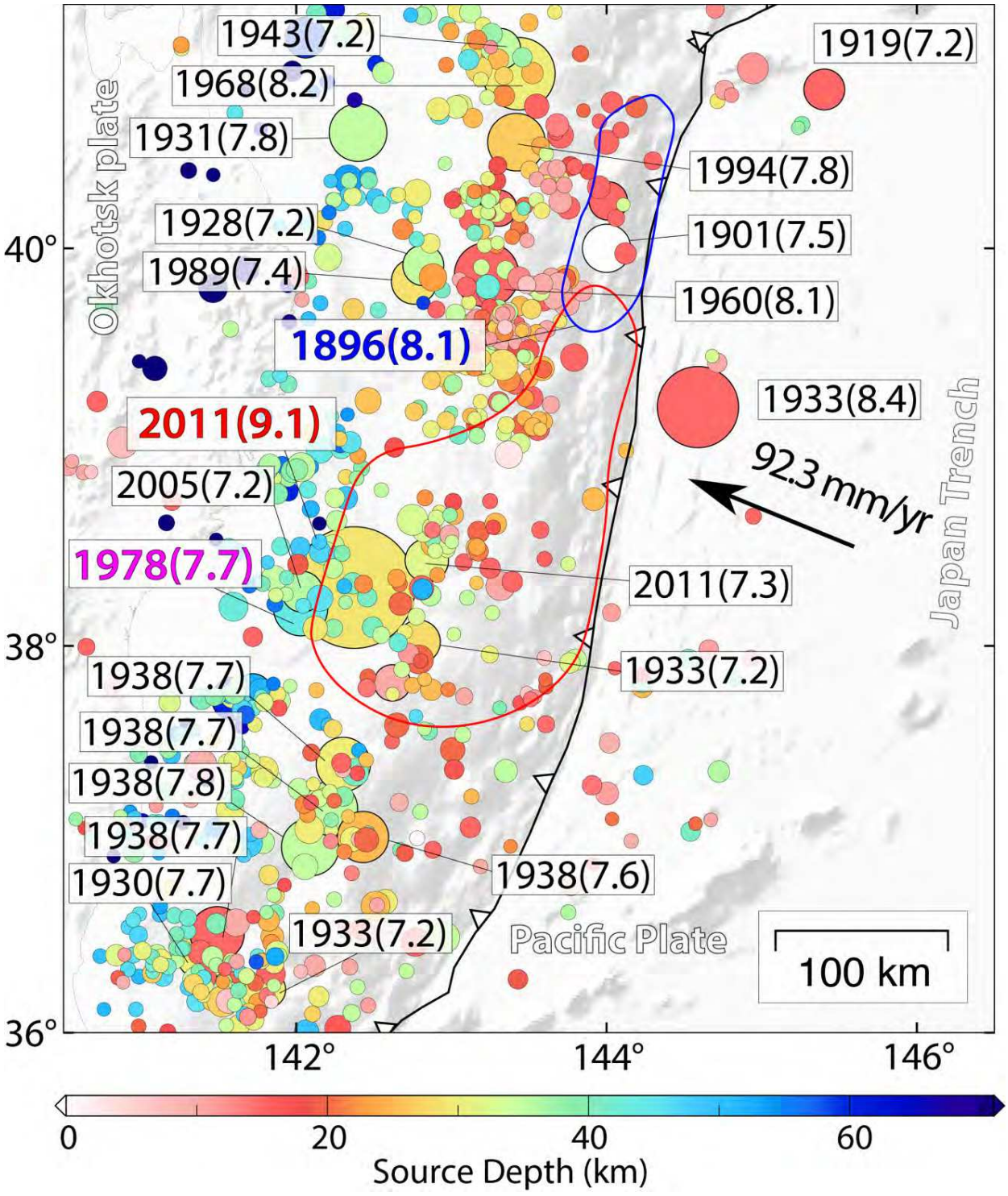

Figure S17. Seismicity in the Japan subduction zone along Honshu. Circles show earthquake epicenters from the USGS- NEIC catalog since 1900, scaled with earthquake magnitude, and color-coded with source depth. Bold contours show the main slip distributions for the 1896 M_W 8.1 Sanriku (blue curve), and the 2011 M_W 9.1 Tohoku (red curve) events (Ye et al., 2021). Black arrow represents plate motion direction and rate of the Pacific plate relative to the fixed Okhotsk plate computed using model MORVEL (DeMets et al., 2010).

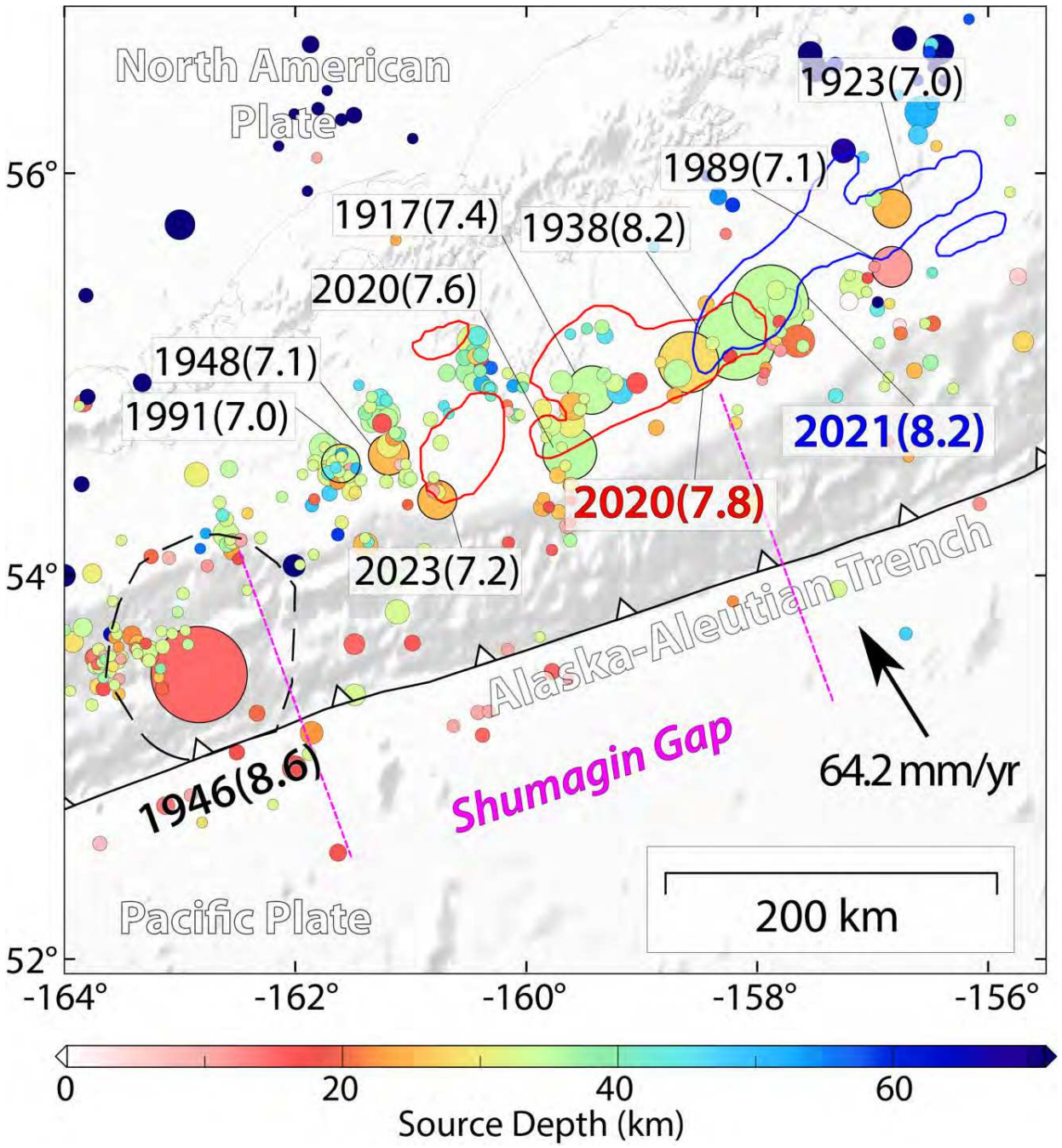

Figure S18. Seismicity along the Shumagin Gap Alaska-Aleutian subduction zone. Circles show earthquake epicenters from the USGS-NEIC catalog since 1900, scaled with earthquake magnitude, and color-coded with source depth. Bold contours show the main slip distributions for the 2020 M_W 7.8 Shuamgin (Liu et al., 2023; red curves), the 2021 M_W 8.2 Chignik (Ye et al., 2022; blue curves) events. Black arrow represents plate motion direction and rate of the Pacific plate relative to the fixed North American plate computed using model MORVEL (DeMets et al., 2010).

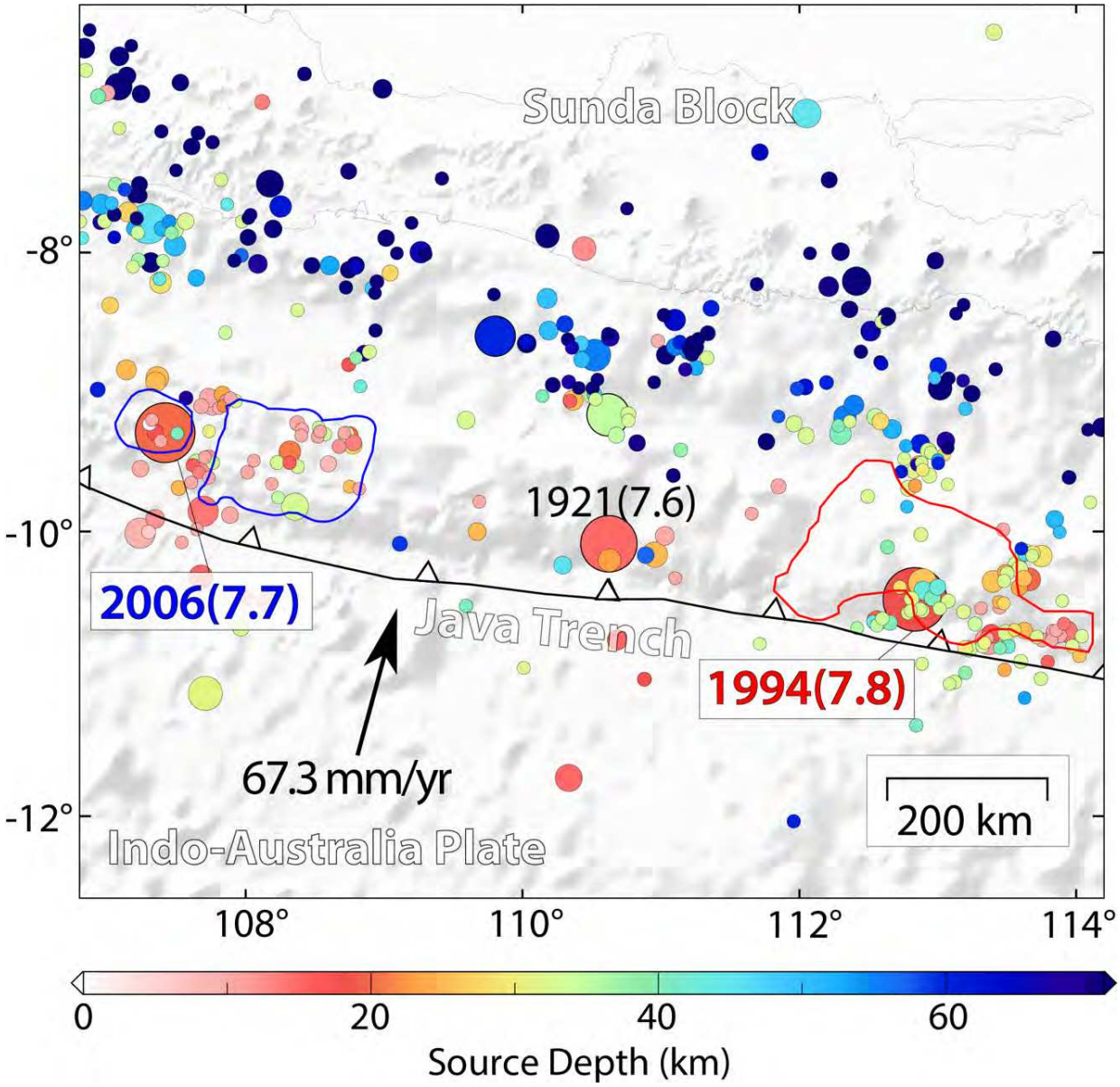

Figure S19. Seismicity in the Java subduction zone. Circles show earthquake epicenters from the USGS-NEIC catalog since 1900, scaled with earthquake magnitude, and color-coded with source depth. Bold contours show the main slip distributions for the 1994 M_W 7.8 Java (Bilek and Engdahl, 2007; red curve), the 2006 M_W 7.7 Java events (Ammon et al., 2006; blue curves) events. Black arrow represents plate motion direction and rate of the Indo-Australia plate relative to the fixed Sunda block computed using model MORVEL (DeMets et al., 2010).

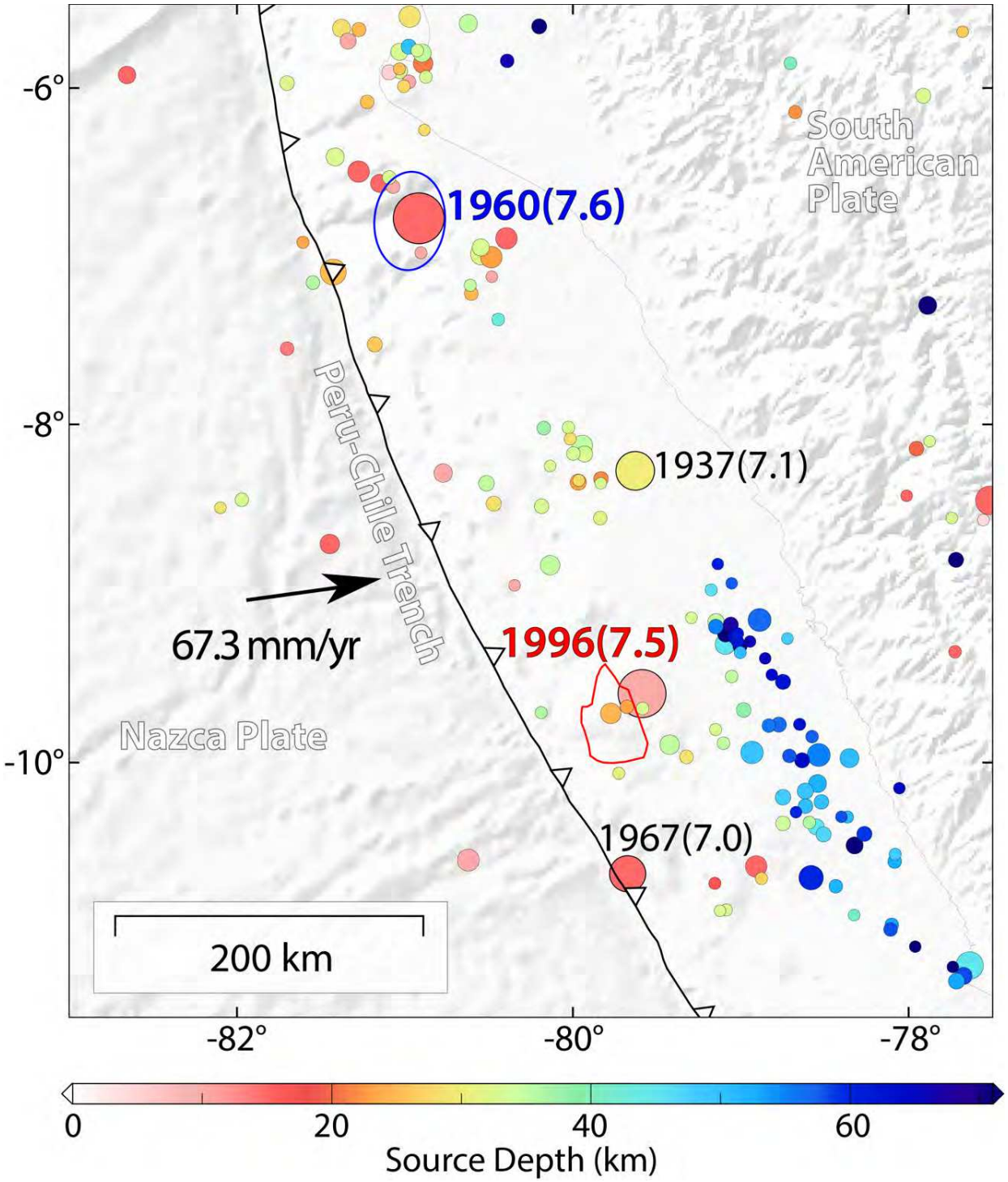

Figure S20. Seismicity in the Peru-Chile subduction zone. Circles show earthquake epicenters from the USGS-NEIC catalog since 1900, scaled with earthquake magnitude, and color-coded with source depth. Bold contours show the slip distributions for the 1960 M_W 7.6 Peru (Pelayo and Wiens, 1992; Bilek, 2010; blue curve), 1996 M_W 7.5 Peru (Ihmlé et al., 1998; red curve) events. Black arrow represents plate motion direction and rate of the Nazca plate relative to the fixed South American plate computed using model MORVEL (DeMets et al., 2010).

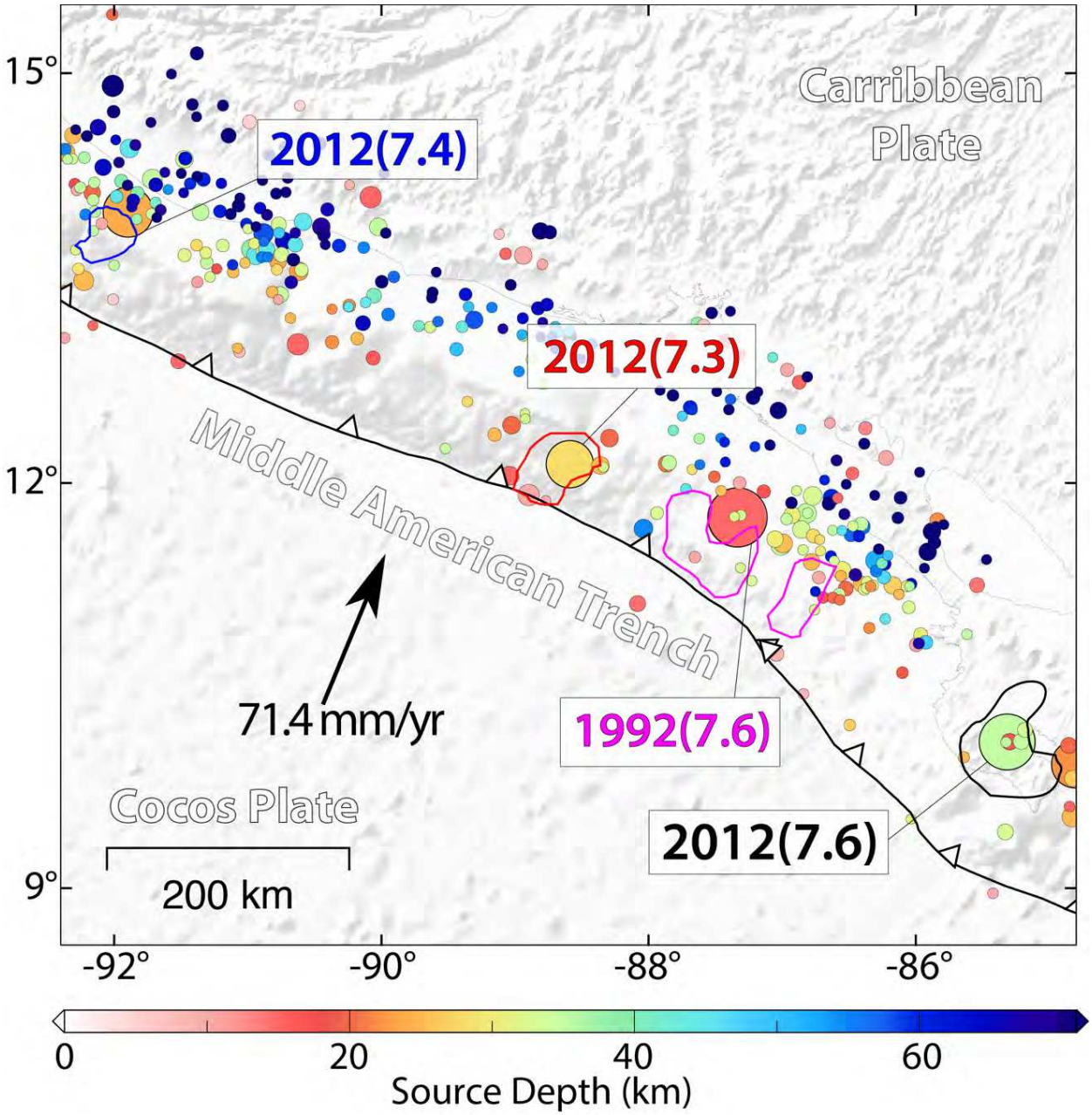

Figure S21. Seismicity in the Middle American subduction zone. Circles show earthquake epicenters from the USGS-NEIC catalog since 1900, scaled with earthquake magnitude, and color-coded with source depth. Bold contours show the main slip distributions for the 1992 M_W 7.6 Nicaragua (Ye et al., 2013; magenta curves), 2012 M_W 7.3 EI Salvador (Ye et al., 2013; red curve), 2012 M_W 7.4 Guatemala (Ye et al., 2013; black curve), and 2012 M_W 7.6 Costa Rica events (Ye et al., 2013; black curve). Black arrow represents plate motion direction and rate of the Cocos plate relative to the fixed Caribbean plate computed using model MORVEL (DeMets et al., 2010).